Understanding the effects of nozzle chevrons on jet noise

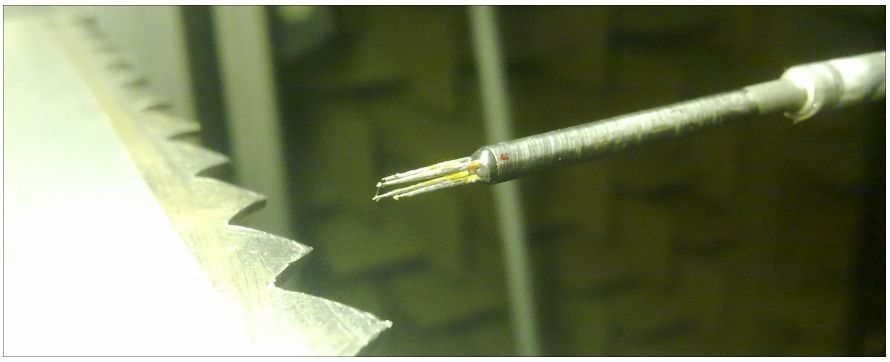

Gilbert Schantl

Institut für thermische Turbomaschinen und Maschinendynamik
Technische Universität Graz
Austria

May 2012

Diploma Thesis

Accepted version
16th of May 2012

Institut für thermische Turbomaschinen und Maschinendynamik
Technische Universität Graz
Inffeldgasse 25 A
8010 Graz Austria

Typeset by the author using LaTeX.
Printed in Austria.

Summary

Noise emissions are an inconvenient side effect of air travel. Nowadays, as air ports are often enclosed by residential areas and the number of handled flights is higher than ever, the reduction of noise due to air travel is of considerable importance. Besides organizational approaches, such as the prohibition of night flight or target-oriented land-use planning, there are technical approaches that focus on the noise source, i.e. the plane. A starting jet plane emits noise from diverse sources, of which the engines are still the biggest. Similarly to total air craft noise, the noise emissions of the engines can also be broken down and assigned to their respective sources. The most important of these sources is the hot and fast jet leaving the engine through the exhaust nozzle. It is the turbulent mixing of the jet with the ambient air that is generating the emitted noise. The velocity difference between the jet and the ambient air strongly influences the sound intensity, with a big velocity difference corresponding to a "loud" jet. Thus, the trend towards greater nozzle diameters and slower jets has favorably influenced the noise emissions. This development is limited by the resulting engine size and the fact that a certain velocity difference is necessary for the provision of thrust, however, which is why further means to reduce the noise emissions are necessary. So-called *nozzle chevrons* have shown to improve the noise emitting behavior with very little thrust loss. Chevrons are effectively serrated nozzle trailing edges and it is generally agreed on that they reduce the noise emissions by, at least partly, inhibiting the development of large flow structures in the mixing layers. Chevrons on round nozzles have been extensively studied and are already in commercial use. The effects of chevrons on jets coming from rectangular nozzles have, on the other hand, been hardly investigated. It was thus the aim of the work at hand to elementarily study these effects. To this end, two 275mm-by-13.5mm “chevroned” nozzles differing in terms of flow protrusion depth were compared to a non-serrated baseline nozzle of the same dimensions. The tests were carried out in an anechoic wind tunnel, which supplied a cold, low Mach number flow. By means of hot wire

anemometry the velocity fields resulting from the different jets were obtained and subsequently compared. Furthermore, the sound field was investigated via microphones close to the nozzle and some distance away. Sound-flow correlation tests were done as well.
The most important result of this investigation is that chevrons are working, indeed also on rectangular nozzles. Reductions of up to 4dB have been recorded. The magnitude of the noise reductions depends on a number of factors, however. Among those are the frequency, the direction of emission and the protrusion depth serrations.

Kurzfassung

Geräuschemissionen sind ein unangenehmer Nebeneffekt des Luftverkehrs. Heutzutage sind Flughäfen aufgrund des Städtewachstums oft in unmittelbarer Nähe von Wohngebieten, darüber hinaus hat sich auch die Anzahl der abgewickelten Flüge über die letzten Jahrzehnte drastisch erhöht. Neben organisatorischen Ansätzen, wie zum Beispiel Nachtflugverboten oder auf die Problematik abgestimmte Flächennutzungsplanung, gibt es natürlich technische Ansätze, die auf die Geräuschquelle, also das Flugzeug, zielen. Die einzelnen Schallquellen eines startenden Düsenflugzeuges sind mannigfaltig, allerdings tragen die Triebwerke am meisten zur Gesamtschallleistung bei. Wie das Gesamtgeräusch kann auch das Triebwerksgeräusch in aufgeteilt und Teilquellen zugeordnet werden. Die wichtigste Teilquelle des Triebwerksschalls ist der schnelle und heiße Freistrahl, der aus der Düse tritt. Das turbulente Vermischen des Freistrahls mit der Umgebungsluft erzeugt den Schall. Als Faktor mit dem stärksten Einfluss auf die Schallintensität gilt die Geschwindigkeitsdifferenz zwischen dem freistrahl und der Umgebung, wobei eine hohe Geschwindigkeitsdifferenz zu hohen Schallemissionen führt. Der Trend zu größeren Triebwerksdurchmessern und kleineren Freistrahlgeschwindigkeiten hat sich daher positiv auf das Geräuschverhalten von Flugzeugen ausgewirkt. Allerdings ist diese Entwicklung, erstens, durch die daraus resultierenden Triebwerksgrößen und, zweitens, durch die Tatsache, dass eine gewisse Geschwindigkeitsdifferenz vorhanden sin muss, um überhaupt Schub erzeugen zu können, begrenzt. Daher sind weitere Maßnahmen zur Reduzierung notwendig. Sogenannte *Chevrons* haben sich als sehr wirksam erwiesen, ohne nennenswerte Schubverluste zu bedingen. Chevrons sind im Grunde Zacken in der Düsenhinterkante eines Triebwerkes und nach vorherrschender Meinung verringern sie die Lärmemissionen, weil sie die Entstehung großer, zusammenhängender Strömungsstrukturen in der Mischschicht zumindest zum Teil verhindern. Über runde Düsen mit Chevrons liegen bereits umfangreiche Untersuchungen vor und solche Düsen werden inzwischen auch schon kommerziell eingesetzt.

Allerdings wurden entsprechende rechteckige Düsen de facto nicht erforscht. Das Ziel der vorliegenden Arbeit war daher die elementare Untersuchung der Einflüsse von Chevrons auf die Freistrahlen aus rechteckigen Düsen. Zu diesem Zwecke wurden drei Düsen mit einem Querschnitt von 275mm mal 13.5mm angefertigt, wobei eine dieser Düsen keine Zacken aufwies und als Referenz diente. Die beiden anderen – gezackten – Düsen unterschieden sich nur in der Eindringtiefe der Zacken in die Strömung. Ein schalltoter Windkanal, der eine kalte Strömung mit niedriger Machzahl bereitstellte, diente als Messumgebung. Die den verschiedenen Düsenformen zugehörigen Geschwindigkeitsfelder wurden mittels Hitzdrahtanemometrie aufgenommen und im Anschluss verglichen. Zur Quantifizierung der des Schallfeldes wurden Mikrophone - positioniert in unmittelbarer Nähe des Austrittes sowie in einer gewissen Entfernung davon – eingesetzt. Untersuchungen der Korrelation der Schall- und Strömungsfelder wurden ebenfalls durchgeführt.
Als wichtigste Erkenntnis der vorliegenden Arbeit kann gelten, dass Chevrons tatsächlich funktionieren, und zwar auch an rechtwinkeligen Düsen. Lärmreduktionen von bis zu 4dB konnten gemessen werden. Wie stark sich Chevrons auswirken hängt von gewissen Faktoren ab, darunter die Frequenz, die Abstrahlrichtung sowie die eindringtiefe der Zacken.

Declarations

Originality

This work contains no material which has been accepted for the award of any other degree of diploma in any university or other tertiary institution. To the best of my knowledge and belief, this work contains no material previously published or written by another person, except where due reference has been made in the text.

Permissions

I give consent to this copy of my thesis, when deposited in the University Library, being made available for loan and photocopying, subject to the provisions of the Copyright Act 1968.
I also give permission for the digital version of my thesis to be made available on the web, via the University's digital research repository, the Library catalogue, the Australasian Digital Theses Program (ADTP) and also through web search engines, unless permission has been granted by the University to restrict access for a period of time.

Gilbert Schantl

Acknowledgements

All tests were carried out at the University of Adelaide, Holden laboratory (School of Mechanical Engineering), and all the equipment was provided by this institution as well. Apart from the nozzles, i.e. the specimens, said equipment consisted of an anechoic wind tunnel, microphones, hot wire anemometers and all the necessary supply, calibration, mounting and data acquisition infrastructure.
I want to thank Dr Con Doolan for giving me the opportunity to carry out the research for my diploma thesis as temporary member of his group at the University of Adelaide. Furthermore, I want to thank him and Dr Danielle Moreau for their continous professional support, which helped me to overcome obstacles and to fill gaps in my knowledge.
Dr. Andreas Marn from the Institut für thermische Turbomaschinen at TU Graz deserves the same gratitude, as he not only agreed to supervise and support my work over a considerable distance and several time zones, but also assisted me during the actual writing process.
Naturally, I want to deeply thank my parents, who have always supported - morally as well as financially - my university career.

Contents

List of Figures

List of Tables

1 Introduction

1.1 Motivation

The jet engine is closely tied to the rise of commercial air travel in the last six decades. Even though propeller-driven planes paved the way after the second World War and already managed to gain notable passenger numbers, only the launch of drastically faster and more powerful jet airliners provided the hike in profitability that enabled the airlines to lower the fares. All put into service in the second half of the 1950s, the Sud Aviation Caravelle, the Tupolev Tu-104 and, particularly, the Boeing 707 (Figure 1.1) are widely considered to have truly started the jet age - even though the first airplane of this kind was unveiled as early as 1949. Ever more powerful engines allowed

(a) Caravelle Sud[1] (b) Tupolev Tu-104[2] (c) Boeing 707[3]

Figure 1.1: Pioneering aircraft

the construction of aircraft with more seats, higher payload and longer range. The notorious 747 is the prime example of this development, ultimately bringing down ticket prices to a very accessible level. Nowadays, air travel is the dominant means of long distance passenger transportation and plays an important role in freight handling. Since so called low cost carriers (LCC) severed the last ties to the times when jet flight was a privilege of the rich, i.e. sacrificed service and comfort in favor of discount prices, flying now is not only safe and fast, but has also become very cheap. Hence, air traffic has increased dramatically (Figure 1.2) over the years.

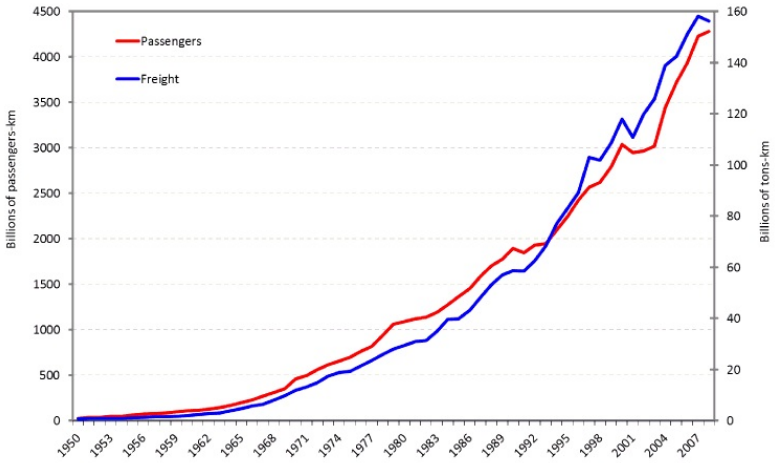

Figure 1.2: Increase in air traffic passenger number and freight volume over the last sixty years[5].

This increase in traffic naturally led to an augmentation of aviation-caused emissions, both chemical and acoustical. Jet engines are very powerful, but unfortunately also "dirty and loud". Take-off requires the most power, a fact made obvious by the noticeable-from-a-distance kerosene stench a starting plane leaves behind (Figure 1.3) and it is no coincidence that whenever the particular loudness of a certain noise is stressed, the proverbial "starting aircraft" is referred to.

Figure 1.3: Starting McDonnell F-4F Phantom II with exhaust gases clearly visible[4].

Despite the undeniable impact of combustion byproducts on climate change, noise emissions have a more immediate effect on the public, especially since many airports are now enclosed by residential areas as a result of the continuing growth of cities. Moreover, surveys have shown that, given equal loudness, consistently twice as many persons find air traffic noise "annoying" than do road traffic noise (*Environmental noise* 2012). The legal requirements for sound emissions are hence getting ever tighter, with the International Civil Aviation Organization *ICAO* acting at an international level (*ICAO* 2012). Besides setting certification standards for new aircraft, so called "Chapters", the ICAO requires its members to adopt a *Balanced Approach* to noise management (POST 2003), including land-use planning around airports with noise emissions in mind, optimization of operation procedures such as approach sequences and certain operational limitations (prohibition of night flight, limited airport access of especially noisy planes). These noise management measures are meant to bolster the technical improvements regarding the noise reduction "at the source", i.e. the aircraft.
Naturally, the design of the entire aircraft influences the noise emissions, but the engines are still the key factor. During take-off they are by far the greatest contributor to the overall noise level, with the exhaust jet being the greatest single contributor to total engine noise. It is the turbulent mixing of the fast and hot exhaust gases with the ambient air that causes significant sound emissions. Continuous research and development have led to drastic noise reductions, though. The exhaust speed, for example, which is the most important parameter in this respect, could be reduced by more then 50% while mass flow and, consequently, thrust remained constant or even increased (Möser and Müller 2003). In order to provide trust at all, the exhaust speed has to remain greater than the aircraft speed, however (see page 45).
Another measure to reduce noise emissions is to influence, i.e. enhance the mixing process of the exhaust gases with the surrounding air. Besides lobed nozzles, often employed to force the mixing of the inner and outer parts of co-axial jets, nozzle chevrons are used to this end. Chevrons are effectively serrated trailing edges of the exhaust ducts, which have proven to work in numerous investigations and were recently introduced to commercial flight on the engines of the Boeing 787 (Figure 1.4).

Figure 1.4: Rolls-Royce Trent 1000 on a Boeing 787 [6].

They facilitate noise reductions of several decibels with little or no thrust loss and, conveniently, chevrons can be retrofitted to existing engines with manageable effort. Despite extensive investigations done by researchers, it is still not completely certain in what way chevrons cause the measured noise reductions. There is a general consensus, however, about the chevrons causing the break-up of large coherent flow structures in the mixing zone, structures which are believed to be a main source of jet noise.
As research dealing with chevrons was centered on round nozzles up until now, the University of Adelaide initiated experimental research of chevron-equipped rectangular nozzles, with the work at hand being part of this ambition.

1.2 Task definition

The declared aim of this work was to experimentally investigate the basic influence chevrons have on the jet from a rectangular nozzle and on the resulting acoustic field. Furthermore, it was of interest to what extend these effects agreed with those caused by round-nozzle chevrons. Basically, the facilities used consisted of a small scale anechoic wind tunnel, where a cold low Mach number (~ 0.1) jet could be studied by means of hot wire anemometry and microphones.
As a first step, it was necessary to design and manufacture the nozzles to be compared and, additionally, an adapter to mount them in the already existing

wind tunnel. The fundamental dimensions of the nozzle outlet were adopted from an elaborate CFD-simulation, in which the University of Adelaide participates, but the detailed implementation of the chevrons was instead part of this work. Of the many possible configurations, three were build and successively investigated.
Secondly, the experiments had to be defined, i.e. the quantities or effects about which more information was desired. This required extensive literature research, to a considerable extend based on works about chevrons on round nozzles, but also about jets in general. As aspects to be investigated were chosen the global velocity field, the local turbulence distribution, the acoustic near and far fields and, finally, the correlation between flow and sound. It was not possible to gather information about all the mentioned areas at the same time, which is why a number of different measuring set-ups, all adapted to their respective purpose, had to be developed.
A not to be underestimated part of empirical research is the post-processing, interpreting and presentation of the data obtained. The final results will serve as a reference for future CAA-computations.

2 Theory

This chapter contains a brief excursion into theory. The aim is merely to provide concise explanations of the terms and effects mentioned in the later chapters. The first section is about jet engines, followed by a section dealing mainly with data processing and, somewhat more extensive, sections about flow mechanics and sound.

2.1 Jet engines

Nowadays, jet engines in all their configurations are the default means of propulsion for virtually all types of aircraft. Only in very small planes and in special applications are piston engines still in use. Gas-turbines offer a variety of advantages, such as fewer moving parts or a vastly better thrust-to-weight ratio. Their most important assets, however, i.e. the initial reasons why they were put into military service, are the abilities to work at very high altitudes and to reach speeds well above a vessel powered by propeller-engines, which are limited by decreasing propeller efficiency when blade tip speed approaches Mach 1.

2.1.1 History

Even though the basic principles of jet propulsion were known for several centuries, more serious development started at the beginning of the twentieth century. First patents were filed, and progress was made despite serious criticism until in the 1930s English and German engineers simultaneously, but independently, developed working stationary jet engines. Both of these early designs featured centrifugal, i.e. radial, compressors and axial turbines. The Germans subsequently came up with the axial compressor, which greatly reduced weight as well as frontal area and gave the jet engine its still valid layout. By the end of World War II, this new type of propulsion had been put into military service. The arms race of the Cold War further fueled development.

2.1.2 Layout

Turbojet

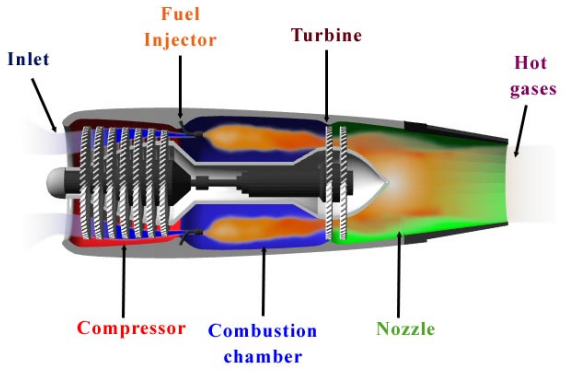

Figure 2.1: Turbojet[7]

Jet engines are implemented in several different ways, each layout optimized for a specific flow regime or application. As the original configuration, the so called "turbojet" shall be used for fundamental descriptions (Figure 2.1). Such devices consists of an air inlet, a compressor, a combustion chamber, a turbine and an exhaust nozzle. Thrust is solely provided by the momentum of the exhausted gas or, in other words, the reactive force acting on the engine. Turbine and compressor are connected via a shaft, with the former driving the latter. Atmospheric air is sucked in by the compressor and pushed into the combustion chamber. There, fuel is added to the pressurized air and the mixture ignited. The high enthalpy exhaust gas is driving the turbine and exits the engine through the nozzle, which is further accelerating the gas by reducing the cross-section. Compression and expansion can be staged, meaning that there is a low pressure compressor charging a high pressure compressor, both driven by their turbine counterparts via concentric shafts (Figure 2.21(a)). As said before, turbojets were the first configuration to be put into - military - service, but they are comparatively inefficient at lower speeds. They have thus largely been replaced by turbofans, even in military applications.

Turboprop and turboshaft

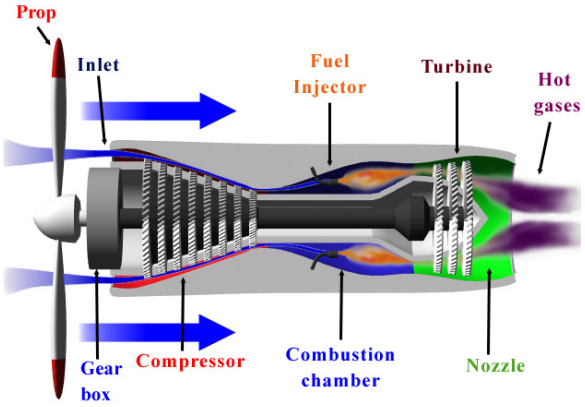

Figure 2.2: Turboprop[7]

As the name suggests, turboprops are a combination of a propeller a jet engine (Figure 2.2). Here, the turbine after the combustor does not only drive the compressor but also a shaft that is, usually via a transmission, driving a conventional propeller. Advantages like low weight and relative simplicity are thus combined with the low-speed efficiency of propellers. In order to power the propeller, virtually all the enthalpy is converted to mechanical work in the turbine stage, meaning that there is very little thrust contribution from the exhaust jet. Even though the best turboprop powered aircraft can reach speeds not far from Mach 1, this configuration is best suited to speeds below Mach 0.7. Turboshaft engines are very similar to turboprops, as they also use almost all the power to drive a shaft. One could probably call the turboprob a special version of the turboshaft, which features a highly integrated reduction gear to drive a propeller. Turboshafts are commonly used in helicopters or as auxiliary engines in big airplanes.

Turbofan

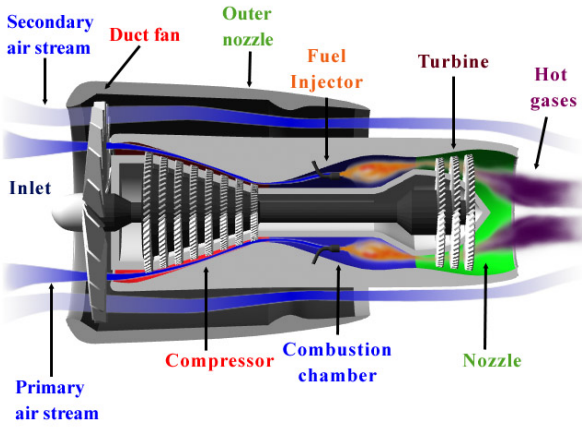

Figure 2.3: Turbofan[7]

Developed from early two-staged turbojets, turbofans (Figure 2.3) offer an exceptional blend of performance and efficiency, which made them the engine of choice for virtually all commercial and many military applications today. Their key feature is a ducted fan that is driven by the turbine and usually mounted in front of the core engine. The inlet air stream is divided, with one part being sucked into the turbine, where it is mixed with fuel and burned to provide power, and the other part being purely accelerated by the fan and pushed out the back (Figure 2.3). The ratio between the mass flows going through the combustion chamber and around is a definitive property of this type of engine, since it governs how big the contributions to total thrust from fan and jet, respectively, are. Turbofans are comparable to propeller engines in terms of fuel efficiency, but offer performance that is on par with turbojets. They are the most efficient engine configuration in a velocity range from about Mach 0.5 to 1.5, speeds at which more or less all commercial air travel takes place. On top of that, the relatively slow and cold air bypassing and enclosing the turbine significantly reduces the noise emissions.

Ramjet

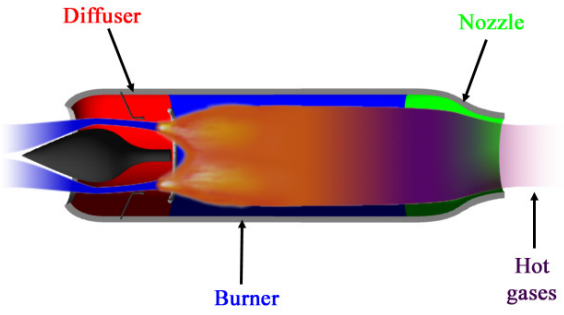

Figure 2.4: Ramjet[7]

Ramjets are a configuration adapted to very high supersonic speeds. Due to this high velocity, the dynamic pressure in the diffuser is sufficient to compress the air for the combustion process. Like in a turbojet, thrust is only provided by the momentum of the exhaust gas. Since no compressor is needed, the turbine is dispensable as well, which leaves no rotating parts in the engine (Figure 2.4).

2.2 Miscellaneous data processing terms

2.2.1 Fourier transformation

Fourier's theorem states that every general function can be represented as the sum of simple trigonometric functions. Figure 2.5 shows the decomposition of an arbitrary function into a number of sinusoidal functions that have different frequencies, phase shifts and amplitudes.

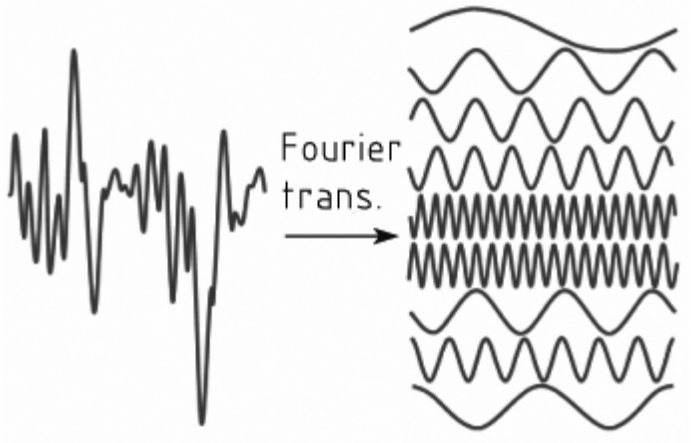

Figure 2.5: An arbitrary function (left) and the trigonometric functions (right) of which the sum is identical to the original function[8].

For the work at hand, this theorem is most relevant when applied on time-dependent signals. Via the *Fourier transformation* (Equation 2.1) signals can be converted from the time domain to the frequency domain, where every part function is represented by a frequency-amplitude couple (Figure **??**).

$$F(\omega) = \int_{-\infty}^{+\infty} f(t) e^{-j\omega t} \, \mathrm{d}t \tag{2.1}$$

$F(\omega)$ is the complex amplitude density and corresponds to the magnitude of a certain harmonic relative to its frequency.

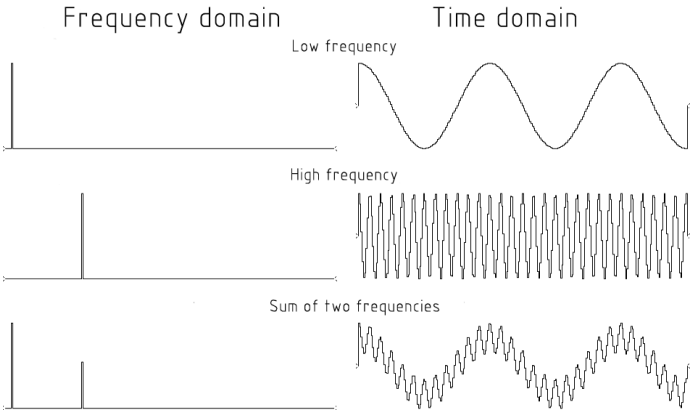

Figure 2.6: Frequency (left) and time (right) domains[9].

The frequency domain is expressed in the form of spectra, graphical means to show what each frequency (or frequency band) contributes to the total, be it pressure, power et cetera. In a spectrum, the frequency, sometimes non-dimensionalized, is plotted on the abscissa, while the corresponding amplitudes are plotted on the ordinate.
Inverse Fourier transformation allows the reconstruction of the original signal from the frequency spectrum by, basically, summing up the contributions of all the part frequencies (Equation 2.2.

$$f(t) = \frac{1}{2\pi} \int_{-\infty}^{+\infty} F(\omega) e^{j\omega t} \, \mathrm{d}\omega \tag{2.2}$$

Full reconstruction requires information about the phase shift, however. This can be accounted for by using the complex amplitude, which includes phase information, in the frequency spectrum.

2.2.2 Aliasing and Nykvist criterion

If the frequency with which a signal is sampled is to low, there is a risk of so-called "aliasing". This effectively means that a certain amplitude would be assigned to a wrong, i.e. lower, frequency in the frequency domain. To avoid this, the *Nykvist criterion* (Equation 2.3) requires the sampling frequency to be at least twice as high as the highest expected signal frequency.

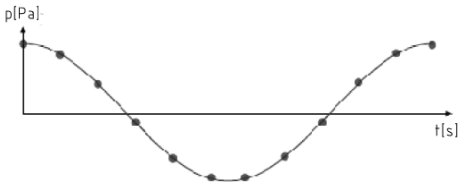

(a) $f_{sampling} \gg f_{signal}$

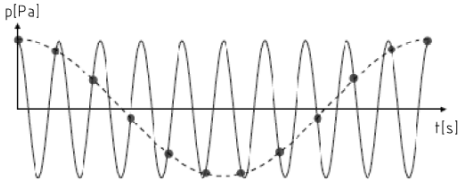

(b) $f_{sampling} \ll f_{signal}$

Figure 2.7: Aliasing.

$$f_{sampling} > 2f_{maxsignal} \tag{2.3}$$

2.2.3 Strouhal number

In order to facilitate the comparison of frequency spectra stemming from various signals, the frequency is often expressed in terms of the *Strouhal number*. It is a frequency quantity, which is non-dimensionalized using a characteristic length and a reference velocity.

$$Strouhal = f\frac{L}{U} \tag{2.4}$$

.

L Characteristic length, e.g. nozzle diameter
U Reference velocity

2.2.4 Correlation

Cross-correlation is a way to find out how similar two functions ($f(t)$, $g(t)$) are. It is basically done by shifting one of the functions ($g(t)$) relative to the other ($f(t)$) in the time or sample domain. To obtain the cross-correlation function ($[f \star g](t)$), the inner product ($f(t) \cdot g(t)$) of the functions is calculated and subsequently integrated over the phase shift, or lag τ (Equation 2.5; *mathworld* 2012).

$$[f \star g](t) = \int_{-\infty}^{+\infty} \overline{f}(-\tau) \cdot g(t-\tau)\,\mathrm{d}\tau \tag{2.5}$$

The lag which leads the the maximum integration value corresponds to the phase shift between the two functions of interest. Autocorrelation is basically the cross-correlation between two identical functions, one of which being phase-shifted, and yields information about characteristic time and/or length scales. The cross-correlation of discrete functions, such as measuring data, is computed using equation 2.6. All cross-correlation investigations in chapter **??** are based on this formula (*Matlab*).

$$\hat{R}_{f,g}(m) = \sum_{n=0}^{N-m-1} x_{n+m} y_n^* \tag{2.6}$$

N	Signal length
m	Number of samples one signal is shifted relative the other
$\hat{R}_{f,g}(m)$	Correlation value for a certain phase shift m

$\hat{R}_{f,g}(m)$ is usually normalized with the autocorrelation value at zero lag.

2.2.5 Coherence

Coherence is a measure for the linear dependency of two signals, usually of the input and output signals of a system, as a function of frequency. Furthermore, it can be understood as an estimate for the power transfer between the signals. In aeroacoustics, for example, the velocity fluctuations in the zone of noise generation correspond to the input signal and the far field sound to the output signal (*Wikipedia*).
Mathematically, coherence, often referred to as *magnitude squared coherence*, is defined by equation 2.7.

$$\gamma^2_{XY}(f) = \frac{|\langle G_{XY}(f)\rangle|^2}{\langle G_{XX}(f)\rangle \dot{\langle} G_{YY}(f)\rangle} \tag{2.7}$$

$\gamma^2_{XY}(f)$	Coherence value as a function of frequency
$\langle G_{XY}(f)\rangle$	Mean cross-power spectral density
$\langle G_{XX}(f)\rangle$, $\langle G_{YY}(f)\rangle$	Mean auto-power spectral densities of the signals
$X(f)$, $Y(f)$	Fourier transforms of the signals

2.3 Flow mechanical aspects

2.3.1 Boundary layers

At the end of the nineteenth century, flow mechanics as a science was firmly divided into theoretical hydrodynamics and applied hydraulics. The main reason for this was the inability of theory to reliably describe certain behaviors, e.g. the pressure drop in pipes or the flow resistance of bodies. It was relatively clear already then that this inferiority was due to the complete negation of friction in the computations, but even though flow equations taking into account viscosity, which basically translates to friction, had already been derived in these early days, their complexity prevented their solving in all but the simplest cases. Moreover, as the viscosities of air and water are very small, it was hard to comprehend for many that friction could have the big influence it seemed to have (Schlichting and Gersten 1997).

In 1904, Ludwig Prandtl found that friction had a big influence indeed, but also that the zones in which it had to be considered were very small. Such zones are thin layers and occur at domain boundaries (wall/fluid, static/moving domains of a fluid, etc.) with high velocity gradients normal to the flow direction. They are commonly called *boundary layers* or *shear layers*, as shear stresses are significant only there. To illustrate the basic principle, figure 2.8 shows a boundary layer at a wall, where the velocity gradient is the result of the no-slip condition at the wall.

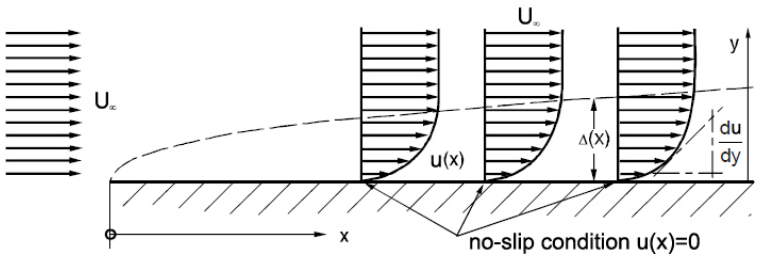

Figure 2.8: Boundary layer on a flat plane (Bräunling 2009).

As is obvious from the schematic, the boundary layer starts at the beginning of the wall, or, in other words, as soon as a velocity gradient is present, and grows in thickness thereafter. The boundary layer is delimited by $\Delta(x)$, the flow outside can be treated as inviscid, i.e. free of friction, and computed using the comparatively simple potential flow theory. There is no discontinuity in the velocity profile at the in boundary layer-inviscid flow interface and it is thus hard to discern where exactly the viscous zone ends. In practice, this is tackled by choosing a certain speed, often 99% of the free stream velocity, and defining it as the delimiting factor.
A free shear layers occurs between two fluid domains, which feature different flow velocities (Figure 2.9), hence leading to a velocity gradient. Similarly to the wall boundary layer, the shear layer starts upon the first occurrence of the velocity gradient and subsequently grows in thickness. Again, this thickness is described via a function $\delta(x)$.

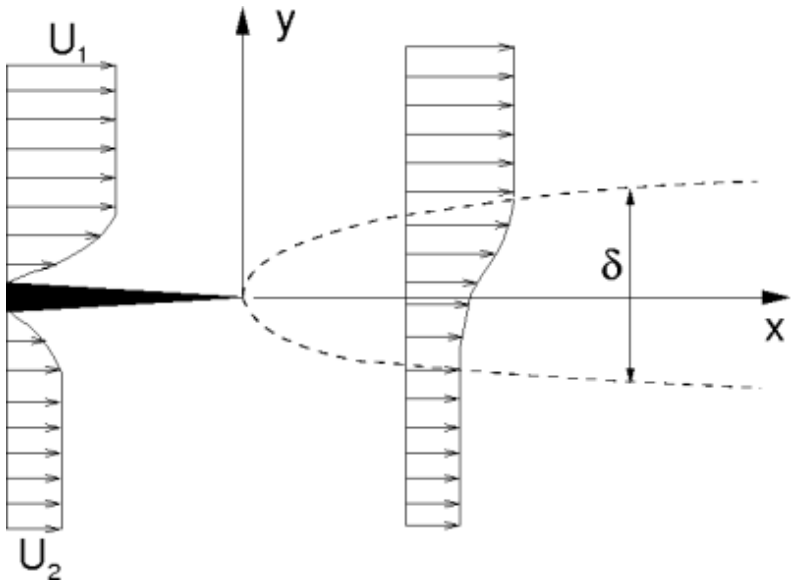

Figure 2.9: Shear layer (**REFREF**).

2.3.2 Viscosity

Fluid friction can be understood as the resistance of a fluid to deformation due to shear stresses τ. In a solid, shear stresses are a function of the strain, while they are related to the strain rate in fluids. The inherent fluid property governing friction is called viscosity μ, which is basically the proportionality factor relating the shear stress to the velocity gradient normal to the flow direction. Equation 2.8 shows the *Newtonian law* of fluid friction, which can be understood as the definition of viscosity.

$$\tau = \mu \frac{du}{dy} \tag{2.8}$$

If the viscosity of a certain fluid is independent of the strain rate, it is a Newtonian Fluid (air is such a fluid, for example). The so-called Couette flow (Figure 2.10(b)) usefully illustrates the Newtonian law. The upper of the two (infinite) plates is moved at a certain velocity with the resulting force couple F depending on the viscosity of the fluid between the plates. Viscosity can also be interpreted as a measure for momentum transport. In the Couette flow the shear forces due to the velocity difference between the upper and the lower fluid particles accelerate the lower particles, which effectively is momentum transported towards lower velocities. Momentum transport always happens in this direction.
Figure 2.10(a) shows the shear stresses on an infinitesimal fluid element.

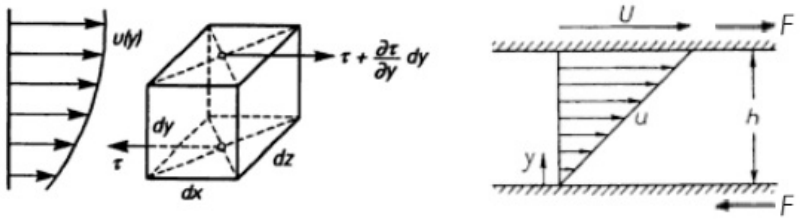

Figure 2.10: Couette flow(left) and friction forces on a volume element (right) (Schlichting and Gersten 1997)

2.3.3 Reynolds number

The dimensionless Reynolds number, which is defined in equation 2.9, is an important quantity to describe and compare flows.

$$Re = \frac{\rho U L}{\mu} = \frac{U L}{\nu} \tag{2.9}$$

- U Characteristic velocity
- L Characteristic length
- ρ density
- ν kinematic viscosity ρ / μ

It is effectively the ratio between the momentum forces and the viscous forces occurring in a flow. If two flows have the same Reynolds number and similar geometries, they will closely resemble each other qualitatively, even if they have vastly different characteristic length scales, i.e. extents. It is due to this *similarity* that results obtained in laboratories via model flows can be used to accurately predict the behavior of related full-scale flows.
A high Reynolds number means low relative friction, thus (theoretical) inviscid flows have infinite Reynolds numbers. Correspondingly, slow and inert flows have low Reynolds number. More or less depending on their (local) Reynolds numbers, flows (or flow regimes) are divided into two groups: laminar and turbulent.

2.3.4 Laminar or turbulent?

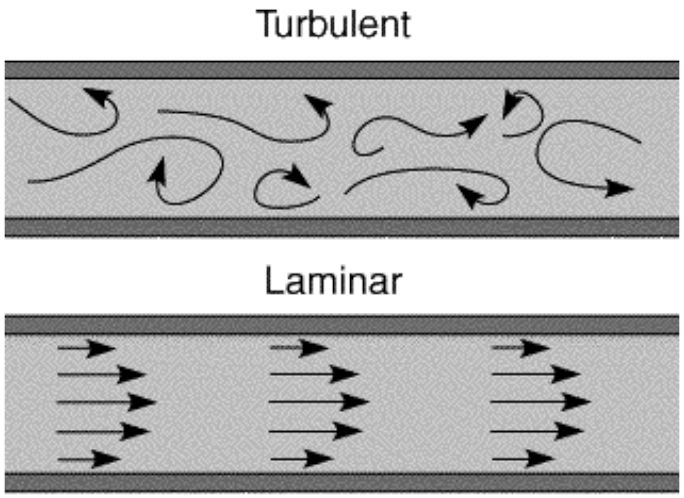

Figure 2.11: Laminar and turbulent (**REFREF**).

Up to a certain Reynolds number, flows are laminar. This means that the fluid is moving in layers, without rotation or movement normal to the flow direction (Figure **??**, bottom). As indicated above, even though there is no lateral mass transport, there is momentum transport from faster to slower layers. Increasing the Reynolds number, usually by upping the speed, increases the importance of the momentum forces, the flow becomes less stable and eventually, at a crossover Reynolds number which depends on the geometry, turbulent (Figure **??**, top). In turbulent flow, the fluid is no longer moving in layers, but rather stochastically, with rotation and movement normal to the flow direction. This leads to increases in momentum diffusion, friction and mixing. In fact, viscous momentum transport is far exceeded by momentum transport due to lateral fluid movement. Turbulence makes the determination or computation of the instantaneous velocities of single particles very hard, which is why properties of turbulent flow are usually given as the sum of a mean value and a statistical value that states the size of the fluctuations about the mean value. Equation 2.10 shows this using the example of the x-component of the velocity vector.

$$u(x,t) = \overline{u(x)} + u'(x,t) \tag{2.10}$$

$\overline{u(x)}$ corresponds to the ensemble average, or mean, of the velocity component, while $u'(x,t)$ describes the turbulent fluctuations. This decomposition

is useful in analysis as well as in experiments, where the turbulence level, or intensity I, is used to describe the magnitude of the turbulent fluctuations, i.e. how turbulent the flow is in a certain zone. It is defined as the turbulence kinetic energy k in relation to a reference velocity U_0 (Equation 2.11). If all three components of the root mean square of the velocity fluctuation (e.g. $\overline{u'}$ for the x-component) are known, k is calculated using equation 2.12. If only two components are available the third $\overline{w'}$ can be estimated. This is done by simply assuming that the magnitude of $\overline{w'}$ amounts to a mean value between the magnitudes of $\overline{u'}$ and $\overline{v'}$ (Equation 2.13). Given isotropy, I can also be gained via equation 2.15

$$I = \frac{\sqrt{2k/3}}{U_0} \tag{2.11}$$

$$k = \frac{1}{2}\left(\overline{u'}^2 + \overline{v'}^2 + \overline{w'}^2\right) \tag{2.12}$$

$$k = \frac{3}{4}\left(\overline{u'}^2 + \overline{v'}^2\right) \tag{2.13}$$

$$\overline{u'} = \frac{3}{4}\left(\overline{u'}^2 + \overline{v'}^2\right) \tag{2.14}$$

$$I = \frac{\sqrt{\overline{u'}^2}}{U_0} \tag{2.15}$$

An important feature of turbulent flow is its self-similarity, or self-preserving, which means that structures (velocity profiles, eddies, est.) occurring throughout the flow field can strongly resemble each other shape-wise, despite being vastly different in size. This can be exploited for computation proposes, using ansatz-solutions.
The kinetic energy transport in turbulent flow is a cascade process, where the largest turbulent structures are fed by the main flow, before decomposing into ever-smaller structures. Eventually, the kinetic energy of the then very small-scale turbulence dissipates.

2.3.5 Boundary layer equations

The *Navier-Stokes equations*, which take into account viscous effects, are considered the basic mathematic model of fluid mechanics and were already known in Prandtl's days, although hardly used due to their complexity. Equations 2.16 to 2.18 show the Navier-Stokes (NS) equations for a three-dimensional Cartesian coordinate system. Note that the temperature field and

the corresponding energy equations are not discussed here as the model flow investigated is isothermal. In-depth treatment can be found in designated literature (REF SCHLICHTING Gersten Herwig)

$$\rho\frac{Du}{Dt} = f_x - \frac{\partial p}{\partial x} + \frac{\partial}{\partial x}\left[\mu\left(2\frac{\partial u}{\partial x} - \frac{2}{3}div\boldsymbol{v}\right)\right] + \\ + \frac{\partial}{\partial y}\left[\mu\left(\frac{\partial u}{\partial y} + \frac{\partial v}{\partial x}\right)\right] + \frac{\partial}{\partial z}\left[\mu\left(\frac{\partial w}{\partial x} + \frac{\partial u}{\partial z}\right)\right] \tag{2.16}$$

$$\rho\frac{Dv}{Dt} = f_y - \frac{\partial p}{\partial y} + \frac{\partial}{\partial y}\left[\mu\left(2\frac{\partial v}{\partial y} - \frac{2}{3}div\boldsymbol{v}\right)\right] + \\ + \frac{\partial}{\partial z}\left[\mu\left(\frac{\partial v}{\partial z} + \frac{\partial w}{\partial y}\right)\right] + \frac{\partial}{\partial x}\left[\mu\left(\frac{\partial u}{\partial y} + \frac{\partial v}{\partial x}\right)\right] \tag{2.17}$$

$$\rho\frac{Dw}{Dt} = f_z - \frac{\partial p}{\partial z} + \frac{\partial}{\partial z}\left[\mu\left(2\frac{\partial w}{\partial z} - \frac{2}{3}div\boldsymbol{v}\right)\right] + \\ + \frac{\partial}{\partial x}\left[\mu\left(\frac{\partial w}{\partial x} + \frac{\partial u}{\partial z}\right)\right] + \frac{\partial}{\partial y}\left[\mu\left(\frac{\partial v}{\partial z} + \frac{\partial w}{\partial y}\right)\right] \tag{2.18}$$

Via dimensional analysis based on the assumption that $\delta(x) << L$, where L is the characteristic length scale of the flow, Prandtl managed to simplify the NS-equations sufficiently to make them applicable. When abdicating non-dimensionalization, the Prandtl-equations for a laminar, planar, incompressible and stationary flow are

$$\frac{\partial u}{\partial x} + \frac{\partial v}{\partial y} = 0 \tag{2.19}$$

$$\rho\left(u\frac{\partial u}{\partial x} + v\frac{\partial u}{\partial y}\right) = -\frac{\partial p}{\partial x} + \frac{\partial^2 u}{\partial y^2} \tag{2.20}$$

with the boundary conditions

$y = 0$: $\quad u = v = 0$

$y = \infty$: $\quad u(x) = U(x)$.

Inserting equation 2.10 and the analog equation for v into equations 2.19 and 2.20 yields the turbulent boundary layer equations

$$\frac{\partial \overline{u}}{\partial x} + \frac{\partial \overline{v}}{\partial y} = 0 \tag{2.21}$$

$$\rho\left(\overline{u}\frac{\partial\overline{u}}{\partial x}+\overline{v}\frac{\partial\overline{u}}{\partial y}\right)=-\frac{\partial p}{\partial x}+\frac{\partial}{\partial y}\left(\overline{\tau}_v+\tau_t\right) \tag{2.22}$$

with

$$\overline{\tau}_v=\mu\frac{\partial\overline{u}}{\partial y} \tag{2.23}$$

and

$$\tau_t=-\rho\overline{u'v'} \tag{2.24}$$

.
$\overline{\tau}_v$ are the shear stresses due to viscosity (see equation 2.8) and τ_t the turbulent shear stresses. τ_t is a new unknown, which would require a further equation. This problem is solved via turbulence models, basically empirical equations that establish connections between the mean flow field and the turbulent stresses. There are various turbulence models, such as the vortex viscosity and mixing length hypotheses.
Viscous stresses are only important in laminar flow and in the immediate vicinity of walls. Thus, in free turbulent shear layers $\overline{\tau}_v$ can be disregarded. The same is for the pressure term, as the static pressure is usually constant in free shear layers. Turbulent shear layers are governed by equations 2.25 to 2.26.

$$\frac{\partial\overline{u}}{\partial x}+\frac{\partial\overline{v}}{\partial y}=0 \tag{2.25}$$

$$\rho\left(\overline{u}\frac{\partial\overline{u}}{\partial x}+\overline{v}\frac{\partial\overline{u}}{\partial y}\right)=\frac{\partial\tau_t}{\partial y} \tag{2.26}$$

The aforementioned vortex viscosity model is defined by equation 2.27. It is obvious that equation 2.27 is very similar to the Newtonian law, which describes viscous stresses. The vortex viscosity value ν_t is obtained by means of different empirical equations of various complexity.

$$\tau_t=\rho\nu_t\frac{\partial\overline{u}}{\partial y} \tag{2.27}$$

2.3.6 Mach number

The Mach number is the ratio between the velocity U with which an object moves in a fluid and the local speed of sound c in this fluid (Equation 2.28).

$$Ma = \frac{U}{c} \tag{2.28}$$

If a fluid moves at a Mach number below 1, the flow is called *subsonic*, correspondingly it is traveling at *supersonic* speeds, if $Ma > 1$. Until $Ma \sim 0.3$, flows can usually be assumed to be incompressible, but at higher speeds effects due to changes in density gain importance, especially at transsonic ($Ma \sim$) and supersonic speeds. If supersonic flow is deflected or generally decelerated, the changes in velocity, pressure or density are not gradual, but rather sudden over a very short distance ($\sim 25\mu m$). Such rapid changes in flow conditions are called shocks.

2.3.7 Jets

The term "jet" describes moving fluid that is entering a zone of slower moving or stagnant fluid through a nozzle. In most practical applications, the fluid in the zone entered is the same as the jet fluid. Inevitably, there are velocity gradients at the interfaces between the moving and stationary domains, which cause the development of free shear layer. Jets can be laminar or turbulent, depending on the densities of jet and surroundings as well as on the initial Reynolds number of the faster fluid, but technically important jets are usually turbulent. Jets of air craft engines are highly turbulent, for example. As these are the subject of this work and since the investigated model flow is turbulent as well (see section XXX on page xxx), laminar jets will not be discussed any further.
Figure 2.12 shows the typical development of a turbulent jet. Zones where stagnant and flowing air mix form immediately after the outlet and grow linearly outwards and inwards (angles δ_a and δ_i). The core, where air is still undisturbed and traveling with the outlet velocity, hence has the shape of a cone (round nozzle) or a wedge (rectangular nozzle). This *potential core* is between 4.5 and 5 outlet diameters long, with the actual length depending on the temperatures, densities and Reynolds numbers of the fluids mixed (Eck 1981).

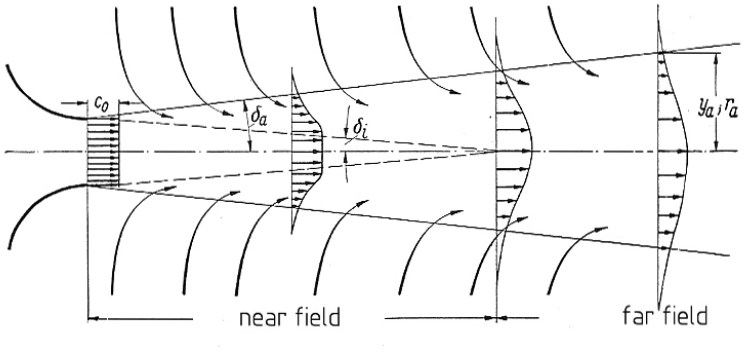

Figure 2.12: Typical development of a turbulent jet (Eck 1981).

After the extinction of the potential core (plus a short transition zone), the jet can be considered developed. This region is known as the *far field*, as opposed to the *near field* close to the outlet. In the far field, turbulent jets become very self-similar, meaning that velocity profiles at different stream-wise locations are akin and a linear dependency can be established between the normal coordinate y and the stream-wise coordinate x (Equation 2.29).

$$\eta \equiv \frac{y}{\Delta} \tag{2.29}$$

$\Delta(x)$ Characteristic length scale for the width of the shear layer .
Because of this, equation 2.26 becomes an ordinary differential equation. By using the following ansatz

$$u = U_\infty + U_N(x) f'(\eta) \tag{2.30}$$

U_∞ Ambient velocity
$U_N(x)$ Jet centerline velocity .
$f'(\eta)$ Shape function describing the velocity profile

$$v = -\frac{d(\Delta U_N)}{dx} f(\eta) + \frac{d\Delta}{dx} U_N \eta f'(\eta) \tag{2.31}$$

,
equations 2.30, 2.30 and 2.31 yield

$$(U_\infty + U_N f')\Delta \frac{dU_N}{dx} f' - U_\infty U_N \frac{d\Delta}{dx} \eta f'' - U_N \frac{d(\Delta U_N)}{dx} f f'' = \frac{U_N}{\Delta} (\nu_t f'')' \tag{2.32}$$

.

The integral of equation 2.26 over the jet cross section is the so-called *kinematic momentum*. It is independent of the stream-wise coordinate x and an important property of a jet.

$$K \equiv \int_{-\infty}^{+\infty} u^2 \, \mathrm{d}y = U_N^2(x)\Delta(x) \int_{-\infty}^{+\infty} f'^2 \, \mathrm{d}\eta = const \tag{2.33}$$

The fact that the kinematic momentum remains constant also influences the jet-specific ansatzes for $U_N(x)$ and $\Delta(x)$.

$$U_N(x) = B(x - x_0)^{-\frac{1}{2}} \tag{2.34}$$

$$\Delta = \alpha 4(x - x_0) \tag{2.35}$$

.
In equations 2.34 and 2.34 x_0 corresponds to the distance between the outlet and the virtual jet origin (see figure XXX) and α is a *slenderness parameter* connected to the vortex viscosity via equation 2.36. B is constant related to the kinematic momentum.

$$\nu_t(x) = \alpha \left| U_N(x) \right| \Delta(x) \tag{2.36}$$

Combination of the above finally yields the differential equation for the shape function f

$$f''' + 2(ff')' = 0 \tag{2.37}$$

with the boundary conditions $\begin{array}{ll} \eta = 0: & f' = 1 \\ \eta = \infty: & f' = 0 \end{array}$.
The non-trivial solution is

$$f(\eta) = tanh\eta \tag{2.38}$$

$$f'(\eta) = 1 - tanh^2\eta \tag{2.39}$$

.
Thus, $U_N(x)$ corresponds to the profiles' maximum values on the centerline. More detailed derivations of the velocity field can be found in (REF SCHLICHTING GERSTEN HERWIG)

As is the case with all shear layers, the outer limit edge of a jet is hard to determine; the velocity trends to zero asymptotically. This is why the measure

$y_{0.5}$ (or $r_{0.5}$ if the jet is round) is commonly used to define the outer edge. It corresponds to the y-positions (upper and lower) at which a certain property, e.g. stream wise velocity U or temperature, is half as great as it is on the centerline. The straights on which $y_{0.5_U}$ and $y_{0.5_T}$ lay were found to be inclined by 6.6° and 8.5°, respectively. As these angles are functions of the vortex viscosity μ, they are the same in all jets, given identical fluid and temperature. Note that other ratios, e.g. one tenth, of the flow properties are sometimes used to define the jet boundary as well. The reason for the broadening of the jet is the momentum transport from the fast jet to the slow or stagnant surrounding. The system strives towards an even momentum distribution. As the global kinematic momentum remains constant, a reduction in core velocity has to go along with the broadening. This momentum exchange on the edges also leads to previously stagnant air being sucked into the jet. This *entrainment* leads to an increase in volume flow along the center line and a non-zero vertical velocity component at the edges.

Figure 2.13 shows three free streams at different Reynolds numbers. The middle jet is initially laminar before transitioning and the growing structures in the mixing layer are nicely visible. The rightmost jet is fully turbulent and exhibits the linear opening mentioned above. The notable faster growing of turbulent jets clearly shows how much more turbulence contributes to momentum transport than does viscosity. The spiral-like structures visible in jets a and b are known as *Kelvin-Helmholtz instabilities*.

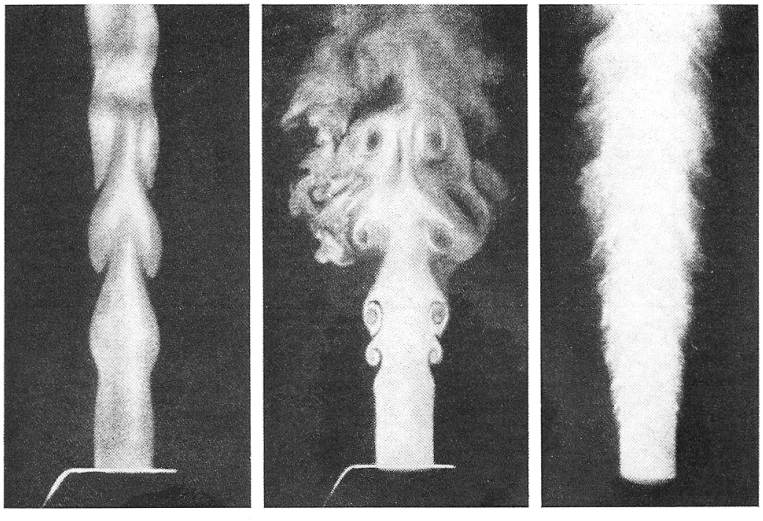

Figure 2.13: Jets with different Reynolds numbers: a) Re<1450, b) 3800<Re<4750, c) Re>10000 (Eck 1981)

The self-similarity grants that in the far field, after effects due to the nozzle shape have faded out, the (normalized) parameters describing the jet are only a function of the stream wise location x. Table **??** gives an overview of the relations.

Table 2.1: Jet parameters as functions of stream wise location (Schlichting and Gersten 1997).

Parameter	*f(x)*
Normalized centerline velocity	$U_N(x) \sim \frac{1}{\sqrt{x-x_0}}$
Lateral length scale	$\Delta(x) \sim x - x_0$
Mixing length	$l(x) \sim x - x_0$
Half U-magnitude width	$y_{0.5u} = 0.11(x - x_0)$
Half T-magnitude width	$y_{0.5t} = 0.14(x - x_0)$
Vortex viscosity	$\nu_t(x) \sim \sqrt{x - x_0}$
Normalized temperature	$T_N(x) \sim \frac{1}{\sqrt{x-x_0}}$
Lateral edge velocity	$y_e(x) \sim \frac{1}{\sqrt{x-x_0}}$

The lateral length scale is effectively the thickness of the mixing layers, while the lateral edge velocity could be understood as the entrainment velocity (Schlichting and Gersten 1997).

2.4 Sound

This section is based on (Marn and Pirker 2011) and (Möser and Müller 2003), where the interested reader is also referred to for more detailed information.

2.4.1 Field quantities

Strictly speaking, sound is mechanical oscillation that occurs within the audible range (from about 16Hz to, ideally, 20kHz). Noise is generally understood to be undesired sound, e.g. traffic noise, noise coming from conversations one is not part of or, the very topic of this work, aircraft noise. Depending on the medium the oscillation occurs in, sound is referred to as air-borne, solid-borne or water(liquid)-borne. Also depending on the medium is the preferred measurand to quantity the sound. In solids, this can be the deflection of a surface, its velocity or acceleration. In air, pressure fluctuations are almost exclusively resorted to, as they are the characteristic quantity for human hearing. These time-dependent fluctuations are superimposed on the

static air pressure p_0 and are usually smaller by several orders of magnitude (Figure 2.14).

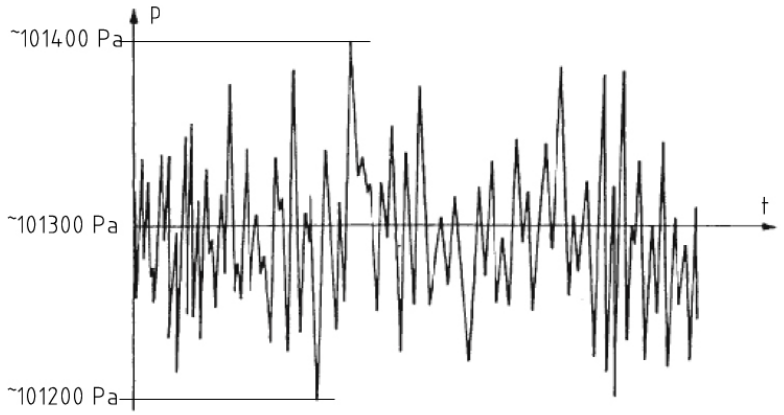

Figure 2.14: Sound corresponds to small pressure fluctuations about the 1 bar (101300 Pascal) static air pressure.

The pressure fluctuations can be expressed as

$$p' = \hat{p}cos(\omega t + \phi_p) \tag{2.40}$$

or, complex, as

$$\underline{p'} = \hat{p}e^{i(\omega t + \phi_p)} \tag{2.41}$$

,
if the sound is a harmonic oscillation. In equation 2.40 $\hat{p}$ is the amplitude, ϕ_p the phase shift and ω the angular frequency. Note that in the complex case, only the real part is relevant for cosines, while only the imaginary part is relevant for sines. Harmonic oscillations are also known as "pure tones".
Together with the sound pressure, the sound particle velocity v' (Equations 2.42 and 2.43 is used to describe the sound field. v' is the speed, with which the particles move about their initial position. It is a vector and not to be confused with the notorious *speed of sound* (see page 30).

$$\boldsymbol{v}' = \hat{\boldsymbol{v}}cos(\omega t + \phi_v) \tag{2.42}$$

$$\underline{\boldsymbol{v}'} = \hat{\boldsymbol{v}}e^{i(\omega t + \phi_v)} \tag{2.43}$$

In planar sound waves (see page 33), p' and v' are connected via equation 2.44.

$$p' = \rho c \boldsymbol{v}' \tag{2.44}$$

ρ Density of the medium
c Speed of sound in the medium

$p/\boldsymbol{v}$ is defined as the *acoustic impedance* of a material. It effectively governs, how much amplitude is necessary to transmit sound in a certain material.

There is energy contained in the compression of the fluid and in the movement of the particles. The so-called sound energy density w is defined by equation 2.45.

$$w = \frac{1}{2}\frac{p^2}{\rho_0 c^2} + \frac{1}{2}\rho_0 |\boldsymbol{v}|^2 \tag{2.45}$$

Sound intensity is defined as the product of sound pressure and sound particle velocity (Equation 2.46) and states the sound energy transmitted per unit area. Due to the sound particle velocity being a vector, the intensity is a vector as well.

$$\boldsymbol{I} = p\boldsymbol{v} \tag{2.46}$$

The sound power that passes a certain unit area normal to the velocity vector is obtained via integration of $\boldsymbol{I}$ (Equation 2.47).

$$P = \int I_n \, \mathrm{d}S \tag{2.47}$$

I_n Intensity component normal to the control surface
S Control surface

2.4.2 Speed of sound

The speed of sound c is the propagation velocity of sound waves in the supporting medium. It strongly depends on the material properties of the medium. Solids allow the highest propagation speeds ($c_{Steel} \sim 5000 m/s$), with liquids ($c_{H_2O} \sim 1450 m/s$) and gases ($c_{Air} \sim 343 m/s$) following suit. Since solids and liquids are irrelevant for this work, only the governing equation for gases is stated (Equation 2.48).

$$c = \sqrt{\kappa \frac{p_0}{\rho_0}} = \sqrt{\frac{\kappa R T_0}{M_{air}}} \tag{2.48}$$

p_0	Static pressure
ρ_0	Static density
κ	Heat capacity ratio, in air $\kappa = 1.4$
R	General gas constant $R = 8314 J/kmolK$
M_{air}	Molar mass of air

c can depend on the frequency and wavelength of a signal. This dependency is called dispersion and is governed by equation 2.49.

$$c = \lambda f = \omega \frac{1}{k} \tag{2.49}$$

$$k = \frac{2\pi}{\lambda} \tag{2.50}$$

.

λ	Wavelength
f	Oscillation frequency
k	Wave number

A signal consisting of a number of different frequencies hence might be skewed due to dispersion, as the respective signal fractions travel at different velocities.

2.4.3 Effective values

The effective value is generally used to state the sound pressure (or particle velocity) in terms of numbers. This is done, since the mean value of the very common sinusoidal tones is zero and maximum values are hard to measure. Equation 2.51 shows, how the effective value of the sound pressure fluctuations calculates.

$$p_{eff}^2 = \frac{1}{T} \int_0^T p^2 \, \mathrm{d}t \tag{2.51}$$

2.4.4 Sound fields and sound propagation

The condition of an ideal gas is defined by its density ρ_g, its temperature T_g and its pressure p_g. As mentioned before, sound consists of very small, temporally and spatially distributed variations of the reference values (Equations 2.52 to 2.54).

$$\rho_g = \rho_0 + \rho(x, y, z, t) = \rho_0 + \rho' \tag{2.52}$$

$$T_g = T_0 + T(x, y, z, t) = T_0 + T' \tag{2.53}$$

$$p_g = p_0 + p(x, y, z, t) = p_0 + p' \tag{2.54}$$

The ideal gas law (Equation 2.55) relates temperature, density and pressure to each other.

$$p_g = R\frac{\rho_g T_g}{M_{air}} \tag{2.55}$$

As heat conduction can be neglected virtually always in gases, sound events are adiabatic (Equation 2.56.

$$\frac{p_g}{p_0} = \left(\frac{\rho_g}{\rho_0}\right)^{\kappa} \tag{2.56}$$

Since the fluctuations due to sound are exceptionally small in relation to the reference values, elements of higher order as well as products of field quantities have virtually no effect within the hearing range. Equations 2.55 and 2.56 can hence be linearized to equations 2.57 and 2.58, which show that temperature, pressure and density feature similar signal shapes, which differ only by scaling constants.

$$\frac{p}{p_0} = \frac{\rho}{\rho_0} + \frac{T}{T_0} \tag{2.57}$$

$$\rho = \frac{p}{c^2} \tag{2.58}$$

The changes in density ρ result from deflections ζ being different at different positions. Equation 2.59 governs the one-dimensional case.

$$\rho = -\rho_0 \frac{\partial \zeta}{\partial x} \tag{2.59}$$

The increase in density hence stems from local dynamic "packing" of the fluid. Applying Newton's momentum law on an infinitesimally small cube filled with gas yields equation 2.60.

$$\rho_0 \frac{\partial^2 \zeta}{\partial t^2} = \rho_0 \frac{\partial v}{\partial t} = -\frac{\partial p}{\partial x} \tag{2.60}$$

Combining the second time derivative of equation 2.59 with the first spatial derivative of equation 2.60 yields the one-dimensional wave equation (2.61), solutions of which are general wave functions (Equation 2.62).

$$\frac{\partial^2 p}{\partial t^2} = c^2 \frac{\partial^2 p}{\partial x^2} \tag{2.61}$$

$$p = f(t \pm x/c) \tag{2.62}$$

For pure tones with an angular frequency ω, these functions become

$$p = p \pm \hat{p}cos(\omega(t \pm x/c)) = p \pm \hat{p}cos(\omega(t \pm kx)) \tag{2.63}$$

As the frequency range audible for humans starts at 16Hz and ends at about 16kHz, relevant wave lengths λ are approximately $20m > \lambda > 0.02m$. Expanding equations 2.59 and 2.60 by two dimensions yields the three-dimensional wave equation (2.64).

$$\Delta p = \frac{\partial^2 p}{\partial x^2} + \frac{\partial^2 p}{\partial y^2} + \frac{\partial^2 p}{\partial z^2} = \frac{1}{c^2} \frac{\partial^2 p}{\partial t^2} \tag{2.64}$$

Two solutions of equation 2.64 for basic sound fields are briefly discussed in the following.

Firstly, there is the plane wave, which means that all movement is directed in one direction only and all quantities only depend on one coordinate (Figure **??**).

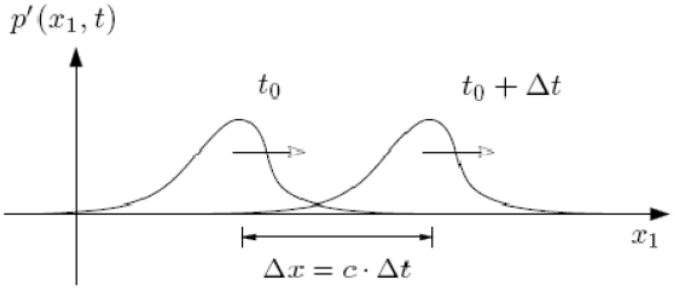

Figure 2.15: Propagation of a planar wave

If one choses x as this coordinate, equation 2.64 simplifies to equation 2.65, with equation 2.66 as solution.

$$\frac{\partial^2 p'}{\partial x^2} = \frac{1}{c^2}\frac{\partial^2 p'}{\partial t^2} \tag{2.65}$$

$$p' = Acos\left(\omega\left(t - \frac{x}{c}\right)\right) = Acos(\omega t - kx) = Re(Ae^{i(\omega t - kx)}) \tag{2.66}$$

It is clear that above equation is only valid for pure tones. This is sufficient, however, as all sounds are merely combinations of various pure tones. Furthermore, equation 2.66 shows that the amplitude is independent from the coordinate, thus saying that the sound pressure does not lessen if the distance from the source is increased.

Planar waves have relatively little relevance in reality, however, as compact sources emit spherical waves. Assuming again that movement only occurs in one, in this case the radial, coordinate direction yields equation 2.67, with $\frac{\partial}{\partial \zeta}$ and $\frac{\partial}{\partial \theta}$.

$$\frac{\partial^2 rp'}{\partial r^2} = \frac{1}{c^2}\frac{\partial^2 p'}{\partial t^2} \tag{2.67}$$

Equation 2.68 is a solution of above equation and it is clear, with r in the denominator below A, that in this case, the sound pressure does get lower with increased distance from the source.

$$p' = \underline{p}' = \frac{A}{4\pi r}e^{i(\omega t - kr)} \tag{2.68}$$

2.4.5 Near field and far field

The sound field can roughly be divided into two regimes, the *near field* and the *far field*. The governing entity is the Helmholtz number (Equation 2.69), which can be understood as the ratio between momentum forces and pressure forces in the sound field.

$$He = \frac{L}{\lambda} = kr \tag{2.69}$$

- L Characteristic length
- λ Wavelength
- k Wave number
- r Distance from the source

In the far field, where $He >> 1$, the momentum forces are stronger than the pressure forces, which positively influences sound emission and propagation. In the near field ($He << 1$), on the other side, the pressure forces are dominant. This inhibits the momentum effects necessary for efficient sound emission and propagation, i.e the effective sound intensity is very low. As the intensity is the product of sound pressure and particle velocity, the reason for this intensity is the $\sim 90^\circ$ phase shift between p and v. Like in AC-electrics, this leads to high reactive power, but little effective power.
It is apparent from equation 2.69 the transition zone between the regimes is at different locations for different frequencies. High frequency waves have high wave numbers, meaning that the Helmholtz number increases quickly and the far field hence starts relatively close to the source.

2.4.6 Model sound emitters

In acoustics, model sound emitters are used to mathematically emulate real sources of sound. Figure **??** shows the three most common shapes: monopoles, dipoles and quadrupoles. Each of said models has its specific real sources, which it approximates well. Complex sources can be modeled by combining these basic types, .

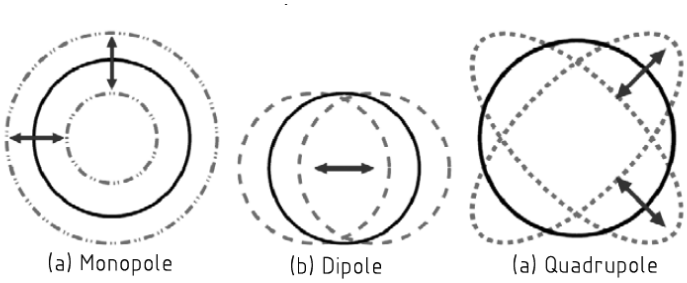

Figure 2.16: Model sound emitters

Many sound sources can be characterized by the time-variant volume flow they provide. Popular examples are car exhausts, fire works or pressure valves. If the dimensions of the source are small relative to the wave length, they can be approximated with a "breathing" sphere, i.e a monopole. The volume flow V is derived via equation 2.70.

$$V = \int_S v \, \mathrm{d}S \tag{2.70}$$

S Source surface

Equation 2.71 describes the pressure variations resulting from the spherical source or monopole. Assuming pure tones yields equation 2.72, which is also used in conjunction with Fourier transformations. The distance between the center of the source and the observer is denoted r.

$$p' = \frac{\rho_0}{4\pi r} \frac{\partial Q(t - r/c)}{\partial t} \tag{2.71}$$

$$p' = \frac{j\omega\rho_0}{4\pi r} Q e^{-jkr} \tag{2.72}$$

A dipole corresponds to a small, oscillating body. Equation 2.73 governs a dipole implemented as a small sphere (Radius a) with a radial particle velocity $v = v_0 cos\theta$, while equation 2.74 describes a dipole of general shape. V_k refers to the volume displaced by the body ($4/3\pi r^3$ in case of a sphere) and V_H to the volume that is hydrodynamically moved. There are numerous examples for this type, especially in aeroacoustics: fans, turbines, jet engines, propellers, turbochargers, etc.

$$p'(r,\theta) = -\frac{\omega^2 2\pi a^3 \rho_0}{4\pi r c} v_0 cos\theta \left(1 + \frac{1}{jkr}\right) e^{-jkr} \tag{2.73}$$

$$p'(r,\theta = -\frac{\omega^2 (V_H + V_k)\rho_0}{4\pi r c} v_0 cos\theta \left(1 + \frac{1}{jkr}\right) e^{-jkr} \tag{2.74}$$

Quadrupoles can be understood as an assembly of monopoles or dipoles, they are "breathing" and/or oscillating. Depending on how the underlying monopoles are arranged (Figure quadropoles), on can distinguish between *longitudinal* and *lateral* quadrupoles.

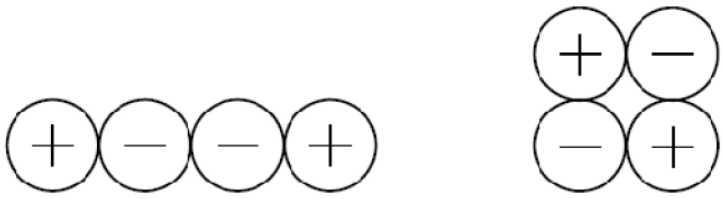

(a) Longitudinal (b) Lateral

Figure 2.17: Types of quadrupoles (Möser and Müller 2003)

$$p(r,\theta,\phi) = -i\frac{k^3}{4\pi} rho_0 c Q \frac{e^{-jkr}}{r} cos^2\theta \tag{2.75}$$

$$p(r,\theta,\phi) = -i\frac{k^3}{8\pi} rho_0 c Q \frac{e^{-jkr}}{r} cos2\theta sin^2\phi \tag{2.76}$$

Q Quadrupole moment

Sound sources that resemble quadrupoles include hot exhausts, pressurized air devices and jets.
As introductorily stated, further types of mathematical sources, so-called multipoles, can be built through various combinations of monopoles, the quadrupole has the most practical relevance, however (see chapter 3 on page 47). Precise modeling of sound sources is is important mainly in the near field as the influence of the source lessens in the far field and there simpler models are often sufficient.

2.4.7 Potency laws

The internationally standardized reference sound pressure $p_0 = 2 \cdot 10^-5 N/m^2$, it is the smallest effective sound pressure detectable by the human ear. On the other hand, sound starts to be painful at $p_{eff} = 200 N/m^2$. The useful sound pressure range hence comprises seven orders of magnitude. Because of this, and, to a lesser extend, because the human body generally detects changes in a certain quantity relative to the quantity's initial size, i.e. the subjective perception is proportional to the logarithm of the objective change in magnitude, sound pressure is generally stated in terms of the *sound pressure level* L_p. This sound pressure level *SPL* is basically the logarithm of the ratio between occurring effective sound pressure and the reference sound pressure. The logarithmic unit used on the SPL scale is decibel (dB), one tenth of the nowadays rarely used unit bel. Equation 2.77 shows how the sound pressure level is derived. The logarithmic scale approximately comprises the range $0 < L_p < 140 dB$.

$$L_p = 10 lg \frac{p_{eff}^2}{p_0^2} = 20 lg \frac{p_{eff}}{p_0} \tag{2.77}$$

The logarithmic scale can be applied on all field and energy quantities, e.g. the sound particle velocity (Equation 2.78).

$$L_v = 10lg\frac{v_{eff}^2}{v_0^2} = 20lg\frac{v_{eff}}{v_0} \tag{2.78}$$

Equation 2.79 shows how n separate sound sources are added to yield a combined SPL in the logarithmic domain.

$$L_{p_tot} = 10lg\left(\frac{\sum_{i=1}^{n} p_i^2}{p_0^2}\right) = 10lg\left(\sum_{i=1}^{n} 10^{\frac{L_{pi}}{10}}\right) \tag{2.79}$$

Figure 2.18 illustrates the logarithmic sound scale's relation to various well-known sound emitters. A change in sound pressure level of one dB is just about noticeable, while a change of three dB is very easily noticeable. Three dB more or less respectively correspond to doubling or halving the sound intensity, i.e. adding or removing a second source (see page 29).

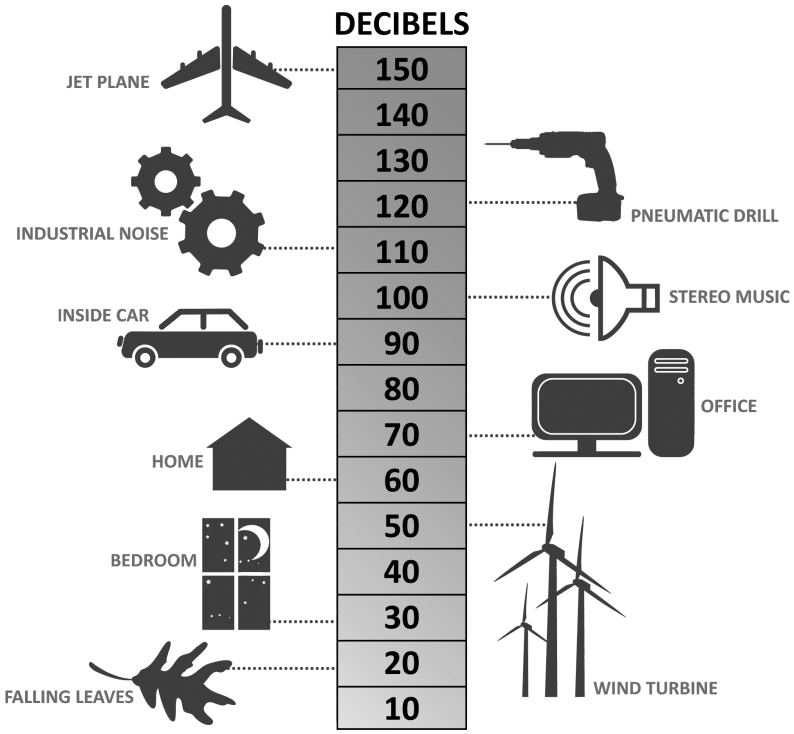

Figure 2.18: Sound scale

2.4.8 Sound spectra

As sound can be decomposed into frequencies or frequency bands, it is conveniently depicted via sound spectra. There are narrow-band, octave and third-octave spectra. In narrow-band spectra, the width of the frequency band in which a measure is given is constant, e.g. 10Hz. Octave (and third-octave) spectra have frequency bands of varying size, it is the ratio between the upper and lower limit frequency of a certain band that is constant (octave: $f_{upper} = 2f_{lower}$, third-octave: $f_{upper} = \sqrt[3]{2}f_{lower}$). These broad-band spectra are a remainder from the days, when narrow-band analysis was technically difficult, but are still very common. There are standards for octave bands, defined by their center frequency. As an example, figure 3.1(b) on page 51 shows a narrow-band spectrum.

2.4.9 Weighting

The sound pressure level alone is not sufficient to describe how the human ear reacts to sound. To predict when sound becomes noise, so to speak, several factors need to be considered. Naturally, acoustic sound properties play an important role, but also other aspects are very important, like, among others, time and place of the sound event as well as the physical and mental condition of the person(s) exposed to the noise. In fact, non-acoustic factors can influence the human reaction more strongly than acoustic ones. Furthermore, there is a strong frequency dependency in the perceived loudness level, which is given in terms of the psychoacoustic unit *phon*. Figure 2.19(a) shows that tones at high and low frequencies are perceived to be quieter than tones around 1kHz. This property of the human hearing is accounted for through weighting filters. There are several different filters, all of them made for special noise conditions, but A-weighting has emerged as somewhat of a standard and is commonly used. Figure 2.19(b) depicts how weighting filters lessen the influence of certain frequencies. The A-weighting functions is roughly the inverse of the constant loudness curve at 40 phon. The changes made to the spectra are governed by equations 2.80 and 2.81(REF), where $A(f)$ means a reduction in sound pressure level (as a function of frequency) due to weighting. To indicate that a sound pressure level underwent weighting, it is correspondingly indexed, e.g. L_{pA}. An important international weighting standard is the perceived noise level PNL.

$$R_A(f) = \frac{12200^2 \cdot f^4}{(f^2 + 20.6^2)\sqrt{(f^2 + 107.7^2)(f^2 + 737.9^2)}(f^2 + 12200^2)} \tag{2.80}$$

$$A(f) = 2.0 + 20 \lg R_A(f) \tag{2.81}$$

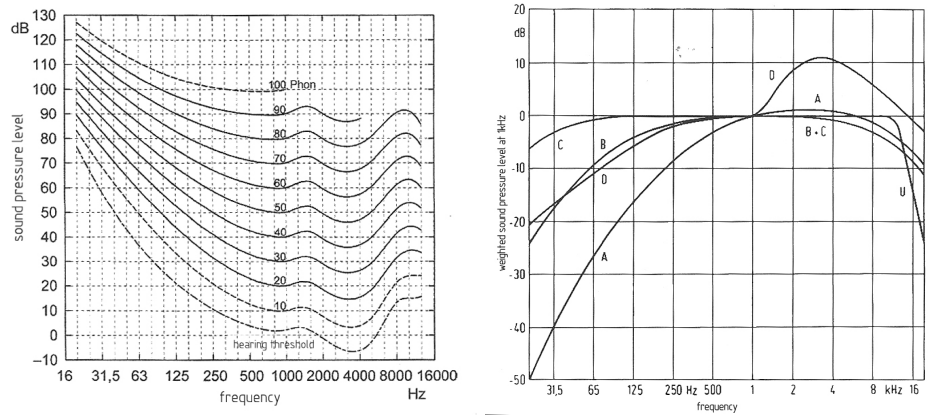

Figure 2.19: Curves of constant loudness (left) and weighting functions (right) (Möser and Müller 2003)

The sound pressure level is rarely constant but varies strongly with time. For the sake of simplicity and in order to provide comparability, it is common practice to use the temporal average, i.e. the equivalent continuous sound measure L_{peq}(Equation 2.82) or L_{pAeq}, if A-weighted. It is defined as the sound pressure level of a constant sound that over a certain period of time would emit the same sound energy as the varying noise in question. This equivalent level correlates well with the actual effect of the sound, but to sufficiently describe a sound event it is often necessary to add (or subtract) adjustment constants K that regard further influences. These influences include peaks (K_I), tones (K_T), contained information (K_{inf}) or the time of the day (K_R). These constants are standardized and can be looked up in tables. The sum of L_{peq} and the added constants is called *rating level* L_R, equation 2.83 shows a possible configuration.

$$L_{peq} = 10lg\left[\frac{1}{T}\int_0^T \frac{p^2(t)}{p_0^2}\,\mathrm{d}t\right] dB \tag{2.82}$$

$$L_R = L_{peq} + K_I + K_{inf} + K_R \tag{2.83}$$

2.4.10 Aircraft noise

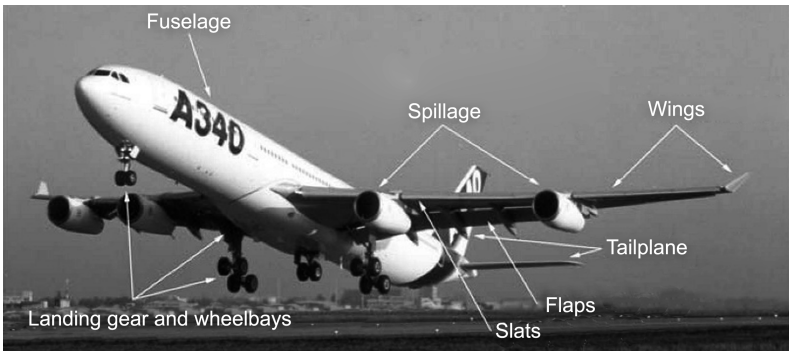

Figure 2.20: Non-propulsion related noise sources of an aircraft.

Figure **??** depicts various noise generators of an aircraft in take-off or landing configuration. Obviously, the non-aerodynamic landing gear in conjunction with its housings causes noise emissions. The same is true for lift-enhancing devices like slats or flaps as well as the boundary layers on the fuselage and the wings. But even though noise stemming from landing gear and extended flaps can gain significant relative importance in modern planes, the engines are still the major contributer to total aircraft noise. Engine noise can itself be split up and assigned to various sources within the engine. The respective noise contributions of these sources depend on the situation or maneuver the aircraft is in (Figure 2.21(b)). During take-off, when the engine is operated at full throttle, fan and jet are almost exclusively responsible for the noise, while during approach, at around 50% throttle, turbine, compressor and even the combustion chamber (below 800Hz) play a role (Möser and Müller 2003). The basic noise generation processes taking place in a turbofan, the engine configuration currently state-of-the-art (Figure 2.21(a)), are briefly explained in the following (NASA 1999).

During operation, air is sucked into the nacelle, or casing, by the fan. The fan blades cut through the air like propellers and, in doing so, produce a broad-band noise with several peaks in the spectrum. Peaks occur at the blade passage frequency (BPF) and its higher harmonics. Upon exceeding of the sound barrier by the blade tips, tones appear also at multiples of the fan speed (angular frequency). Additionally, in order to straighten the then swirly air in the outer duct (or fan duct), a stator ring is installed right after the fan. The individual wakes of each fan blade 'crash' into the stator blades much like the surf on a beach. These recurring events also emit noise with

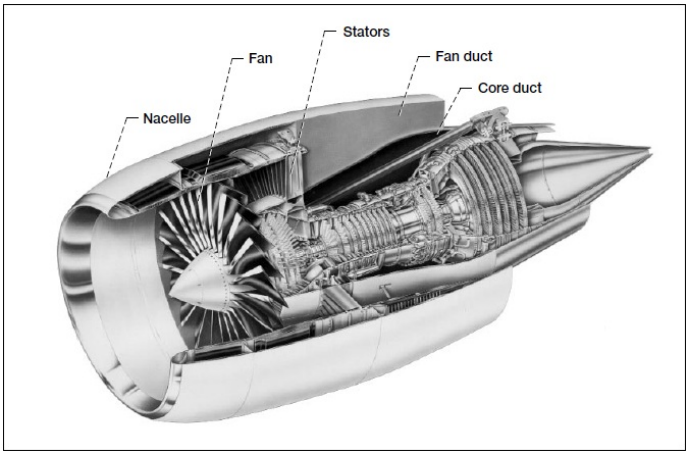

(a) Cutaway of a turbofan engine.

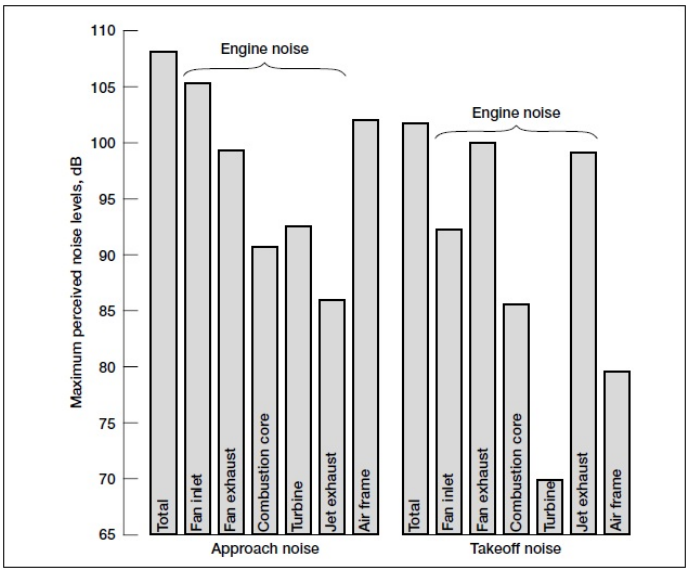

(b) Noise contribution of various areas.

Figure 2.21: Noise contributions of jet engine parts (NASA 1999).

peaks at the BPF and its multiples. The air that is led into the combustion chamber passes a number of compression stages, i.e. rotor/stator couples, where sound is generated in a fashion similar to the aforementioned situation in the bypass. Burning the gas/air mixture is a further source, emitting mainly low frequency noise. The high enthalpy exhaust gases then drive the turbine, which, again, consists of a combination of rotors and stators. As a jet engine is effectively a canal, it is important to understand how and if the sound waves generated by internal sources are able to propagate. Careful assessment of the sound field's modes yields very useful design guidelines, e.g. for the ideal ratio between the numbers of stator and rotor blades or maximum tip speeds. This detail work has reduced the roughly tonal sound stemming from the rotation to such an extend that previously secondary broad band noise resulting from the trailing edge or the fan feed, among others, somewhat emerged as the future challenge (Möser and Müller 2003). The major source of engine noise, however, is the jet leaving the engine through the outlet and subsequently mixing with the surrounding air.

Jet noise is understood as the sound emission due to to the mixing of fast (and usually hot) exhaust gas with slower (or stagnant) ambient air. The sound generation in mixing layers is still not thoroughly understood and the precise location of the noise source hence not easily determined. In a turbulent jet, the origin of the sound emissions lays in the mixing layers (Figure 2.22(a)). The mixing layers emerge virtually directly after the outlet and grow linearly. Close to the outlet the characteristic length scales of the turbulence are small, which means that the higher frequencies of the resulting spectrum originate mainly in this area. The wider the mixing layers get, the larger the turbulent structures become, meaning that the emissions' frequencies decrease. Highest source strength is assumed to occur right after the end of the potential core, about six nozzle diameters downstream.

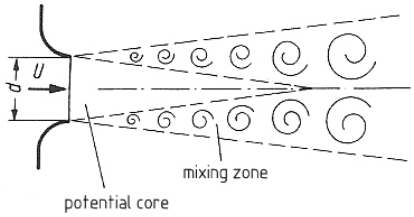

(a) Potential core and mixing zone of a jet

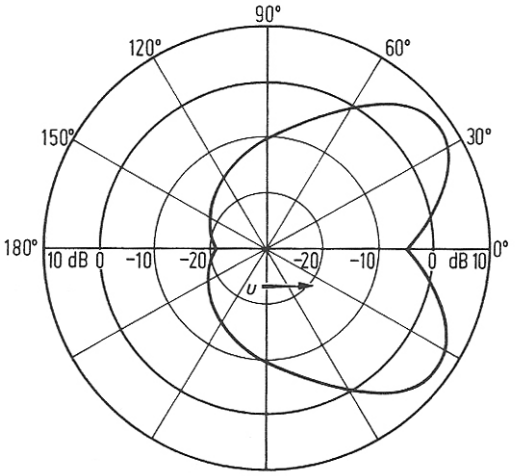

(b) Directional dependence of the noise

Figure 2.22: Jet noise (Möser and Müller 2003)

Given unobstructed flow, the emitted sound is broadband, while obstacles in the potential core can trigger tones that would increase the sound power by up to 20dB. At least in the area $0.7 < \textit{Mach number} < 1.6$ the noise exhibits a significant directional dependence (Figure 2.22(b)). In the same Mach number range, the sound power P increases proportionally to the 8th power of the outlet velocity. This so-called 'M8'-law is the famous result of Lighthill's acoustic analogy (Lighthill 1952). This acoustic analogy is basically a mathematical model that establishes a causal correlation between the flow field and the noise field. It has been reworked numerous times and sometimes criticized, but early works resulted in source terms resembling dipoles or quadrupoles, an intermediate step towards the mentioned 'M8'-law. Whether the source is more akin to a dipole or a quadrupole depends on the flow velocity and on the position within the jet. In the main jet quadrupoles are dominant, while vortexes close to the outlet are rather dipoles. At lower

velocities (*Mach number* < 0.7) the flow now noise is covered up by noise due to said outlet vortexes. If dipole-sources are dominant, the sound power is proportional to the 6th power of the velocity. Consequently, the most effective measure to reduce mixing noise is to lower the jet velocity. In order to provide thrust at all, the outlet velocity has to remain higher than the cruising speed of the aircraft (Equation 2.84).

$$\boldsymbol{F}_T = \dot{m} \underbrace{(\boldsymbol{v}_j - \boldsymbol{v}_0)}_{>0!} \tag{2.84}$$

$\boldsymbol{F}_T$ Thrust vector
$\boldsymbol{v}_j$ Velocity of the jet
$\boldsymbol{v}_0$ Aircraft speed relative to the surroundings

Keeping the thrust constant when lowering the speed naturally requires larger nozzle diameters. The sound power of a jet with constant thrust changes with the fourth (dipole) to the sixth (quadrupole) power of the jet velocity. Lower velocities also lead to lower frequencies of the sound emissions, which is positive as weighting functions scale down the magnitudes of low frequencies. Apart from velocity reductions, which effectively require a complete redesign of the engine, mixing enhancers are a valid way to lower noise emissions. Lobed nozzles, for example, reduce noise, but sacrifice too much thrust in doing so. Turbofan engines offer the possibility to merge the bypass and the core flow within the outer duct, thus "keeping the mixing noise inside". The most promising development are nozzle chevrons, however. They are assumed to induce stream wise vortexes and have shown to reduce the noise emissions notably with close to zero thrust loss. Previous works dealing with nozzle chevrons are reviewed in **??**, starting on page 47.

3 Literature review

3.1 General

Aeroacoustics as a sciency, also covering jet noise, emerged some sixty years ago. Correspondingly, analysis strategies and experimental techniques have seen very significant advancements and, naturally, the knowledge about 'what is going on' in a jet has hence grown tremendously. **jordan** and Suzuki (2010) independently from each other reviewed the field of subsonic jet noise and presented summaries of the various diagnostic studies carried out over the years, the remaining uncertainties and future goals. To provide some context for the present work, this general section of the chapter aims at explaining the current state of affairs, mainly based on said two works. Thereafter, a small number of research papers relevant to the topic investigated here is discussed in more detail.
Everything seems to have started with Lighthill's famous acoustic analogy that proposes a sound-generation mechanism for jet noise (Suzuki (2010), Lighthill (1952); Equation 3.1 and *Lighthill's stress tensor* in equation 3.2) It effectively recasts the Navier-Stokes equations into an inhomogeneous wave equation. Sufficiently far away from the source (the jet), the left-hand side is equal to an acoustic field that is driven by the dissipation term on the right-hand side.

$$\frac{\partial^2 \rho'}{\partial t^2} - a_\infty^2 \frac{\partial^2 \rho'}{\partial x_j^2} = \frac{\partial^2 \boldsymbol{T}_{ij}}{\partial x_i \partial x_j} \tag{3.1}$$

.

$$\boldsymbol{T}_{ij} \equiv \rho u_i u_j + \left[(p - p_\infty) - a_\infty^2 (\rho - \rho_\infty) \right] \delta_{ij} - \sigma_{ij} \tag{3.2}$$

.
Due to the behavior of the source term the sources came to be understood as quadrupole elemental deformations connected to turbulent eddies. Furthermore, these sources were considered acoustically compact, i.e. with a spatial

extent smaller than the wavelength of the emitted sound. Furthermore, they were assumed to be convected by the flow, thus leading to stronger radiation in downstream direction. Many other researchers reworked this acoustic analogy in order to better describe the source or take into account the interactions between the 'source' and the base flow. Others based their own analogies on altogether different mechanisms, e. g. vorticity. The temperature of the jet is considered to play a role as well, with dipole source terms accounting for it, but Viswanathan (2004) showed that it may not be the temperature itself but rather the Reynolds number change due to the temperature that influences the noise emission. All the analogies have in common that they linearize the base-flow and define the difference between this base-flow and the exact compressible Navier-Stokes equations as the source term. It is still controversial, what constitutes an optimal source definition. Even for purely experimental works, Lighthill's equation and theoretical models in general are very important because they give an idea of the sound emitting structures in the mixing layer and hence assist the hardly straight-forward process of measurement data interpretation.
Several years after these initial consideration researchers started to become aware of larger, coherent structures in the mixing layers and it was eventually universally accepted that these large coherent structure where sources of jet noise. Analogies with source terms based on these large structures agreed well with experiments, showing peak radiation at small angles from the jet axis. Note that the exact nature of these coherent structures is still unclear. Suggestions include vortex pairing or instability waves, among others. Tam (1998) pointed out the possibility of two source mechanisms, large structures *and* compact turbulence. This duality poses problems in source modeling and it is still unclear how to relate experimental results to the respective source mechanism. Also, it was suggested by many that the collapse of the annular mixing layer just after the potential core might by an event violent enough to be a dominant noise source. Guj et al. (2003), Hileman et al. (and 2005) have, among others, experimentally proven that noise was produced in this area. They also observed strong intermittency. As stated above, the hypothesis of the separate noise sources in the mixing layer, small scale turbulence behaving like quadrupoles, and large coherent structures of various form, remains a hypothesis. To get further in this question, the experiment is still the essential means, despite impressive progress in numerical modeling. Simultaneously measurements of flow variables and the far field pressure cast some light on this matter. The so called causality method uses formal relationships between far field autocorrelation, flow-acoustic cross-correlation and the acoustic analogy to predict the sound field. Hot-wire, hot-film or in-

flow pressure probes were used in conjunction with far field microphones in early attempts. Correlation computations showed that high frequency noise were radiated from upstream positions, while downstream lower frequencies dominated. Again, the transition region after the potential core was found to be a strong noise emitter. When using an intrusive measuring method like hot-wire anemometry, there is always the risk to produce more noise by the probe than the sources in the flow would. Hence, special-made low intrusion probes or completely non-intrusive methods like laser Doppler anemometry (LDA) were used. The results of these works more or less agreed that the transition area right after the potential core yielded the highest correlations with the far field, thus implying strong sources in that area. Juvé et al. (1980), Panda et al. (2005) and others found these sources to be highly intermittent, meaning that 50% of the noise is produced in 20% of the time. This intermittency would render statistical source models insufficient to describe the full dynamics. Moreover, an intermittent source would elude meaningful description by a second order averaging technique, e.g. RMS. Guj et al. (2003) therefore used conditional averaging to look for correlations between sound and velocity measurements. The authors also found that the main source should be located in the region after the potential core. Near field microphone measurements just outside the jet are further means of investigation. The main advantages of this method are the measured pressure fluctuations' being scalars and the fact that "smaller turbulence scales are ineffective in driving the flow in this region". This mechanism is filtered out via a still poorly understood effect, leaving the coherent structures for investigation. The measurements are difficult to interpret, however, as there are contributions from both 'hydrodynamic' and 'acoustic' pressure fields. Tinney and Jordan (2008) discussed this in some detail. **arnd**, Harper-Bourne (2004), Coiffet et al. (and 2006) proposed Helmholtz numbers $1 < kr < 2$ to mark the change between the domains (k = wave number; r = radial distance from the center of the mixing layer to the microphone). Research led to the conclusion that the near field can be considered a superposition of convective ("hydrodynamic") and propagative ("acoustic") components.
High Reynolds number jets are still too complex for direct numerical simulation (DNS), but the less exact, but increasingly powerful and popular large eddy simulations (LES), that due to a coarser mesh can only compute the larger turbulence structures and ignores or models the finer scale contributions, yielded impressive results. Simulations done by Bogey and Bailly (2004), for example, resulted in the transition region after the core being a strong intermittent source. This is in agreement with experimental studies.
In a nutshell, the above means that despite significant progress, uncertainties

remain regarding the definition of the sources mechanisms and how to best mathematically describe them. **jordan** proposes in the concluding remarks of their work a three-phase approach for future investigations: The first phase includes in-depth theoretical analysis and problem definition; in the second phase the theoretical possibilities are exploited as much as possible using numerical investigation; finally, the third phase is about experimental verification of the simulations, directly aimed at answering questions that arose in the foregone phases.

3.2 Relevant works

Callender et al. (2005) investigated the impact of nozzle chevrons on far-field noise. On a coaxial testing rig, they compared three serrated core nozzles, differing in lobe number and penetration depth (Figure 3.1(a)), to a baseline nozzle. A constant distance (3,81m radius) microphone array, covering a 90 degree section of the surroundings, was used to determine the far-field noise (Figure **??**). In these investigations, it was found that, generally, chevrons reduce noise at Strouhal numbers between 0.1 and 1, while increasing it at higher frequencies (Figures 3.1(b) and 3.1(d)). Directivity analyses of the overall sound pressure level $OASPL$ show that the greatest attenuations are achieved at aft angles. This is in agreement with the spectral results, as lower frequencies mainly propagate to aft angles and higher frequencies are more dominant upstream. This shift indicates that the serrations modify the jet plume and its noise-generating mechanisms. The stated effects are found to be highly dependent on the conditions present, however. The magnitudes of the changes in the spectra increase with the Mach number as well as with increased penetration depth. The perceived noise level PNL directivity plots of the single flow measurements show that serrated nozzles actually increased the SPL at upstream angles, i.e. that excessive velocity differences lead to substantial high frequency noise increases, which cannot be compensated by low frequency gain (limited by weighting) any more (Figure 3.1(c)).

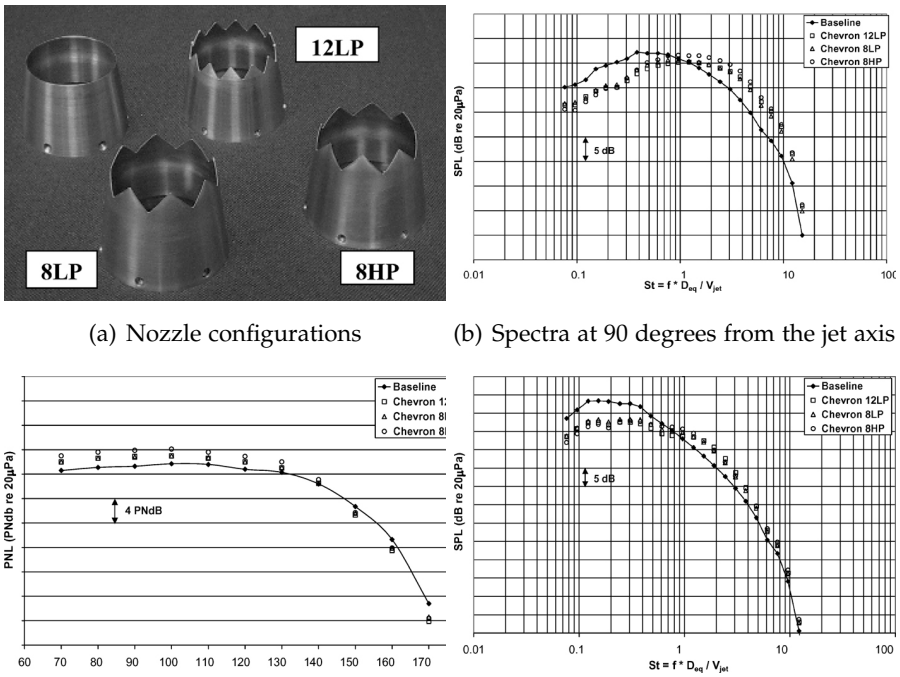

(a) Nozzle configurations

(b) Spectra at 90 degrees from the jet axis

(c) Directivity

(d) Spectra at 30 degrees from the jet axis

Figure 3.1: Callender et al. (2005)

Tinney and Jordan (2008) carried out pressure measurements in the near field of high Mach number subsonic, coaxial jets. The work strove to better understand the near pressure field of the jet and employed circular as well as line arrays of microphones (Figure 3.2(a)). Two different secondary nozzles were investigated, with and without serration. In terms of protrusion depth, Tinney's serrated nozzle is most likely situated in between the two serrated configurations of the present work. It was found that the near field OSAPL is reduced by the serration and that there is a stark change in the coherence spectra at $Str = 0.75$ (Figure 3.2(b)), which implies the presence of a low-frequency hydrodynamic regime and a high-frequency acoustic regime. The researchers went to great length to separate the two regimes. To this end, the pressure fields $p(x,t)$ were displayed in a wavenumber-frequency domain $p(k_x, f)$ using spatial and temporal Fourier transformations (k_x is defined as the axial wavenumber). Arguing that acoustic fluctuations could never convect supersonically, the speed of sound of the ambient air a_a was defined as the boundary between the two regimes in figure 3.2(c). a_a corresponds to the dashed line in the figure and the above left region, characterized by

subsonic convection speeds ($f < k_x a_a$), can be associated with the hydrodynamic regime, while the region on the other side of a_a corresponds to the supersonic acoustic pressure fluctuations ($f > k_x a_a$). After assorting the frequencies and wave numbers to their respective regimes in the fk_x-space, inverse transformation yields the desired separated pressure fields (hydrodynamic and acoustic). The serrations were found to lower the magnitudes of the low-frequency, coherent fluctuations, which is in accordance with the universally assumed effect of nozzle serrations. Note that in order to divide the total pressure field into its hydrodynamic and acoustic components, spatial information about the pressure fluctuations $p(x)$ is required.

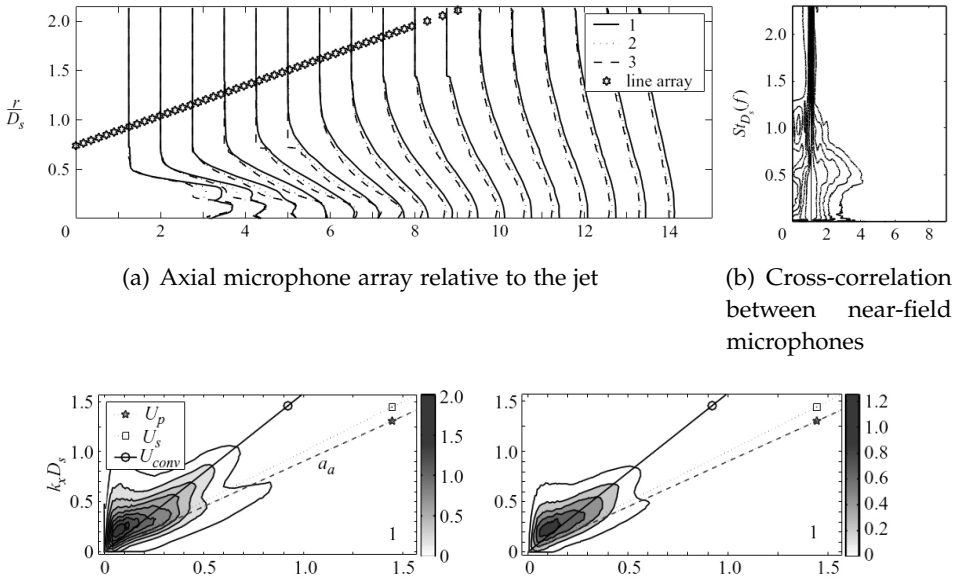

(a) Axial microphone array relative to the jet

(b) Cross-correlation between near-field microphones

(c) $k_x - f$-spectra

Figure 3.2: Tinney and Jordan (2008)

Tam et al. (2008) published an extensive work on jet noise, based on the assumption that the characteristics of the noise source are imprinted on the far field. The researches investigated microphone data autocorrelation, cross-correlation between microphones and cross-correlation between microphones data and flow data stemming from the Rayleigh-scattering technique. The work aims at supporting the known hypothesis of two separate noise sources in the mixing layer, namely fine-scale turbulence emitting sound omni-directionally and large, coherent structures, which emit strong noise at roughly a thirty degree angle from the jet axis, thus rendering the total

noise emission highly directive. The results show all types of correlation to be strongly direction-dependent . Microphone autocorrelation plots show narrow peaks at fore angles and broader peaks at aft angles, hinting at larger, more organized structures being emitted in this direction. Microphone cross-correlation results agree with that, as the cross-correlation only reaches notable values if both microphones are located at aft angles. Also the noise-flow measurement show hardly any correlation outside of this region and, again, considerable correlation within it.

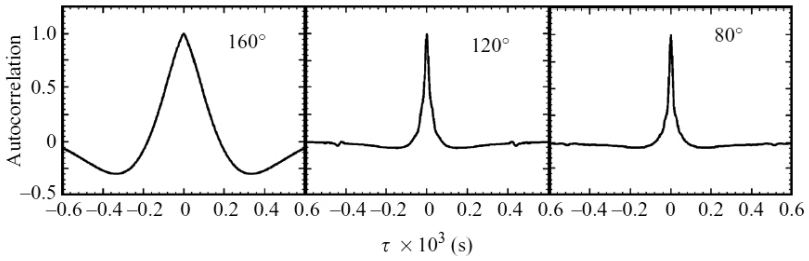

(a) Microphone autocorrelation at three different angles

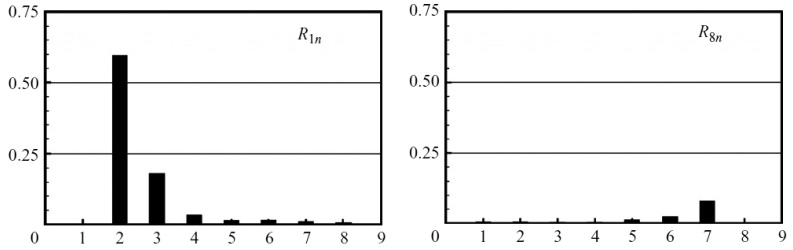

(b) Microphone cross-correlation. In the left plot the microphone at 160 degrees is the reference, in the right one the microphone at 80 degrees.

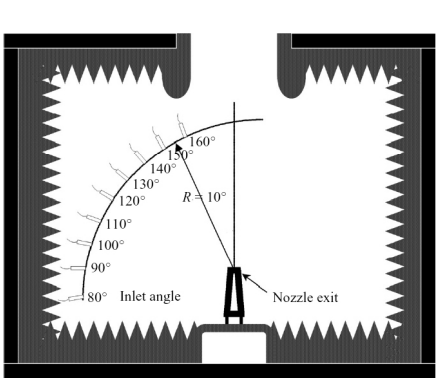

(c) Schematic of the test layout

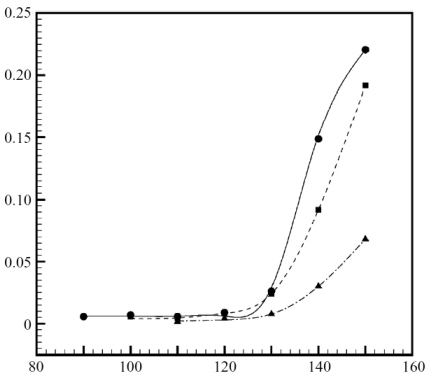

(d) Flow-noise cross-correlation as a function of emission direction.

Figure 3.3: Tam et al. (2008)

Guj et al. (2003) did simultaneous noise-flow measurements using microphones and a hot-wire probe. To account for the expected intermittency of the noise generation, they searched the raw sound data for peaks that fulfilled a set of certain requirements. Samples of a certain length including such peaks were cut out and condition averaged. The time values at which peaks occurred in the noise data were used to extract samples from the velocity data, which were condition averaged as well. Phase shifts and time delay

were then used to compute the location of the noise source. Results strongly indicate that the source is in the transition zone after the potential core.

Zaman (2012) did thorough flow measurements of rectangular jets, including jets stemming from serrated nozzles.

All tests were carried out at the University of Adelaide, Holden laboratory (School of Mechanical Engineering) and all the equipment was provided by this institution as well. Apart from the nozzles, i.e. the specimens, said equipment consisted of an anechoic wind tunnel, microphones, hot wire anemometers and all the necessary supply, calibration, mounting and data acquisition infrastructure. As roughly outlined in the introduction, the investigation was broken down into three parts, namely pure velocity, pure sound and simultaneous velocity-sound measurements. The sound investigation was further divided into near-field, far-field and directivity sections. It is the aim of this chapter to provide an instructions manual that would allow the reader to repeat the experiments if the need arises.

4 Test facility and measuring equipment

4.1 Anechoic wind tunnel

Figure 4.1: The anechoic wind tunnel and its peripheral devices in the laboratory of the University of Adelaide

The purpose of an anechoic facility is to simulate free-field conditions, i.e. that the reflected sound does not interfere with the sound from the investigated noise source. In the present work, the small scale anechoic open-circuit wind tunnel (AWT) of the University of Adelaide is used. Figure 4.2(a) shows the layout of the wind tunnel and its air supply (The diffuser is in the planning stage at present). A 1.7kW FanTech (27B B1) centrifugal fan equipped with a redial blade impeller (diameter = 685mm) is used, which

provides a maximum of about 0.825 m^3/s and a maximum static pressure of 2kPa. Fan speed is controlled with a Vacon NXL-series. The fan is enclosed by a plywood box to minimize noise emission into the laboratory. To reduce flow noise, a silencer is installed after the fan. It consists of a 8m long duct with a cross-section of 400mm x 400mm and 5 90° bends. A flow noise reduction of at least 50dB(A) is hence in the range from 200Hz to 2kHz. Finally, to reduce turbulence a settling chamber is mounted directly after the silencer and in front of the outlet contraction. It contains a honeycomb made of drinking straws and a series of gauze screens. The AWT itself is a cube with an outer side length of slightly more than two meters. Its inner walls are lined with polyester wedges for sound insulation, which yields an actually available measuring volume of a bit more than two and a half cubic meters. Said insulation elements are 300mm high and have a 100mm x 100mm base (Figure 4.4(b)). Thus equipped the facility should be anechoic at frequencies above 200Hz. (Moreau et al. 2012) carried out a free-field characterization of the facility, i.e. how closely the conditions in the tunnel follow the free-field law. This law states that there is a 6dB reduction in sound pressure level every time the distance from the source is doubled. The results show a slight deviation form the ideal decay function at 200Hz, but the facility can be considered anechoic at 250Hz and above (Figure **??**). Figure 4.2(b) shows a cross sections of the wind tunnel. Straightened and silenced airflow enters the tunnel through the main contraction (A), which provides a 275mm x 75mm free jet with a turbulence intensity of about 3%. This mentioned maximum flow rate of about 0.825 m^3/s would yield a maximum velocity of about 40m/s at this point. Note, that the additional contraction needed and specifically made for this jet noise investigation is already included in this view (B). A sheet metal collector (B) directs the air out of the chamber and, for raster measurements of flow variables, a 3-axis traverse system is installed in the anechoic chamber (D, Figure 4.4(a)). The traverse system is a Dantec Dynamics product with a range o 610mm per axis. An external control unit receives and processes the commands that the user issues via specific MATLAB code and subsequently powers the respective stepper motors. These motors feature a resolution of 6.25μm (*Dantec* 2012). Furthermore, two instrument mounting rails run the length of the chamber a few centimeters below the the ceiling. These are not included in the renderings, but can be seen in figure 5.7 on page 5.7. Prior to use, the wind tunnel needs to be calibrated, i. e. a linear relation between centerline flow velocity and the frequency of the electric current fed to the fan must be established. To this end the dynamic pressure at the center line is measured via a pitot tube (Figure 4.5), whose pressure hoses are connected to a Baratron (see

section **??** on page **??**) difference pressure sensor. The flow velocities are computed using the measured dynamic pressures as well as density and temperature of the ambient air. A number of frequency values (e.g. 10Hz, 15Hz, etc.) is manually set at the AWT's control panel to obtain a set of several speed/frequency-couples which are then used to approximate the desired linear relationship.
Despite the sound insulation measures described above, sound measurements were generally done out of the laboratory's operating hours (nights, holidays). The majority of the technical specifications stated above comes from (Moreau et al. 2012).

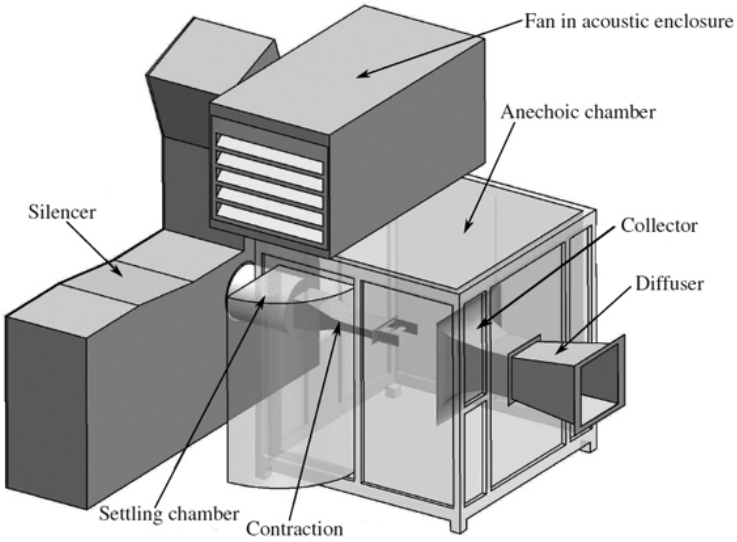

(a) Layout of the AWT and its air supply (Moreau et al. 2012).

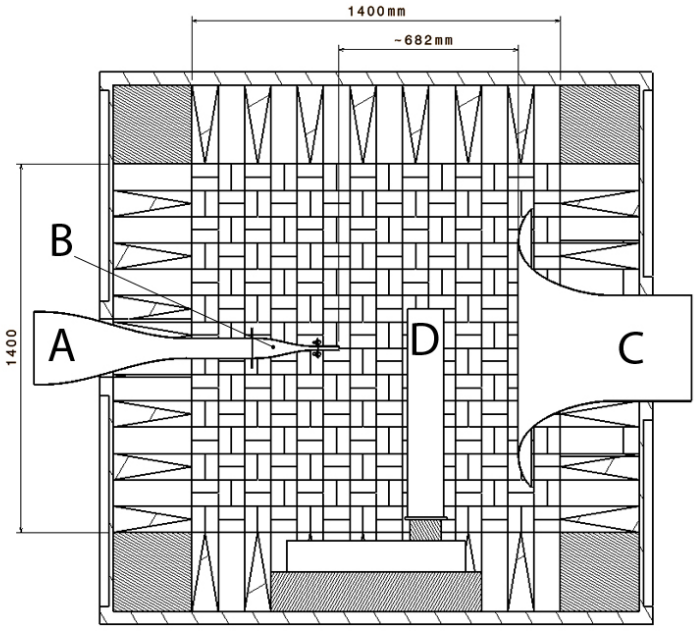

(b) Section of the AWT

Figure 4.2: Anechoic wind tunnel

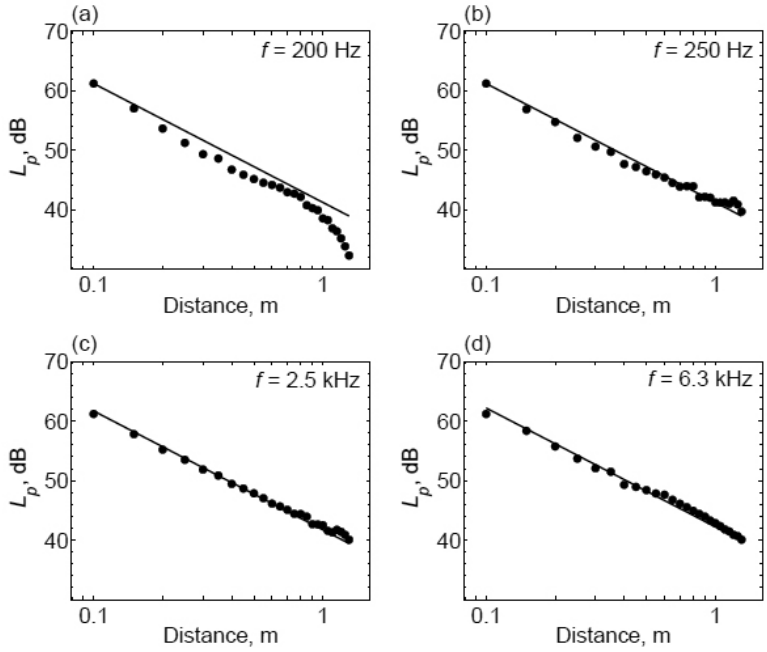

Figure 4.3: Sound pressure level as a function of distance from the source at one-third-octave band center frequencies: (a) f = 200 Hz; (b) f = 250 Hz; (c) f = 2.5 kHz; and (d) f = 6.3 kHz. The solid lines correspond to the theoretical free-field decay (Moreau et al. 2012).

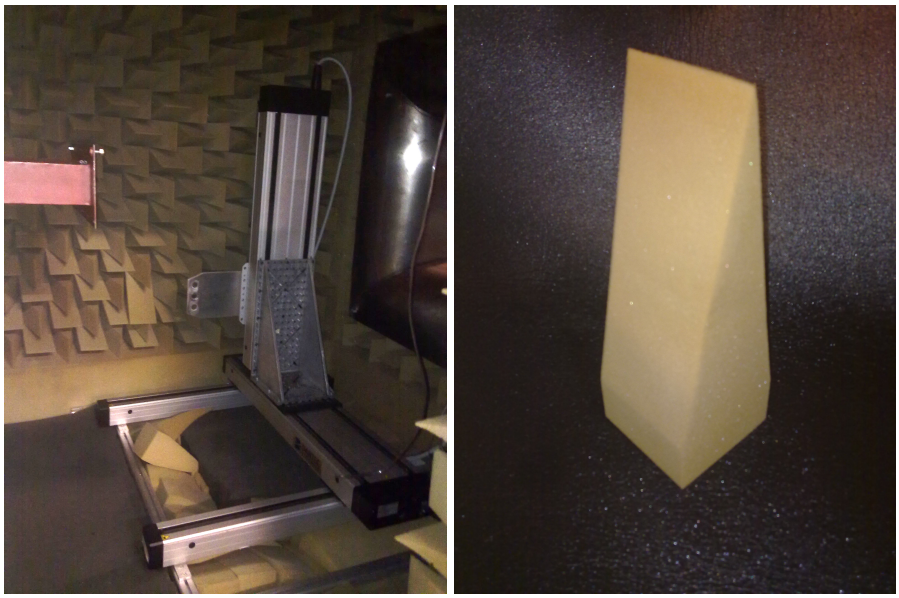

Figure 4.4: Traverse system (left) and sound insulation element (right) of the AWT.

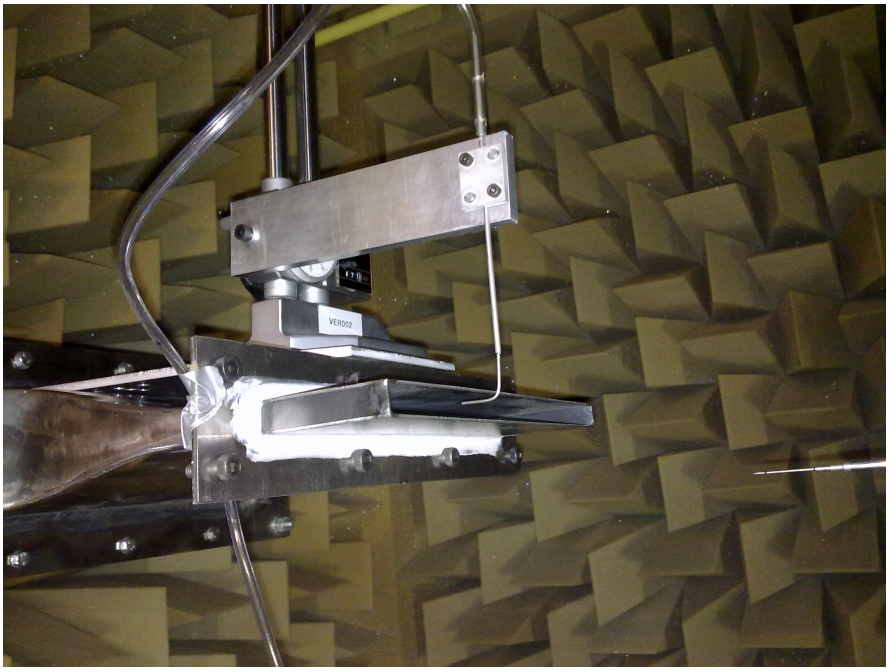

Figure 4.5: The pitot tube and its holder before calibration

4.2 Outlet contraction and nozzles

A university collaborating with the University of Adelaide in the field of jet noise is currently working on elaborate LES-simulations. The outlet dimensions of this simulation were adopted in mutual expectation of comparison and verification possibilities. Therefore, a contraction going from the wind tunnel's 275mm by 75mm air flow supply to the desired 275mm by 13.5mm outlet needed to be fabricated. In order to achieve this cross section change without flow separations at the walls or an increase in turbulence intensity a third-order shape function was used to define the contraction contour. A relatively simple ANSYS analysis was done to verify this. The part is made of 1.6mm sheet steel and features a separable flange, which allows for different 80mm long end pieces of constant cross section to be investigated. The equivalent diameter (according to Huebscher) of the outlet is 53.7mm (Equation 4.1).

$$d_e = 1.3\frac{(ab)^{0.625}}{(a+b)^{0.25}} \tag{4.1}$$

a Major side (275mm)
b Minor side (13.5mm)

Figures 4.6(a) and 4.6(b) show the finished part in baseline configuration prior to and after installation, respectively. Three different outlet configurations were analyzed, namely the flat baseline version, a nozzle featuring straight serrations and another one featuring protruding serrations. Initial considerations about sizing the serrations based on certain flow innate length scales did not yield satisfactory results. Hence, the serration width was simply set to 13,5mm, i.e. the slot height, and the protrusion depth to 1mm (Figure 4.7). The protrusions reduced the nozzle cross-section area by about 7.5%, but the required supply frequency of the fan to reach the desired outlet velocities did not notably change, hinting at a negligible back pressure increase. The end pieces next to their respective CATIA-counterparts are shown in figure 4.8. Note that there were only two end pieces and that the serrations were modified, i.e. made protruding, after all the measurements requiring straight serrations were finished. Furthermore, this nozzle was found to slightly (about two degrees) deflect the flow due to manufacturing mistakes. Fortunately, it was possible to largely correct the resulting errors with MATLAB. No dedicated boundary layer or outlet turbulence intensity investigations were carried out, but the hot wire measurements done close to the outlet give some information in these regard. The leftmost blue curve in figure 6.21(a) on

pageref 6.21(a) gives an idea of the boundary layer thickness in the canal. The profile was obtained about 2mm away from the nozzle and the potential core is still about 12mm high, which hints at boundary layer thicknesses below 0.7mm, probably even less. Figure 6.26 on page 130 shows the turbulence intensities close to the outlet. (See appendix (REF) for all technical drawings).

(a) Finished contraction with plain nozzle

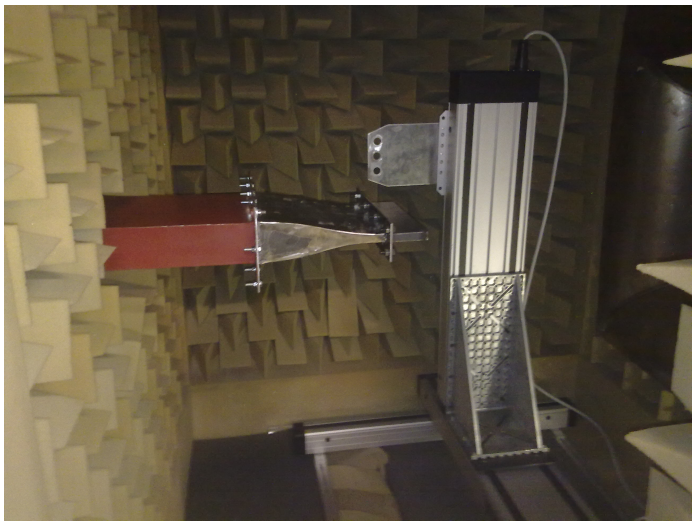

(b) Contraction installed

Figure 4.6: Contraction

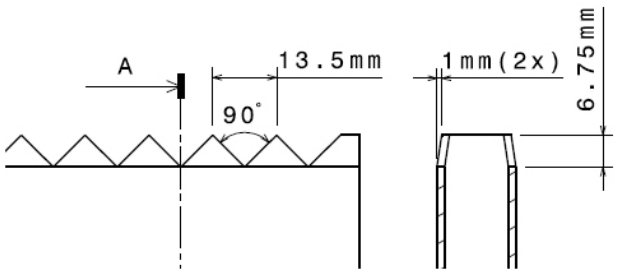

Figure 4.7: Dimensions of the (protruding) serrations.

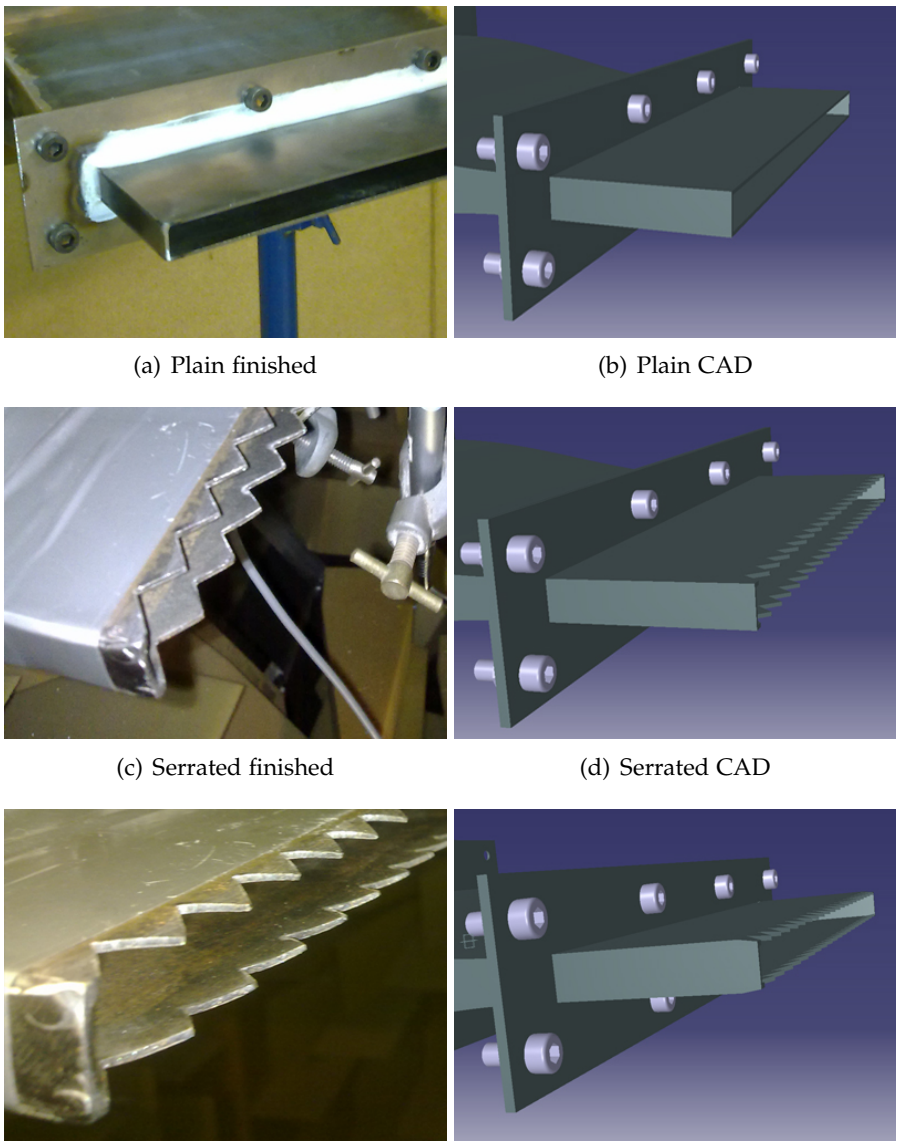

(a) Plain finished (b) Plain CAD

(c) Serrated finished (d) Serrated CAD

(e) Protruding finished (f) Protruding CAD

Figure 4.8: Nozzle configuration overview

4.3 Hot wire anemometry

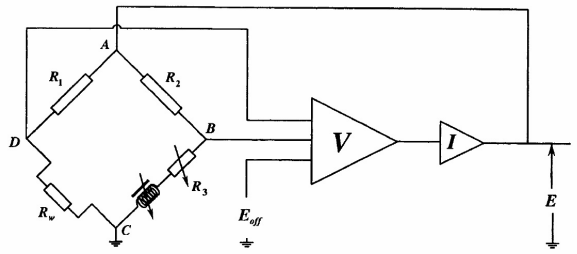

Figure 4.9: Schematic of constant temperature anemometer ("Unsteady Loss in a High Pressure Turbine Stage")

4.3.1 General

With the exception of the wind tunnel calibration, which is done with a pitot tube, hot wire anemometry is used to measure velocities and, consequently, obtain the flow field. This method employs a very thin metal wire that is electrically heated and exposed to the flow. The flow will cool the wire, with the heat transfer depending on the flow conditions. Correlations between the temperature difference, i.e. difference in electrical resistance, of the wire (usually tungsten) and the velocity magnitude can be derived. Depending on the electrical circuit the anemometer is embedded in, several implementations of this measuring principles are possible, namely CCA (Constant-Current Anemometer), CVA (Constant-Voltage Anemometer) and CTA (Constant-Temperature Anemometer). By keeping one variable constant (e.g. temperature), the variations of another (basically heating current) can be directly related to the measurand. CCA and CTA are well established and widely used configurations, with CVA being a more recent development, arguably superior in many respects, but still rather rare. Of the traditional types, CTA is the more common as it is less sensitive to sudden variations in the flow. Hot wire probes are heated well above the flow temperature in order to work efficiently and an abrupt end of the cooling flow can lead to the comparatively inert CCA-probes burning out. On the other hand, sudden exposure to cold flow might cause such probes to cool down to temperatures below their range of efficiency, hence yielding low quality results. For the reasons stated, CTA is used in the present work (Figure 4.9 shows a basic schematic of a CTA). In its most simple form, the setup consists of a Wheatstone-bridge and an amplifier that form a feedback loop. As part of

the calibration, the bridge is compensated by adjusting R3 until points B and D are on the same potential. If then exposed to the flow, the probe is cooled, which is attended by a decrease in electric resistance. This unbalances the bridge, leading to a potential difference between points B and D. The resulting voltage is amplified and reapplied to the the bridge (points A and C), where the increased current reheats the probe until compensation is reached again. The amplified voltage also serves as a velocity dependent output signal. Hot wire anemometry offers high frequency response and is sensitive to very small variations of the flow, i. e. offers high spatial resolution. This renders this method especially useful for obtaining statistical or relative values like turbulence intensity or power spectral density. While the probes can deliver very accurate values over a large velocity spectrum if calibrated correctly, the method is naturally not 100 per cent precise. In their review of the hot wire anemometry, Payne ("Unsteady Loss in a High Pressure Turbine Stage") gives a comprehensive assessment of the measuring accuracy that comprises all the sources of error.

Table 4.1: Error assessment according to ("Unsteady Loss in a High Pressure Turbine Stage")

Error source	*Mach number error (rms)*	*Error in pitch angle (rms)*
Calibration measurement	2.8%	0.1°
Calibration equation	1.8%	1.0°
Calibration drift	4.2%	1.7°
Approximation	Unknown	Small
Spatial resolution	Small	Small
Disturbance	Small	Small
Total error	**5.4%**	**2°**

Table 4.1 shows an overview of their considerations and results. Even though the circumstances of Payne ("Unsteady Loss in a High Pressure Turbine Stage")'s work were naturally different from those of the present work and thus Payne ("Unsteady Loss in a High Pressure Turbine Stage")'s error assessment can only serve as an approximation, it is useful as an estimation aid. According to Payne ("Unsteady Loss in a High Pressure Turbine Stage"), the calibration measurement error is mainly due to drift occurring in the device measuring the dynamic pressure in the calibrator (Baratron; figure 4.15 on 4.15). As the outlet of the calibrator used here is not significantly larger than the X-wire probe, there is most likely a small additional

error due to possible misalignment. The calibration equation used here for the velocity magnitudes is a fifth order polynomial and a fixed effective angle *FEA* (Bakken and Krogstad 2004) method is used to derive the instantaneous flow angle. Payne ("Unsteady Loss in a High Pressure Turbine Stage") apparently relied on similar procedures, hence the expected error should be roughly the same. Calibration drift errors stem from the wires being prone to aging, i.e. changing their electrical resistance while in use, which means that the calibration factors are no longer accurate and the resulting velocity values hence wrong. This could be due to contamination of the wire or bad connections. How fast and how far the measured results deviate from the real values depends on the respective probes and can vary considerably, probes that have been repaired in the past are usually especially affected. It is therefore challenging to obtain entire velocity fields, as this usually takes several hours and can require intermediate recalibrations. X-wire measurements suffer particularly, since the flow angle is a function of the velocity difference between the two wires. Unequal signal drift would thus affect not only the magnitude. If available, a non-intrusive method that is able to capture the entire field at once (e.g. Particle Image Velocimetry) would be a useful supplement to HWA. But as mentioned before, aging of the probes is not constant and sometimes they age very little. Moreover, excessive drift can usually be detected when looking at the results of an investigation and faulty data be discarded. So, again, the error values Payne ("Unsteady Loss in a High Pressure Turbine Stage") proposes should be valid. The approximation error is a accumulation of all the assumptions and simplifications made in the measuring chain, the unavoidable influence the probe has on the flow leads to disturbance errors. The measuring volume of the X-wire probe is approximately a cube with a side length of 1mm, hence one order of magnitude smaller than the dimension defined as the characteristic length scale (13.5mm = 1 slot width). Similar relations are present in Payne ("Unsteady Loss in a High Pressure Turbine Stage"). Taking all the above into account leads to an expected total error slightly above the values in table 4.1.

4.3.2 Theoretical background

c_w	Heat capacity of the wire
T_w	Wire temperature
P	Electrical power
Q	Heat flow
I	Electrical current
R_w	Electrical resistance of the wire
L	Characteristic length (wire length)
d_w	Wire diameter
h	Heat transfer coefficient
T_{adw}	Adiabatic wall temperature
u	Free stream velocity
μ	Absolute fluid viscosity
ρ	Fluid density
c_p	Constant pressure heat capacity
u	Free stream velocity
μ	Absolute fluid viscosity
ρ	Fluid density
c_p	Constant pressure heat capacity
m	Fluid mass flow
Nu_t	Nusselt-number evaluated at total temperature
Re_t	Reynolds-number evaluated at total temperature
Pr	Prandtl-number
Gr	Grashof-number
M_∞	Free stream Mach-number
tau_w	Temperature loading parameter $(T_w - T_{adw})/T_0$
k_t	Thermal conductivity of air evaluated at total temperature
r_w	Wire radius
$A'(T_0), B'(T_0)$	Coefficients depending on total temperature
R_{adw}	Wire resistance at adiabatic wall temperature
R_{ref}	Reference resistance of wire
α_1	Linear temperature-resistance coefficient of wire
η	Temperature recovery ratio (T_{adw}/T_0)

Stainback and Nagabushana (1992) reviewed the hot wire method in some detail. General considerations as well as derivations specifically concerning the case at hand are repeated in the following.

An electrically heated wire exposed to air flow is governed by equation equa-

tion (4.2).

$$\frac{dc_w T_w}{dt} = P - Q \tag{4.2}$$

And further:

$$\frac{dc_w T_w}{dt} = I^2 R_w - \pi L d_w h(T_w - T_a dw) \tag{4.3}$$

Assuming that the temperature of the wire is kept constant leads to equation equation (4.4).

$$I^2 R_w = \pi L d_w h(T_w - T_a dw) \tag{4.4}$$

Heat transfer relationships:

$$Q = f(u, \mu, \rho, c_p, T_w, T_a dw) \tag{4.5}$$

Since μ, c_p, T_{adw} and κ are functions of the total, or free stream, temperature T_0, equation (4.5) simplifies to equation (4.6). The flow velocity in our case is low enough $(M \sim 0.1)$ to assume incompressibility, which yields equation (4.7).

$$Q = f(u, \rho, T_w, T_0) \tag{4.6}$$

$$Q = f(m, T_w, T_0) \tag{4.7}$$

This can be expressed in non-dimensional quantities. When applying the above mentioned assumptions:

$$Nu_t = f\left(Re_t, Pr, Gr, \frac{T_w - T_{adw}}{T_0}, \frac{u^2}{c_p(T_w - T_{adw})}\right) \tag{4.8}$$

$$Nu_t = f\left(Re_t, Pr, Gr, M_\infty, \frac{T_w - T_{adw}}{T_0}\right) \tag{4.9}$$

$$Nu_t = f(Re_t, M_\infty, \tau_w) \tag{4.10}$$

Stainback and Nagabushana (1992) derive equations for mean flow measurements as well as for measurements of small fluctuations:
Stainback and Nagabushana (1992)'s equation for the heat transfer from a heated wire:

$$Q = L\left(k_t + 2\sqrt{\pi k_t c_p \rho u r_w}\right)(T_w - T_{adw}) \tag{4.11}$$

The above in non-dimensional terms:

$$Nu_t = \frac{1}{\pi} + \sqrt{\frac{2}{\pi}}\sqrt{PrRe_t} \tag{4.12}$$

Combining equations equation (4.11) and equation (4.4) yields:

$$P = \left[A'(T_0) + B'(T_0)\sqrt{m}\right](T_w - T_{adw}) \tag{4.13}$$

And generalized for CTA:

$$\frac{E^2}{(R_w - R_{adw})} = A_T(T_0) + B_T(T_0)m^n \tag{4.14}$$

with

$$A_T(T_0) = \frac{R_w A'(T_0)}{\alpha_1 R_{ref}} \tag{4.15}$$

and

$$B_T(T_0) = \frac{R_w B'(T_0)}{\alpha_1 R_{ref}} \tag{4.16}$$

The values for A', B' and n are usually determined through calibration with n ranging from 0.45 to 0.5, roughly $\sqrt{m}$. When given constant density and total temperature, which is a fair assumption in the case at hand, A and B will be constant and the mass flow m can be replaced by the velocity u. King's law hence becomes:

$$E^2 = A + B\sqrt{u} \tag{4.17}$$

or

$$u = A_1 - A_2 E^2 + A_3 E^4 \tag{4.18}$$

In the present work, a fifth order polynomial was used for hot-wire calibration. The coefficient corresponding to the highest order is consistently small, hence effectively rendering the considerations behind equation equation (4.18) valid. For the sake of completeness, the equation concerning small fluctuations:

$$\frac{E^2}{R_w} = L\left(k_t + \sqrt{2\pi k_t c_p \rho u d_w}\right)(T_w - \eta T_0) \tag{4.19}$$

Assuming k_t, c_p, ρ, R_w, T_w and T_0 to be constant yields equation equation (4.20), which, given constant Re_t and Pr is basically a linear relation between fluctuations of mass flow and voltage.

$$\frac{e'}{E} = \frac{1}{4}\frac{\sqrt{2\pi Re_t Pr}}{\left[1 + \sqrt{2\pi Re_t Pr}\right]}\frac{m'}{m} \tag{4.20}$$

4.3.3 Application

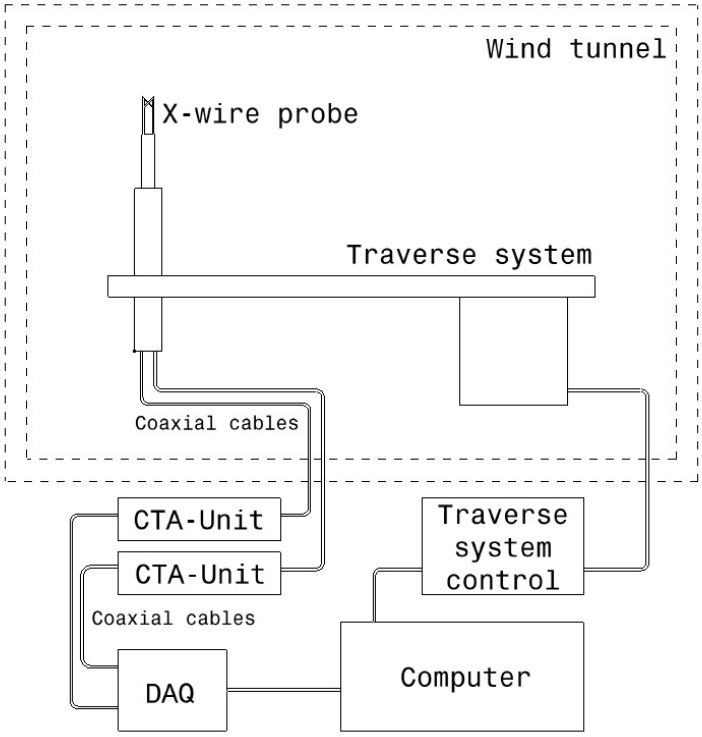

Figure 4.10: Schematic of the testing layout

Initial measurements were carried out using a TSI 1210-T1.5 single-wire anemometer (Figure 4.11(a)) in conjunction with a TSI IFA300 constant temperature anemometer system and the corresponding software ThermoPro. The most important dimensions of the probe are the wire length of 1,27mm and the wire diameter of 3,81μm. Single-wire anemometry yields the velocity magnitude only, however, which is why all tests (except some correlation investigations) were eventually redone using X-wire probes. Here, the addition of a second wire positioned at an angle to the first one, enables the determination of not only the velocity vector's magnitude, but also its direction. The specific probe used, a TSI 1241-T1.5 (Figure 4.11(b)), featured two wires of the same dimension as the TSI 1210's. Due to difficulties arising from using X-wire probes with ThermoPro, the TSI IFA 300 was replaced with simple, but reliable CTA-units (Figure 4.12(a)), the output voltages of which are directly fed into the data acquisition card and subsequently processed with MATLAB. The control panel of such a unit is depicted in figure 4.13.

Note that the internal pre-amplifier was not used as the resulting voltage would have exceeded the limits of the DAQ-card. However, the voltage output range could be adjusted to some extent be altering the overheating resistance (leftmost adjuster on the panel). This was set to a value of 10Ω plus 5 times the combined resistance of cable and hot-wire (roughly 45Ω, see equation 4.21), which yielded a range of about 1.3 Volts for a velocity range of 40m/s. Even though that might seem a little low, the results showed no unintended discretization.

$$R_{OH} = 5(R_{Probe} + R_{Coaxialcable}) + 10\Omega) \tag{4.21}$$

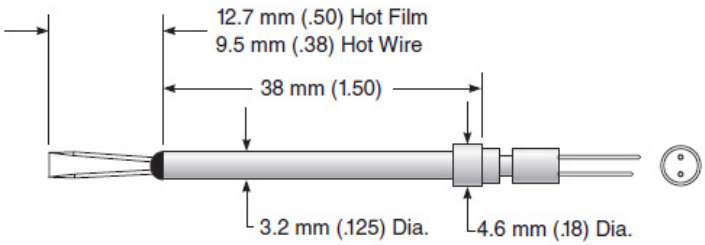

(a) Singlewire HWA (1210)

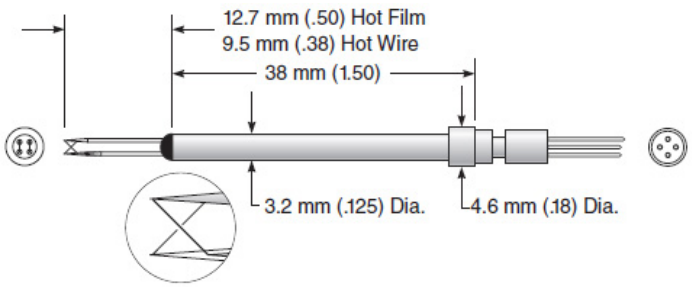

(b) Crosswire HWA (1241)

Figure 4.11: HWA probes

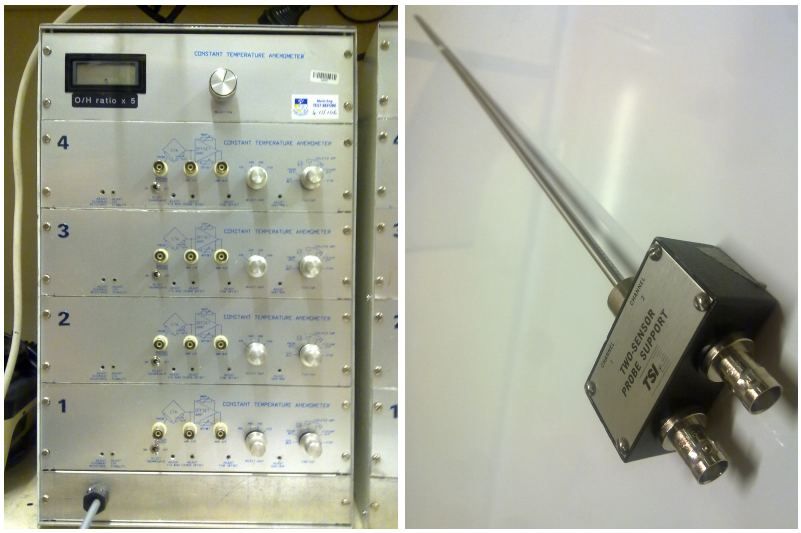

(a) A stack of four CTA-units (b) Probe holder

Figure 4.12: HWA equipment

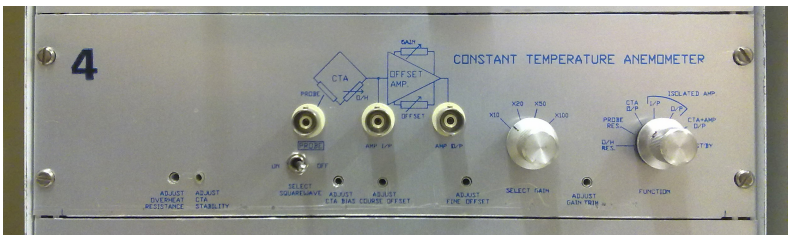

Figure 4.13: Control panel of a CTA-unit

The calibration basically is a two step process. Firstly, offset and gain of the anemometer are set, either in ThermoPro or, as mentioned before, via the OH-resistance. Secondly, the voltages provided to MATLAB must be connected to the corresponding velocities via a calibration function. This function, or more precisely a set of six coefficients defining a fifth order polynomial, is obtained through a 17-point calibration. The probe and its holder are mounted in a calibrator (Figure 4.14(b)) that is connected to the pressurized air network of the lab. The airflow around the probe can be finely adjusted and hence be set to desired values. The pressure changes in the calibrator resulting from the flow are measured using a Baratron differential pressure sensor (Figures 4.15 and 4.14(b)), ambient pressure being the reference, and subsequently transformed to velocity values (see appendix

for the corresponding m-files). Although this is sufficient for a single-wire probe, X-wire anemometry needs a further step, because the dependence of the probe on directional changes of the flow must be determined as well. Of the several possible ways to achieve this, Bradshaw's FEA method (Bakken and Krogstad 2004) was chosen (Figure 4.16). This simple approach gives good results, even though its accuracy is supposed to suffer slightly below 6m/s. At a velocity usually about 70% of the expected centerline speed (here 24.8m/s), the probes are yawed through a number of angles in order to see how the hot-wire responds to directional changes. Then, the respective effective angles α_{eff_i} of the wires at each angle are defined via equation 4.22. In the case at hand, eleven angles are used for the calibration, yielding a set of as many angles per wire. The mean of said set of angles is the desired effective angle. The magnitude of the instantaneous velocity vector and the angle between this vector and the flow direction, β, are subsequently calculated by means of equations 4.23 and 4.24 (See section **??** on page **??** for the application of these equations in MATLAB). Finally, the stream wise and normal flow velocity components are obtained using simple trigonometry. Figure 4.10 shows the general set-up of the respective components, while figure 4.17 depicts a X-wire probe mounted and ready for use.

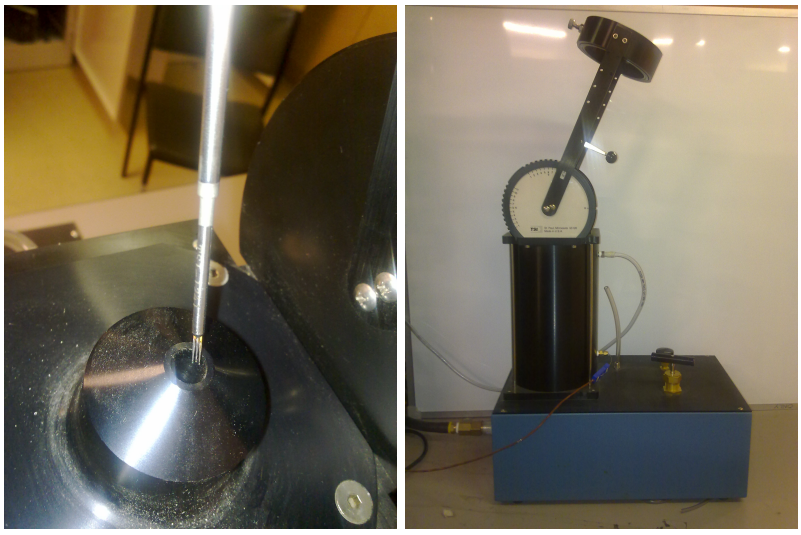

(a) Probe over the air outlet (b) Calibrator

Figure 4.14: The probe in the calibrator during an effective angle calibration.

Figure 4.15: Pressure sensing device (top) with output unit (bottom)

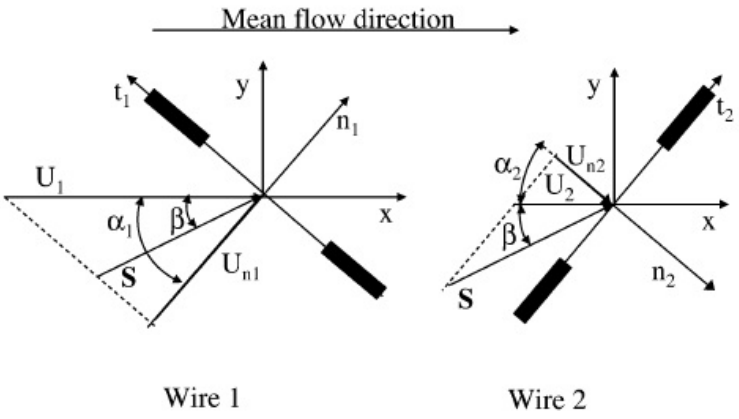

Figure 4.16: Two separated wires of an X-probe. S is the instantaneous velocity vector. U_1 and U_2 are the velocities from the velocity vs. voltage calibrations used to calculate S and β. U_{n1} and U_{n2} are the effective cooling velocities U_{eff_1} and U_{eff_2} respectively. x and y are the stream wise and wall normal directions, and n_i and t_i are the normal and tangential directions in the wire fixed coordinate systems. (**Payne 2001**)

$$U_{yaw_i} \cos(\alpha_{eff_i} + \alpha_{yaw_i}) = U_{unyaw_i} \cos(\alpha_{eff_i}) \tag{4.22}$$

$$S\cos[\alpha_{eff_1}(U_1) - \beta] = U_1\cos[\alpha_{eff_1}(U_1) = U_{n_1}] \tag{4.23}$$

$$S\cos[\alpha_{eff_2}(U_2) - \beta] = U_2\cos[\alpha_{eff_2}(U_2) = U_{n_2}] \tag{4.24}$$

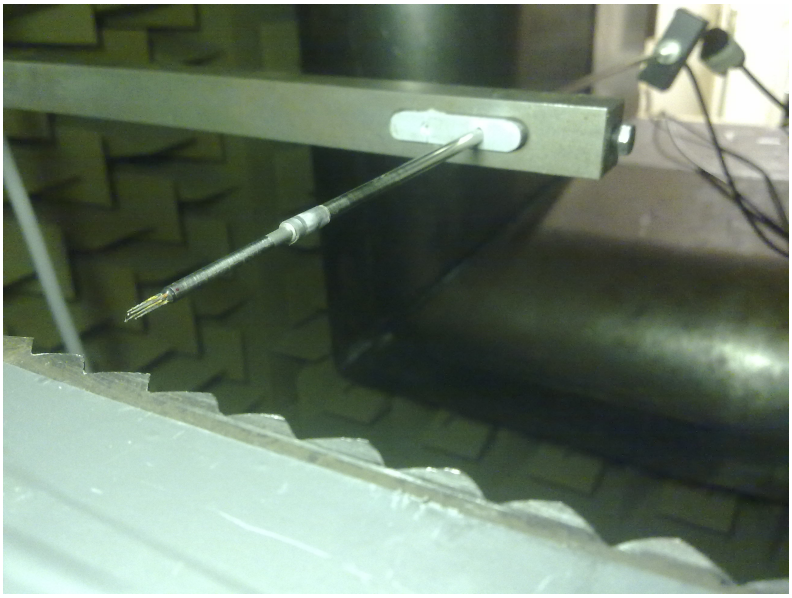

Figure 4.17: X-wire probe during measuring

4.4 Microphones

Figure 4.18: Microphone mounted inside the anechoic chamber

Two B&K type 4190 half-inch microphones (Figure 4.18; see appendix for technical data) were used throughout this investigation. The 4190 is an externally polarized, DC-biased condenser microphone, a type of microphone, which, as the name suggests, employs a capacitor. There are two subgroups, namely DC-biased and high frequency, or radio frequency, microphones. They share the same recording principle, which is based on a plate capacitor consisting of a fixed back plate and a moving plate attached to a diaphragm. The sound waves, i.e. the air pressure waves, move the diaphragm and thereby change the plate distance d, hence transforming the sound information to a function $d(t)$ and, consequently, $C(t)$. The two groups differ in the way they make use of this information, however. In a RF-(radio frequency)-microphone, a low AC-voltage applied to the capacitor is either amplitude-modulated by the changing capacity or, if the capacitor is part of a resonance circuit, frequency modulated. Demodulation yields the sound information in both cases. In DC-biased microphones, the capacitor naturally needs to be charged before changes in the charge can be used as a measuring signal. So-called electret microphones employ stable dielectric media, or electrets, that contain a permanent charge. Nowadays, electrets are commonly made from PTFE, also called Teflon, and attached to the capacitor as films. Such microphones need very little external power, which made them very popular in a number of applications such as mobile phones. Despite this, the majority of laboratory quality microphones is still externally polarized, meaning that a relatively

high supply voltage, typically 200V, is needed to create the difference in potential between the plates. Figure 4.19 shows the basic layout of such a microphone. The polarization voltage U_polar is applied through a high resistance ($R > 10G\Omega$), which yields a constant charge of the capacitor. As mentioned above, the modulation of the plate distance causes a very small AC-voltage that is superimposed on the (DC-)polarization voltage. Below about 140dB, the relationship between sound pressure and voltage is very near linear. The membrane, which is usually made of pure nickel, and the back plate/electrode are about 20μm apart, with the capacity of the setup being around 20pF. Figure 4.20(a) shows a detailed cutaway of typical condenser microphone. Due to the high internal resistance of said setup, a preamplifier (R_in $10 - 100G\Omega$) serving as an impedance converter is necessary. It is not part of the microphone per se, but is usually included in the main tubular case. The lower limit of the usable frequency range (see figure 4.20(b) and appendix for B% 4190 data) is a result of electrical and mechanical effects caused be the polarization resistance (Figure 4.19) and the balance capillary (Figure 4.20(a)), while the upper limit is due to mechanical resonance. In this range equation 4.25 is valid. It linearly relates the measured voltage to the sound pressure acting on the membrane. The sensitivity of a condenser microphone is typically about 50mV/Pa. If the wavelength is sufficiently greater than the membrane diameter, a microphone can be considered direction-independent. Figure 4.20(c) shows that for a half-inch microphone this assumption is valid up to about 2kHz, when bending effects distort the sound pressure. Being a typical condenser microphone, the 4190 needs a polarization voltage, 200V, which is provided by a B& 2829 power supply (Figure 4.21(a)). The 2829 and the microphones are connected via multi-pin LEMO-cables. The output signal from the power supply is preamplified (Gain = 10) before it is recorded by the DAQ, and subsequently MATLAB (Figures 4.21(b) and 4.21(c)).
Calibration employs a BSWA CA 106 sound calibrator (emitting a 1kHz tone at 94dB), which the microphones are slid into (Figure 4.22(b)). The process consists of an initial measurement with the calibrator switched off (self-noise) and a further one with it switched on, thus measuring the calibrator's predefined 1 kHz tone. A MATLAB-algorithm (see appendix) is used to subtract the self-noise and to subsequently compare the measured sound pressure level at the frequency with the highest power spectral density, naturally at around 1kHz, with the known value of 94dB. This yields, firstly, the coefficient that scales the measured voltage to a pressure and, secondly, the offset value accounting for the self-noise.

The anechoic limit of the wind tunnel is 200Hz (CHAPREF) and, as shown in figure 4.20(b), recorded data would require correcting at frequencies above about 10kHz. All sound data was hence band-pass filtered between 200Hz and 10kHz using a forth order digitally simulated butterworth filter.

$$\frac{U_{I=1}}{p} = nS\frac{U_{polar}}{d} \tag{4.25}$$

$U_{I=1}$	Idle input voltage
p	Sound pressure
$U_{I=1}$	Idel input voltage
n	Combined elasticities of membrane and air cushion
S	Membrane area
U_{polar}	Polarization voltage
d	Distance between membrane and backplate

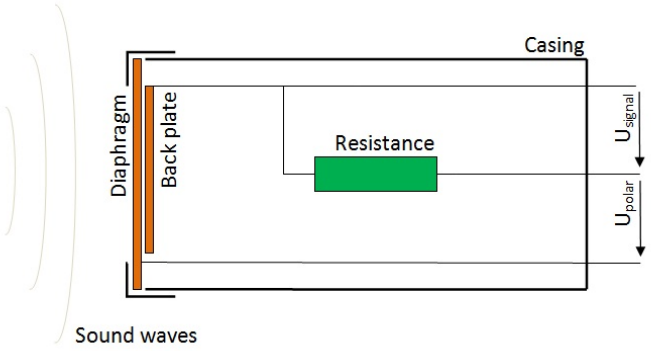

Figure 4.19: Basic design of an externally polarized microphone

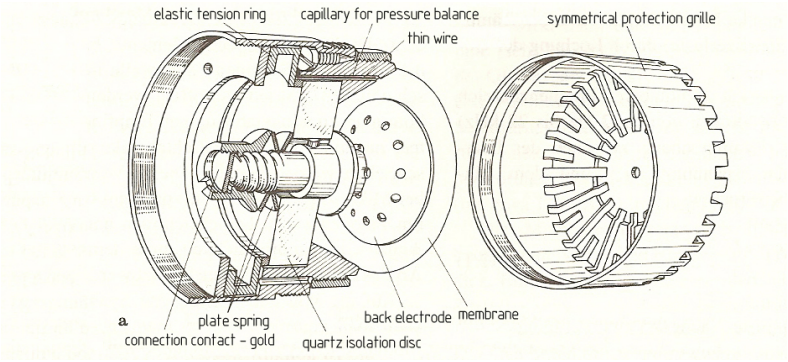

(a) Cutaway

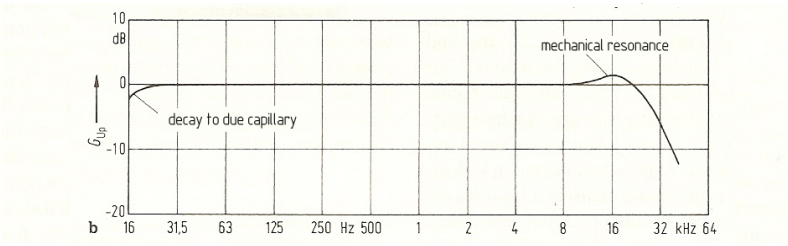

(b) Frequency response

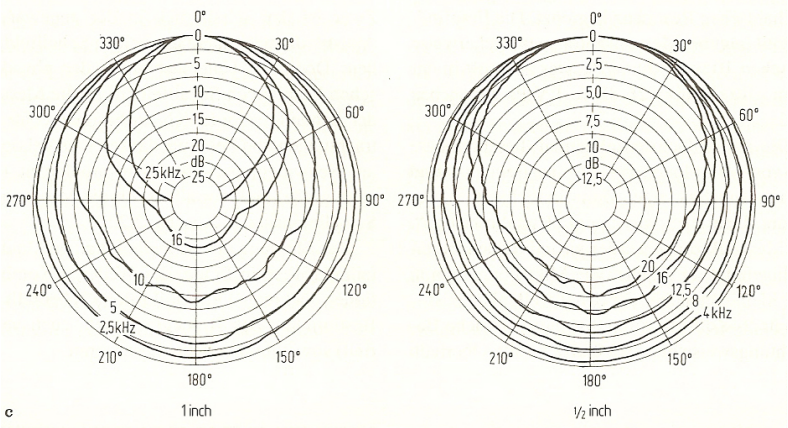

(c) Angular dependency

Figure 4.20: Condenser microphone.

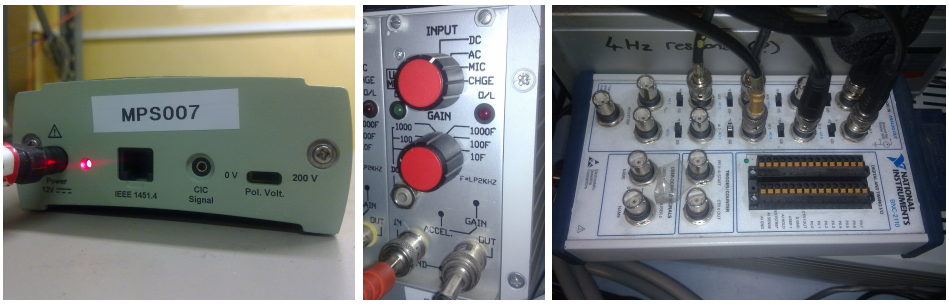

(a) Power supply (b) Amplifier (c) DAQ

Figure 4.21: Peripheral microphone equipment.

(a) Sound calibrator (94dB, 1kHz) (b) Microphone inserted

Figure 4.22: Microphone calibration.

5 Measuring processes

To fully capture the nozzle alterations' influence on the jet and, consequently, on the noise emissions, a number of different tests were conducted. Basically, these tests can be split into three groups, namely the obtaining of velocity data, the recording of sound at various locations and the simultaneous measuring of speed and sound. Detailed descriptions of the respective setups' particulars can be found in the following sections of this chapter, but the commonalities, the most important of which being the jet, are discussed a priori. Initial trial measurements were carried out at a number of different flow velocities (10m/s, 20m/s, 30m/s and 40m/s at the outlet centerline), but limited wind tunnel availability demanded the choice of one flow state at which to obtain all the desired velocity profiles and full flow fields. Considerations about what centerline speed to chose were centered on the question if and how the flow results could be related to the sound measurements of the present work and to previous works by other researchers. Being considerably less time consuming and prone to error, sound measurements could be, and were, done at several different flow states. Preliminary results showed that the sound pressure levels of the lower speed jets do not notably rise above the prevailing ambient noise, meaning that changes in flow due to the nozzle serrations presumably would have been hard to detect in the noise spectra. Furthermore, with the contraction installed, the maximum possible Mach number was about 0.125, which is already a relatively low value. This further speaks in favor of the higher possible flow rates and, eventually, selecting 40m/s, i.e. a Mach number of 0.117, was a straight forward decision. It is not maxing out the fan of the wind tunnel, hence ensuring that the desired flow state can be set at all times, but at the same time provides flow properties that make the results comparable to other works (e.g. REF). The Reynolds number at the outlet depends on what dimension is defined as characteristic. Using the slot width (13.5mm) yields a Reynolds number of 36450, while the equivalent diameter (53.7mm; see section **??** on page **??**) leads to a value of 145000. As indicated before, the setups of the respective tests were loosely

based on earlier experiments done by other researchers, with hopes to be able to check the obtained results against a baseline.

5.1 Velocity field

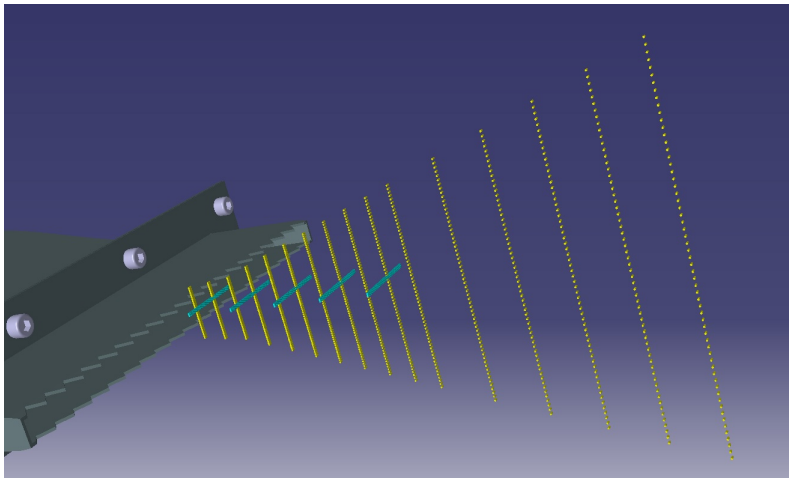

Figure 5.1: Yellow cylinders correspond to the measuring positions of the main vertical flow field, while cyan cylinders belong to the horizontal flow field in the mixing layer

Hot wire anemometry was used to obtain velocity data, a detailed description of which, including calibration procedures etc., can be found in chapter **??** on page **??**. As a trade-off between minimizing vibration of the probe and the support's influence on the jet, the probe holder is clamped by the bracket about 150mm downstream of the measuring location (Figure 4.17 on page 79). This still proved too intrusive for simultaneous noise measurements, however. After initial manual positioning, the measuring points were approached automatically using the traverse system installed in the anechoic chamber. The two series of raw velocity data resulting from a X-wire measurement need to be combined to gain a magnitude S and a direction angle β, through which the actual stream wise and normal velocity components can be computed. Equations 5.1 to 5.4 show how the relations derived in the hot wire chapter are implemented in MATLAB. The main U (stream wise velocity component)-fields (Figure 6.17) for each nozzle configuration consist of 16 individual profiles (named "0", "1", etc, after their distance from the outlet in "slot widths", SW), each itself an array of 61 measurement points. The profiles are symmetrical about the XY-plane, with 30 points above, 30 points below and

one coinciding with this plane. An illustration of the measurement positions is shown in figure 5.1. While the plain nozzle jet was expected to be all-but uniform laterally, the serrations obviously demanded a precise definition of the measurement positions in the Y-direction as well. Thanks to the symmetry of the serrations, three lateral positions on a single serration flank were deemed sufficient to cover the lateral variations in the flow (Figure 6.18). The main flow fields were obtained at the 'side'-position for both serrated nozzles, simply because this position was considered to well represent a laterally averaged flow. In order to account for the opening of the jet, the distance between the respective points was increased as a function of the profiles' stream wise location (see (REF TO APPENDIX) for a table containing the coordinates of all measuring positions). The first profile is located at about 2mm downstream from the outlet. In any case the remaining profiles follow in 13.5mm (1SW) steps for the first ten slot widths and in 2SW steps from then on till 20SW downstream, where the free stream is expected to be fully developed. Thus, each full velocity field comprises 961 (61 times 16) separate velocity values. In addition to these 'global' vertical velocity fields, smaller horizontal fields were gathered in the mixing layer (Figure 5.1), with the probe being moved in Y rather than in Z-direction.

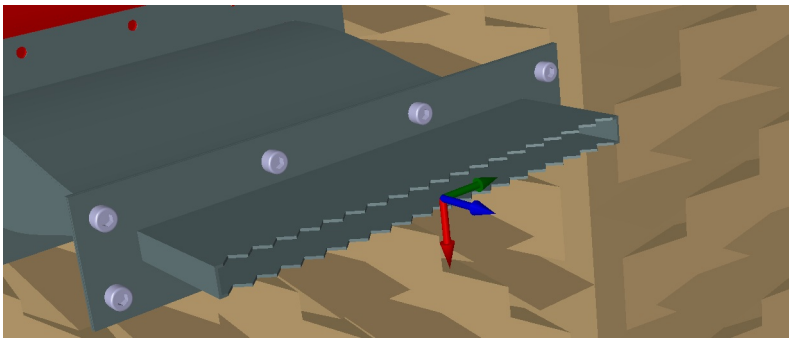

Figure 5.2: The coordinate system used here: X (blue), Y (green) and Z (red). The corresponding velocity components are termed U, V and W, respectively.

Said horizontal flow fields lay in an XY-layer 7.55mm above the centerline, a distance resulting from the geometry of the nozzles. Since each nozzle has an inner height of 13.5mm and is made of 1.6mm sheet metal, the mixing layers are assumed to be located 7.55mm ($13.5/2 + 1.6/2 = 7.55$) above and below the horizontal symmetry plane. Each field consist of five profiles obtained at 1, 3, 5, 7 and 9 slot widths, respectively, downstream (REF TO APPENDIX table again). In order to fully capture the velocity vector components in the mixing layer, each profile was measured twice, once with the probe in the

normal upright position, yielding U and W, and once with the probe tilted 90 degrees (clockwise in stream direction), yielding U and V. On top of the profiles that were used to form flow fields, several further profiles were obtained at various locations, but all of them were used in the end.

$$\beta = \arctan\left(\frac{(\cos(\alpha_{eff_1})\cos(\alpha_{eff_2})\,(U_{1_{raw}} - U_{2_{raw}})}{U_2\cos(\alpha_{eff_2})\sin(\alpha_{eff_1}) + U_1\cos(\alpha_{eff_1})\sin(\alpha_{eff_2})}\right) \tag{5.1}$$

$$S = \frac{U_{1_{raw}}\cos(\alpha_{eff_1})}{\alpha_{eff_1} - \beta} \tag{5.2}$$

$$U = S\cos(\beta) \tag{5.3}$$

$$V = S\sin(\beta) \tag{5.4}$$

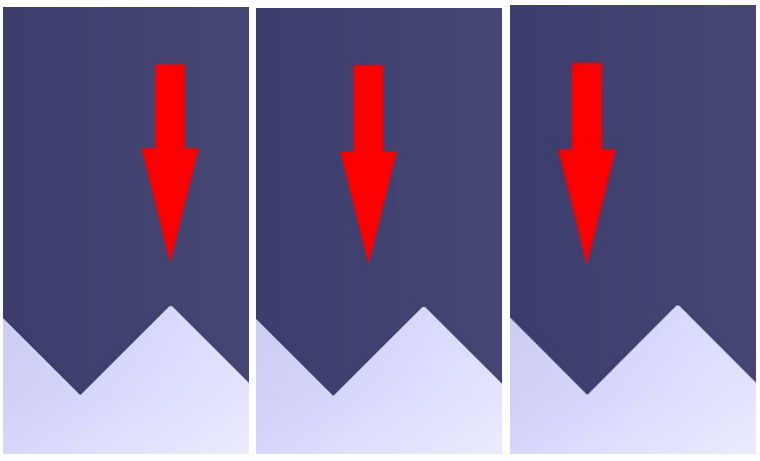

(a) 'top' (b) 'side' (c) 'bottom'

Figure 5.3: Measuring positions in y-direction in case of serrations

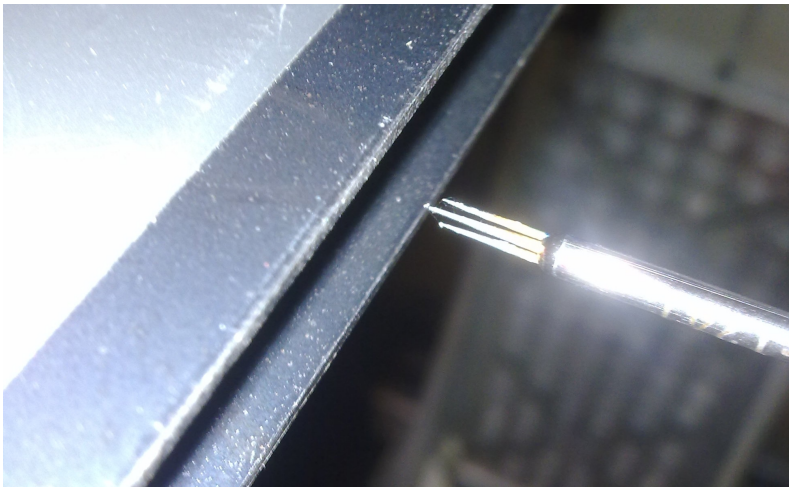

Figure 5.4: Initial position of the hot wire probe

At every measuring position, data was collected for ten seconds at a sampling frequency of 50kHz. For the velocity fields, the resulting 500,000 measurands per position were averaged to yield mean values. Furthermore, each value was normalized using the centerline velocity right after outlet. If a test does not include this vertical '0'-profile, like for example all the mixing layer fields, the wind tunnel calibration velocity, i.e. exactly 40m/s, is used for calibration. The turbulence kinetic energy k, and subsequently the turbulence intensity I, at every measuring position can be derived by calculating the root mean square (RMS) of the velocity fluctuations ($\overline{u}'$,$\overline{v}'$ and $\overline{w}'$). In the mixing layer, all three components are known, and k can thus be computed using equation 5.5. If a component is not known, it has to be estimated, as just leaving it out would yield k-values that are too low. As only U and W were measured when obtaining the vertical flow fields, a guess needs to be made regarding the size of $\overline{v}'$. Commonly, an unknown third component is assumed to be the mean of the other two. This practice leads to equation 5.6. Regardless of how k is derived, equation 5.7 is eventually used to get I.

$$k = \frac{1}{2}(\overline{u}'^2 + \overline{v}'^2 + \overline{w}'^2) \tag{5.5}$$

$$k = \frac{3}{4}(\overline{u}'^2 + \overline{w}'^2) \tag{5.6}$$

$$I = \frac{\sqrt{k}}{U_{ref}} \tag{5.7}$$

5.2 Directivity

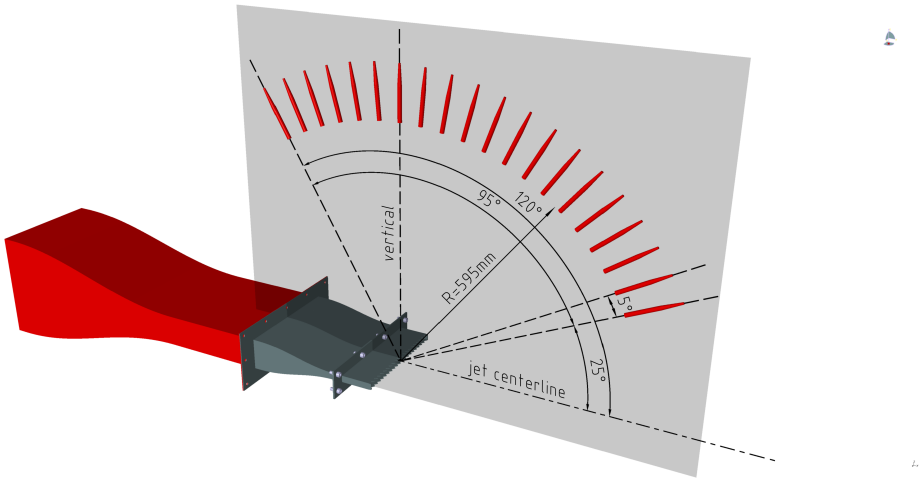

Figure 5.5: The red microphones depict the positions at which sound data was recorded during the directivity investigations.

The rough concept of the directivity measurements was based on (Callender et alREF), mainly because this would yield, to some extend at least, comparison possibilities regarding the angular dependency of the spectra and the SPL. Signal auto- and cross-correlation are of interest as well. The microphones were aimed directly at the nozzle exit and angularly moved along the largest possible circle centered on the nozzle exit (Radius = 595mm; see figure 5.5) from 30deg upstream to 65 deg downstream in 5 deg steps (with the negative Z-axis as reference). This was done for four different velocities (10, 20, 30 and 40m/s; see appendix REF for detailed information about microphone positioning), but note that the step size was increased to 10 deg for the lower speeds as sound emission in these cases is very near nil. It is apparent in figure 5.6(a) that the microphones are ten degrees apart, which at the given radius corresponds to about 100mm. As the traverse cannot perform angular movements and only two B&K 4190 microphones available, manual repositioning was necessary. A wooden template with marks indicating the intended positions of the microphones simplified this task greatly (see figure 5.6(a)). Despite the lack of a sufficient number of microphones to equip a full rack, all desired data (SPL, spectra, auto- and cross-correlation) could be gathered with the available hardware. 30 seconds of sound were recorded at every position and MATLAB automatically paused the process after each individual measurement, so that one could reposition the microphones. All

three nozzle versions were investigated. No simultaneous velocity measurements were carried out. This is true for all sound measurements except for the speed-sound correlation tests.

Figure 5.6: Microphones positioned for the directivity measurements, with (left) and without (right) template.

5.3 Far field

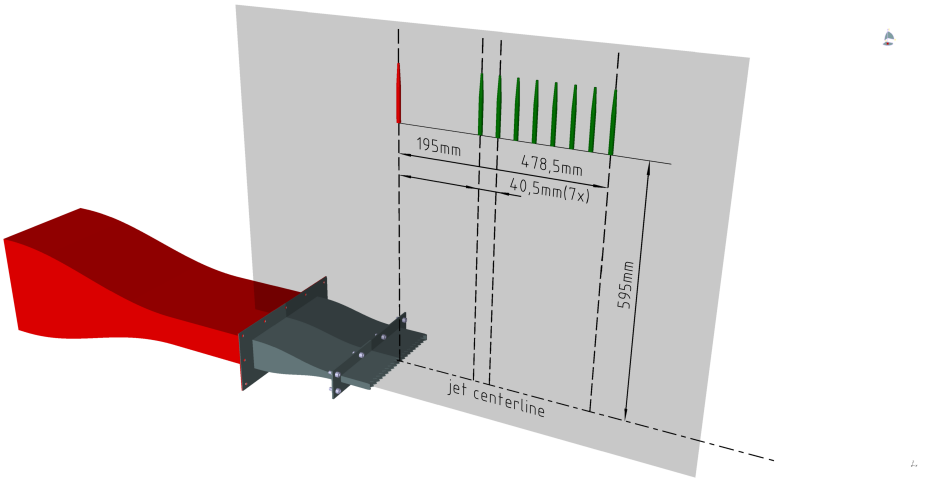

Figure 5.7: The red microphones depicts the stationary microphone, while the green ones correspond to the positions the moving microphone takes up during the course of the test.

In this test, one microphone remained straight above the nozzle outlet (red), while the other (green) was moved to 8 different positions in X-direction, i.e. downstream. The intention of this test was to gain knowledge about the signature of the acoustic far field. Both microphones were installed 595mm above the jet centerline, a dimension resulting from the geometry of the wind tunnel (Figure 5.8). The initial position of the moving microphone was 195mm downstream of the stationary one. This is also somewhat owed to the geometry of the anechoic wind tunnel and the available brackets. The far field is defined as being considerably further than the wavelength of the sound away from the source (see section (helmholtznumber) on page). Strictly speaking, this rule does not apply here, as the the wave length of a 1kHz tone is about 0.34m, which means that, at 595mm above the center line, the far field measurements were taken less than 2λ away from the nozzle outlet. Regardless of this, the second microphone was moved downstream in 7 increments of 3SW (40,5mm) each (Figure 5.7). The measuring was again paused after every recording to allow manual repositioning of the microphone and the setting of different flow velocities (as usual 10, 20, 30 and 40m/s). Fifteen seconds of sound were recorded at every point and the entire procedure was done for all three nozzle configurations (Sample frequency = 50kHz).

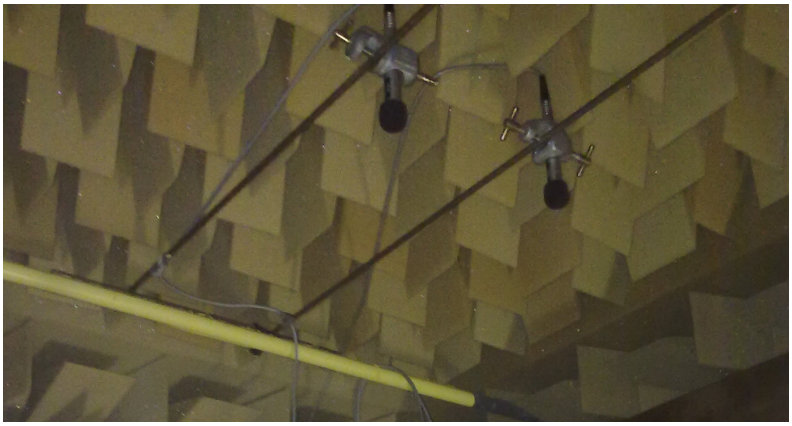

Figure 5.8: Two microphones as they were mounted in the far field tests.

5.4 Near field

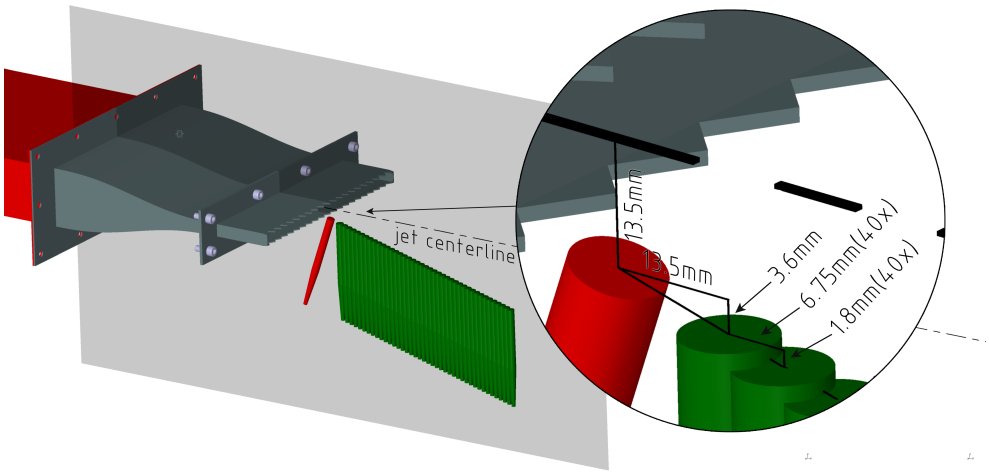

Figure 5.9: As in the far field figure, the red microphones depicts the stationary microphone, while the green ones correspond to the positions the moving microphone takes up during the course of the test.

Similarly to its far field equivalent, the near field test featured one stationary (red) and one moving (green) microphone. There are several differences, however. Firstly, in the near field case the microphones are positioned as close to the opening jet as possible, in order to capture fast-decaying hydrodynamic effects. After assessment of preliminary velocity fields, the opening angle (or half angle, depending on the definition) of the jet was defined as 14,93 degree. This corresponds to a movement in Z-direction of 3,6mm per SW-step in X-direction. Secondly, the use of the traverse system allowed for a higher resolution. The stationary microphone was positioned under the outlet in a way that the microphones midpoint would coincide with the vertical exit plane and be one SW below the jet centerline. Due to the geometry of the brackets this microphone could not be mounted vertically (Figure 5.10), but this should not matter as the microphones are non-directional. The second microphone starts its 'journey' 1 SW downstream of the first and hence 3,6mm below it. As stated earlier, the traverse was used to move the second microphone along a line tilted downwards 15°, more precisely 6,75mm in X-direction and 1,8mm in Z-direction per step; 41 steps in total (Figure 5.9). As in the other acoustic tests, four speeds and three nozzle configurations were investigated.

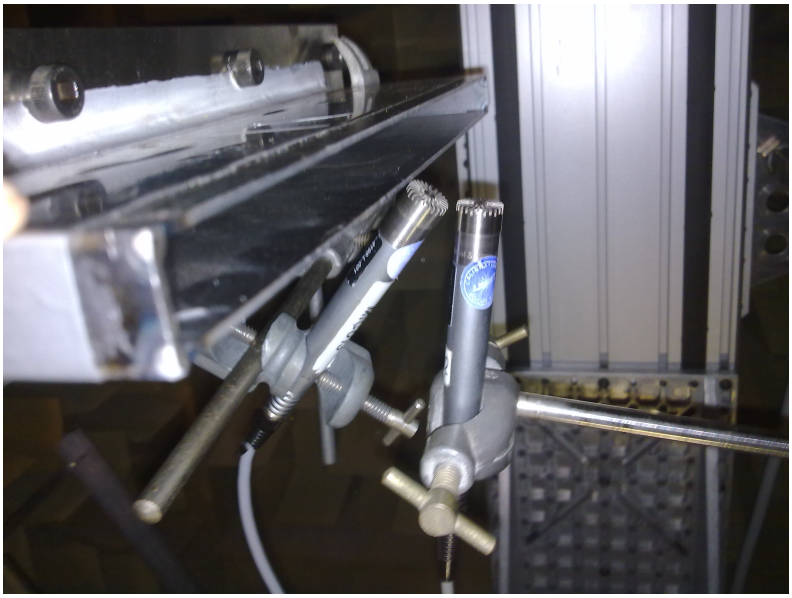

Figure 5.10: Start position of the near field measurements.

5.5 HWA-sound correlation

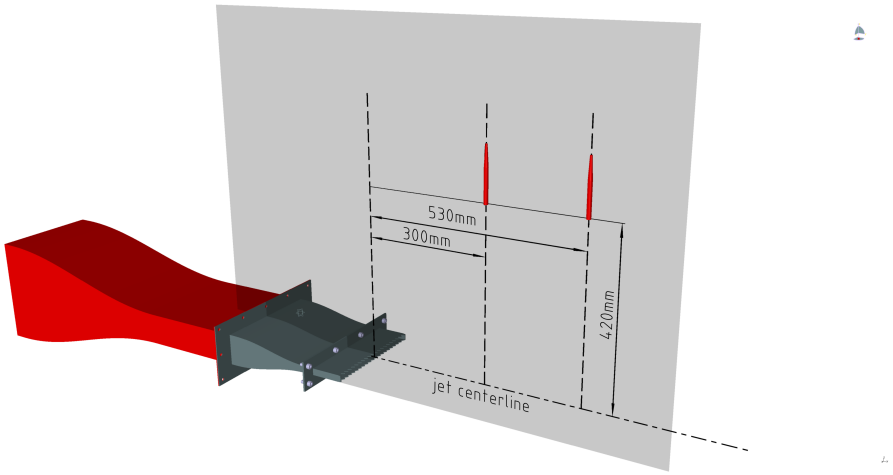

Figure 5.11: Microphone positions (red) and hot wire measuring points (magenta) of the first correlation test setup. In the second setup the rear microphone was not used.

All sound tests were done without simultaneous velocity measurements and vice versa. The reason for this is simply the flow noise generated by the support of the hot wire probe. If one wants to find correlations between the noise and speed signals, they need to be recorded simultaneously, however. The aim of this test was to find a connection between the sound field and the velocity field. The first approach consisted of coherence investigations using inbuilt MATLAB-algorithms. The second, more ambitious, approach was based on conditional averaging. Guj et al. 2003 and others proposed this as a promising means to detect intermittent noise sources. To this end, the microphone data is searched for maxima (see appendix for code REF), which are "cut out" of the signal in the form of 10 ms long samples. This samples are subsequently ensemble averaged and compared to similarly averaged samples from the velocity signal. The velocity samples were taken from the signal at exactly the same times t_i as the sound samples. As an example, if a maximum occurred in the sound signal at, say, 1367.5ms, samples starting at 1362.5ms and ending at 1372.5ms are taken from *both* the microphone and the hot wire data. In the first setup two microphones were mounted in the area that is widely considered to lay in the main emission direction (a line inclined roughly 30deg from the centerline and intersecting the centerline at 5 to 10 slot widths downstream; Figure 5.12(a); Möser et al REF). To move the relatively massive probe holder out of the jet, the hot wire probe was

installed tilted (Figure 5.12(a)). Due to unsatisfactory results, this test was repeated, albeit with a slightly altered setup. As there was little hope to locate the noise source with only two microphones, the objective of this test was changed and the focus was put on finding any connection at all. One microphone was hence enough. In addition to the altered microphone setup, a newly available 'elbow', allowing the probe to be installed in the holder at a 90deg angle, was employed (Figure 5.12(b)). Thanks to this, a X-wire probe could be used, which was moved in 41 steps downstream along the centerline. The first set of tests included the usual four velocities and three nozzle ends, but since the microphones hardly responded to the the lower two and there was very little time for the repeating of these tests, the nozzles were only compared at the highest velocity.

(a) 'First implementation'

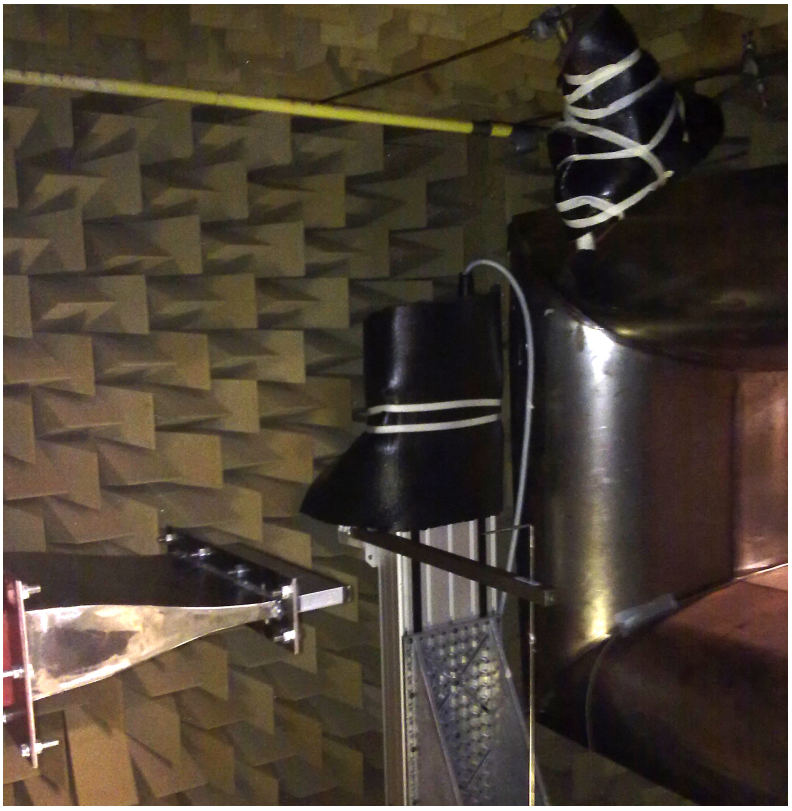

(b) 'Second implementation'

Figure 5.12: The two different setups used in the correlation tests.

5.6 Data processing

This chapter contains all the significant results of the numerous tests and measurements carried out in the course of this work. The raw data samples, of both sound and velocity, are ten to thirty seconds long, which, at a sampling frequency of 50kHz, translates to up to 1.5 million measured values per reading point. Post-processing was hence indispensable and the software MATLAB was employed to this end. A number of different computations was done to extract the desired information from the vast data volume. The sound data, for example, required band-pass filtering (MAYBE MORE DETAIL) before being transformed into spectra or combined to OASPLs. And, as explained in some detail in chapter (CHAPREF TO HOTWIRE), the raw velocity data consists of two separate data strings that need to be converted to U and W (or V, depending on probe orientation). These components were then either averaged in order to build mean velocity fields or used in root mean square calculations for turbulence intensity investigations. On top of that, the velocity values underwent normalization and, if necessary, small corrections. With the aim of finding meaningful connections between flow fluctuations and sound, the in-built coherence and correlation functions were employed to process the simultaneous sound-velocity measurements.
All the MATLAB code used can be found in the appendix (CHAPREF, PAGEREF). The same is true for normalization parameters, limit frequencies for filtering et cetera.

6 Results

6.1 Turbulence determination

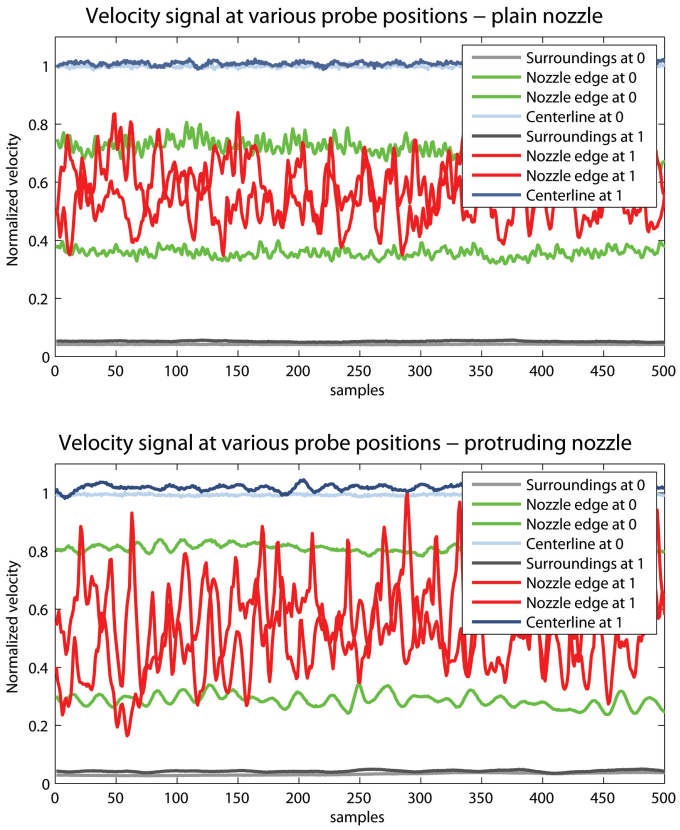

Figure 6.1: 10ms samples taken from the volicity signals.

Figure 6.1 shows what turbulence "looks like" in a velocity signal. Four measuring positions were chosen to illustrate the differences between the distinctive flow domains. "0" corresponds to the position of the first vertical velocity profile right after the outlet, with the "1"-position being situated 1 slot width downstream.
In both sub-figures, the gray lines represent measuring positions completely out of the flow. Unsurprisingly, the velocity there is close to zero and not fluctuating at all. At the jet centerline (light and dark blue), the speed signals are very steady as well, which means that the potential core is laminar at these position. It is an altogether different story at the nozzle edge, however. Due to the importance and the steep vertical velocity gradients in this area, the signals of two measuring points are depicted. For either nozzle, both edge signals show signs of pending turbulence immediately after the outlet (green)

and strong fluctuations, i.e. turbulence, 1 slot width downstream (red). It is noteworthy that the fluctuations are larger in the case of protrusions.

6.2 Acoustic measurements

6.2.1 Directivity

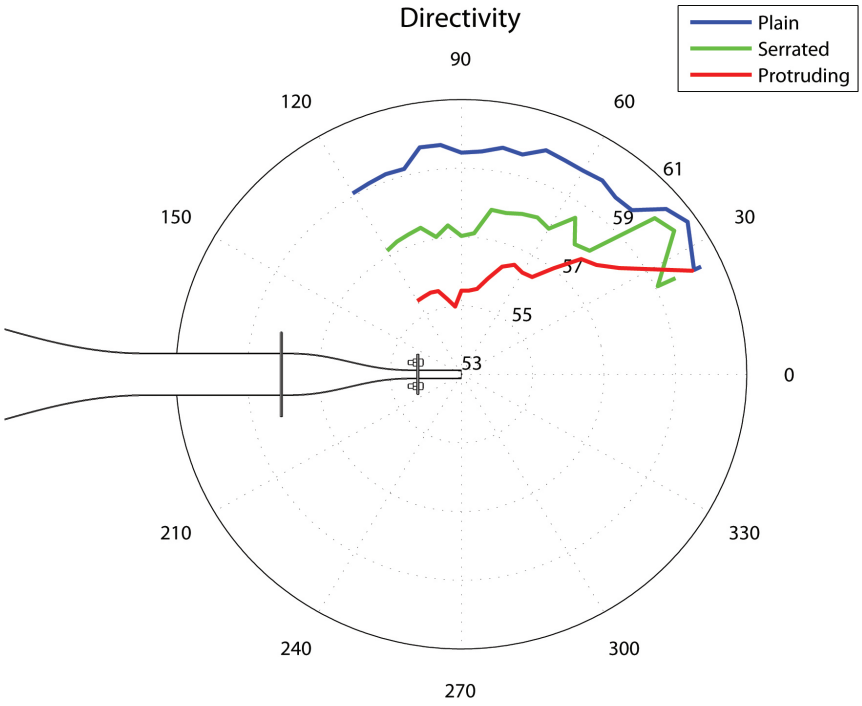

Figure 6.2: Overall sound pressure level as a function of direction (40m/s).

Figure 6.2 shows the overall sound pressure level as a function of angular microphone position. The most important, and obvious, conclusion one can draw from this graph is that the concept of chevrons works. Both nozzle featuring serrations were emitting less noise than the baseline nozzle. This reduction in OASPL is not uniform, as the serrations seem to work very well at fore angles (around 120 degree), but get less and less efficient when going towards the centerline. This does not agree with the results of Callender et al. (2005), who found the serrations to work best at aft angles. They used round nozzles in their work, however, which have a noise emission profile (roughly a point) different from the rectangular nozzle used in this work (closer to a line). Looking at the combined spectra of the baseline configuration (Figure 6.3(a)) reveals that the sound emission is relatively uniform. There is only a small ridge in the 35°-low frequency-area, which probably accounts for the slightly increased OASPL at aft angles. Generally, this uniformity is

not unexpected, as, for example, Möser and Müller (2003) stated that low Mach number jets exhibit little angular dependency.
Both serrated nozzle show qualitatively very similar behavior, albeit with the protrusions handsomely increasing the observed effect. There is very useful reduction in SPL between Strouhal numbers of 0.2 and 1, a range in which Callender et al. (2005) saw reductions as well (Figures 6.3(b) and 6.3(c)). Also the increase at higher frequencies agrees with previous results of other researchers.
The serrations, both straight and protruding, apparently strongly attenuate low frequency noise at angles close to the jet ($\sim 30°$). Apart from said angles close to the jet, the reductions caused by the serrations are very akin over the entire angle range.
The results of the autocorrelation investigations again show that the jet coming form the baseline nozzle is hardly angle dependent. And, also like observed in the spectra fields, straight and protruding nozzle show similar tendencies with the protrusions seemingly increasing the same effect. If and how this is related to the changes due to the nozzle modifications in the spectra fields, is hard to say. Tam et al. (2008) argue that a wider peak in the autocorrelation hints at large coherent structures. HIGH FREQUENCY NOISE ABSORBED BY ATMOSPHERE
Figure 6.5 shows the cross-correlation between a pair of microphones $10°$, or roughly 100mm, apart. Several interesting observations can be made. Firstly, the half-waves of the cross-correlation curves look very similar to their corresponding autocorrelation curves. Assuming that, as Möser and Müller (2003) states, the nozzle exit is a strong, if not the strongest source in low Mach number jets, and keeping in mind that the microphones are directly aimed at the nozzle exit and are positioned at the same radial (and relatively great) distance, it makes sense for autocorrelation and cross-correlation to resemble each other. The measured pressure fluctuations must indeed be very similar. Secondly, there is generally very little lag, but if the microphones are positioned at $90°$, the lag is virtually zero in all configurations (green lines in figure 6.5), hinting yet again at a strong source at the nozzle tip. Thirdly, the cross-correlation at aft angles is comparatively small in the "protrusion"-case, hence somewhat putting the conclusions drawn from the autocorrelation results into perspective.

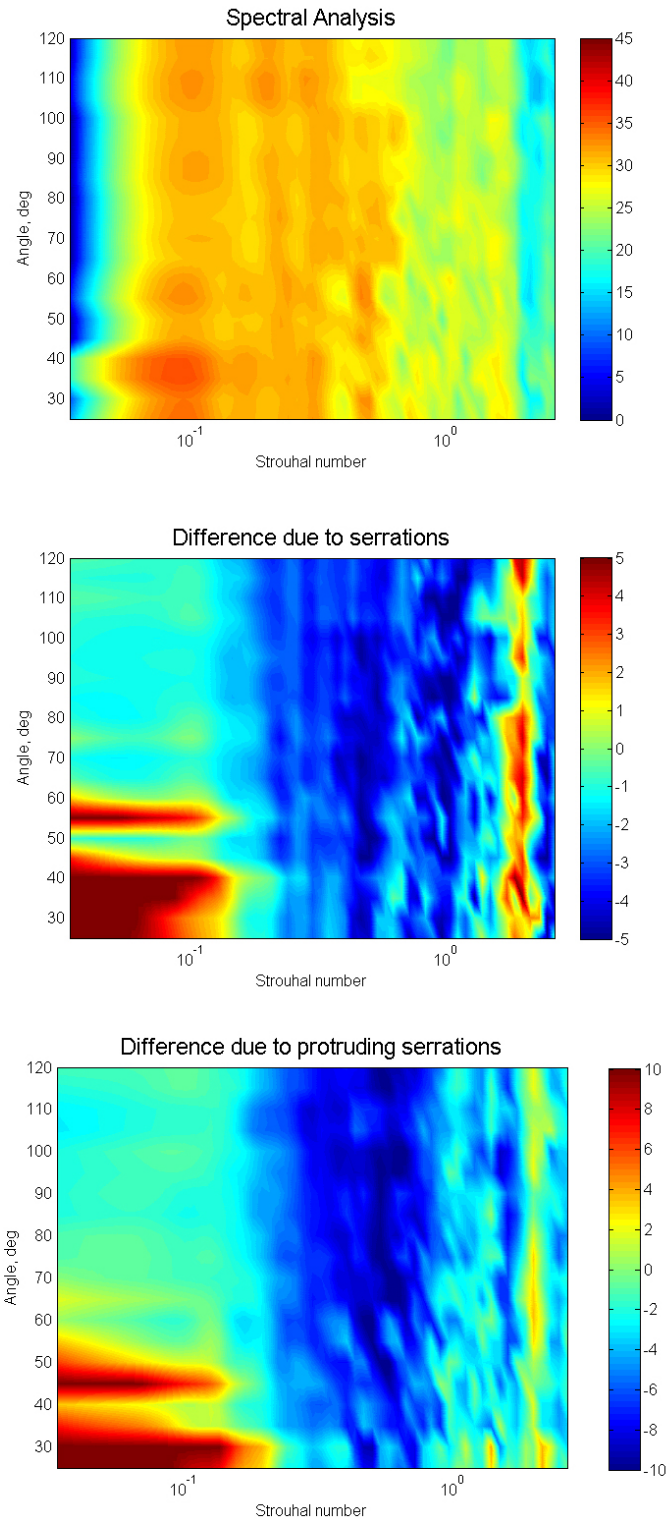

Figure 6.3: Spectra field of the "plain"-configuration and variations due to serrations and protrusions (40m/s).

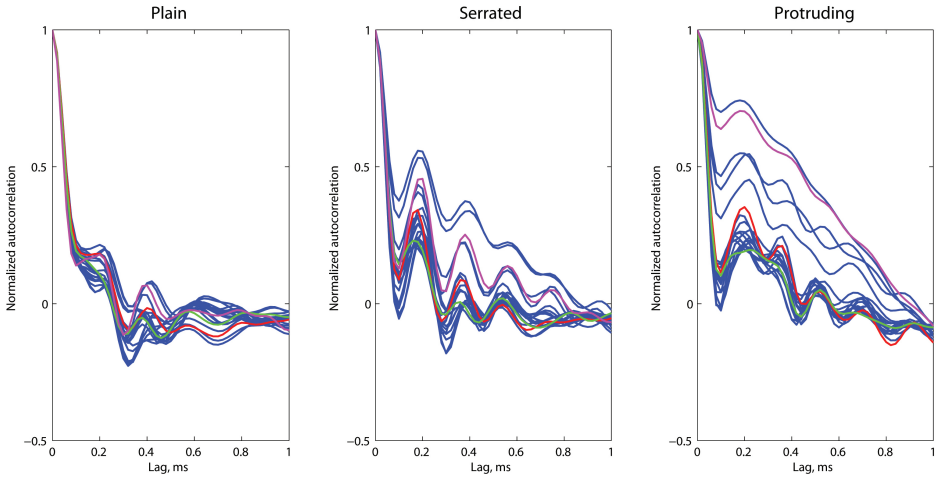

Figure 6.4: Autocorrelation plots for all three configurations at 40m/s. Note that to highlight interesting angles, the red line in every figure corresponds to "120°", the green line to "90°" and the magenta line to "25°".

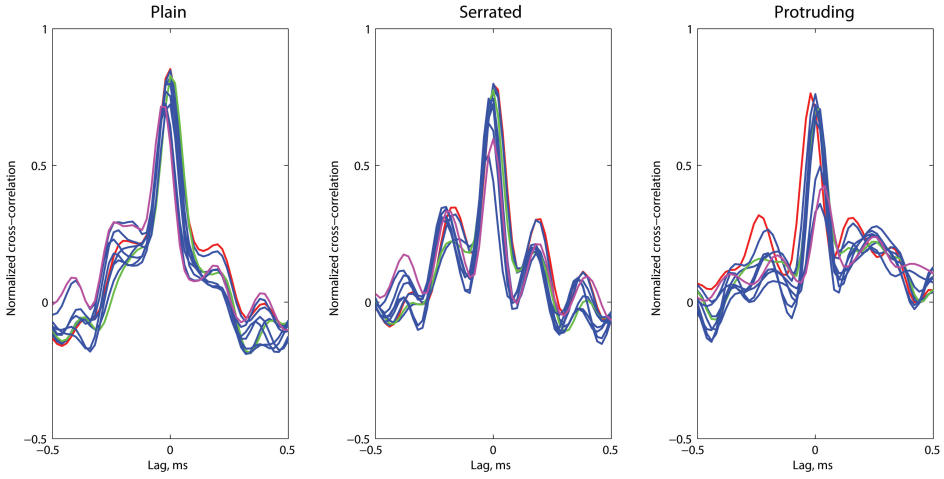

Figure 6.5: Cross-correlation plots for all three configurations at 40m/s. Again, note that the red line in every figure corresponds to "120°", the green line to "90°" and the magenta line to "25°".

6.2.2 Near field

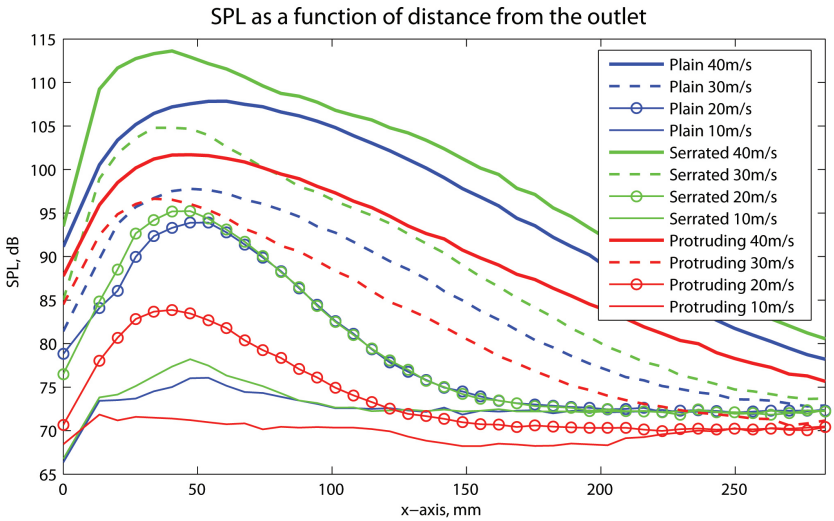

Figure 6.6: Overall sound pressure level of all test configurations.

Figure 6.6 shows the combined OASPL functions resulting from the near field tests. It is remarkable how the protrusions seem to reduce the SPL at all velocities. In the region close to the jet the microphone measurements are understood to be a combination of hydrodynamic and acoustic pressure fluctuations. Tinney and Jordan (2008) have discussed this in some detail.
As the hydrodynamic fluctuations are assumed to play an important role in the near field, these curves can be interpreted as being at least partially related to the turbulence intensity in the respective areas. Keeping this in mind, the plot shows very good agreement with the turbulence intensity results stemming from the hot wire tests (Figure 6.26 on page 130). Both measuring methods reveal that the nozzle featuring straight serrations seems to yield the most turbulent jet and that protrusions make the jet slimmer, i.e keep it further away from the microphone path, and move the turbulent 'core' slightly upstream. Apart from its magnitude, the graph corresponding to the serrated nozzle does not resemble the hot wire results well. But then again, the microphone data contains information about the acoustic field as well, hence complete agreement of turbulence intensity and near field pressure would be unlikely anyways. The 70dB base line noise that remains virtually constant for the lowest velocity over the entire investigated length is presumably due to hydrodynamic fluctuations, as acoustic fluctuations would most likely reach the far field. At 10m/s no flow noise is detected in

the far-field, however.
Tinney and Jordan (2008) proposed that the boundary between the hydrodynamic and acoustic regimes depended on frequency as well as on wave number ($f < k_x a_a$, see chapter **??** on page 47), meaning that a frequency spectrum alone is not enough to draw the line. But one might still assume that the probability to remain in the hydrodynamic domain is higher at low frequencies and such *ad-hoc* separations of the spectra in a low-frequency hydrodynamic field and a high-frequency acoustic regime have been suggested by Arndt et al. (1997), Harper-Bourne (2004), Coiffet et al. (and 2006). Tinney and Jordan (2008) argue that the coherence is a useful measure to approximately separate the regimes, as such plots clearly show the difference between the coherent structures of the flow and the chaotic sound field. Coherence plots in the form of contours for all three configurations can be found in figure 6.12. The devision into the domains, is immediately apparent, even if the resulting magnitudes (very low with serrations, very high with protrusions) do not agree with the calculated cross-correlation (Figures 6.9(a) and 6.10; note that for both coherence and correlation, the signals of a fixed microphone and an intermittently moved microphone are compared). Regardless of the magnitude, the change in regime seems to take place at a Strouhal number of about 0.6. This roughly agrees with Tinney and Jordan (2008)'s initial results (Figure 3.2(b)). The approximated change from fluid domain to acoustic domain seems to occur at roughly the same Strouhal number for all configurations. Figure 6.7 shows the spectra obtained at the near most position to the nozzle. $St = 0.6$ falls into the area where the low frequency "hill" merges into a flatter high frequency range. The various peaks above $St = 1$ can be seen in figures 6.8 and fig:chnf as well and they seem to be dependent on the nozzle geometry in so far as the protrusions apparently push them to higher frequencies. These frequencies may be an inherent frequency of the nozzles, comparable to those of organ pipes.

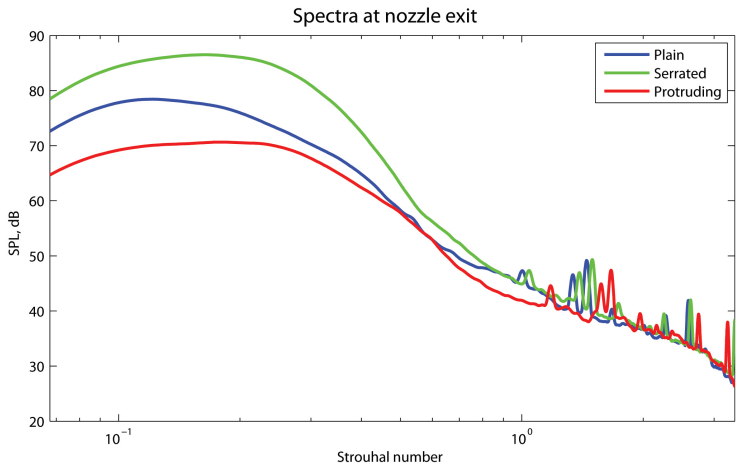

Figure 6.7: Comparison of the spectra one SW downstream of the outlet.

Figure 6.9 shows near field cross-correlation plots for all configurations. The auto correlation of the stationary microphone positioned right under the edge of the outlet is depicted in figure 6.9(a). At zero lag, the normalized correlation value, expectedly, amounts to 1. At its initial position, the moving microphone sits one slot width downstream and 3.6mm below its stationary counterpart. The normalized cross-correlation functions at this position are displayed in figure 6.9(b). According to the plot, the signal of the moving microphone trails the signal of the first by 25 samples, which, at 50kHz, translates to 0.5ms. When multiplied with the mean flow speed at the exit (40m/s), one finds that the air within the jet travels 20mm during this time. This calculated distance is very close to the gap between the microphones, which amounts to slightly more than 13.5mm. Taking into account the fact that the flow speed at the edge of the jet is somewhat lower than at the core, however, the derived length of 20mm seems to be reasonably near the distance the air would actually have traveled at 40m/s. Due to fact that obviously the flow speed rather than the speed of sound is 'characteristic', it can be concluded that aerodynamic pressure variations are dominant in this region very close to the mixing layer, supporting previously made assumptions. These considerations also work when applied to the signals recorded at 3 (6.9(c)) or 5SWs (6.9(d)) downstream. Combining the maxima of all cross correlation plots yields figure 6.10.
While the lag sheds light on the time delay between the two signals at hand, the normalized correlation value basically tells how similar they look. It is obvious from figure 6.10 that the resemblance between two signals decreases greatly with increasing distance between the microphones. It is noteworthy

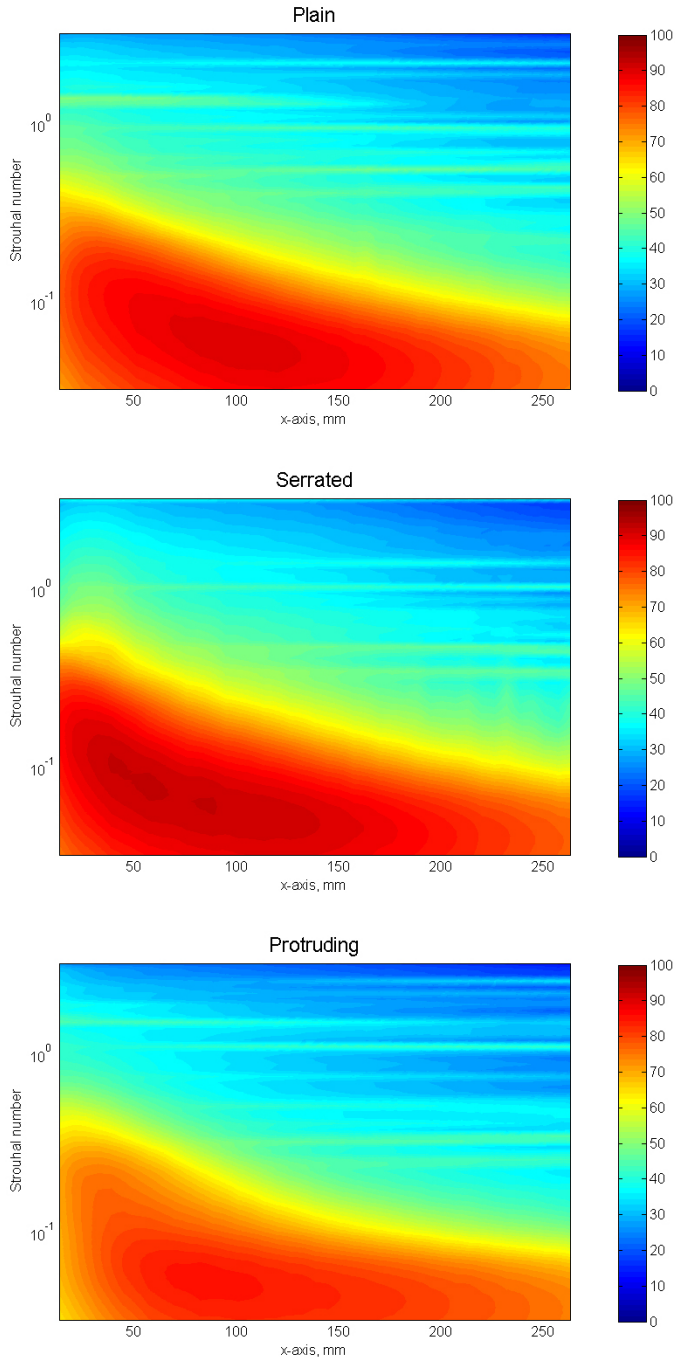

Figure 6.8: Resulting turbulence intensity when taking into account all three components u′, v′ (estimated) and w′.

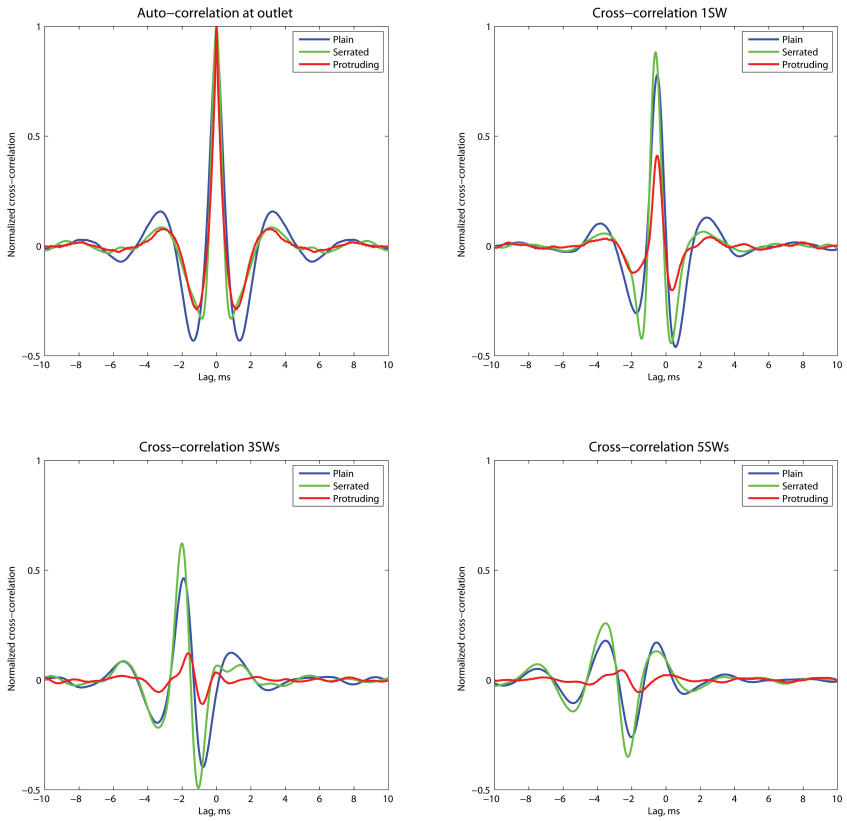

Figure 6.9: Autocorrelation and cross-correlation plots for all configurations

how much less correlation there is in the case of protruding serrations. As the near field microphone measurements seem to be related closer to aerodynamics than to acoustics, this hints at an earlier onset of turbulence in the mixing layer due to the protrusions. This assumption is supported by the turbulence intensity measurements (Figure 6.26(c)) on page 130). The humps in the 'plain' and 'serrated' curves could probably be explained with the jets' being much wider at these locations (100mm or 7SWs to 200mm or 14SWs downstream) than the 'protruding' jet (Figure 6.26 on page 130).

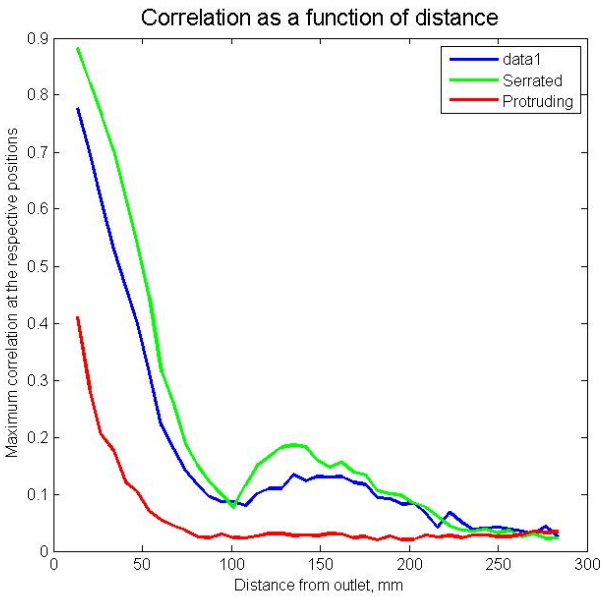

Figure 6.10: Comparison of graphs consisting of the maxima of the respective correlation spectra at each position

The conclusions drawn from the above, namely that the near field microphone recordings predominantly contain information about aerodynamic fluctuations, are further validated by the phase shift data, at least for low frequencies (Figure 6.11). The blue curve reaches a shift of 180° at a Strouhal number of about 0.09, which translates to 240Hz. At this frequency half a wave length, i.e. 180 degree, takes 1/480s, which is equal to the time it takes the wave to cover the distance between the two microphones. 3SWs amount to 40.5mm and dividing this by 1/480s yields an average convection speed of 19.44m/s, a reasonable value for this relatively short distance close to the outlet. Calculating the convection speed using other frequency/phase shift-couples from the same plot, for example 50 degree at a $St = 0.015$, leads to the same result ($\sim 20m/s$). The average wave progression speed decreases quickly with increasing distance from the outlet, since the microphone is moved along the edge of the opening jet where flow speed is generally lower and decaying faster than in the center. Note that the phase shift function of the protruding nozzle is less smooth than the other two, which are virtually identical to each other. This fits in with the hot wire results, where the strong influence the protrusions have on the distributions of velocity and turbulence is clearly visible (see figures 6.26 on page 130, among others).

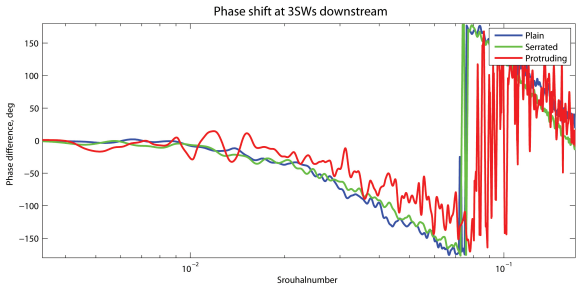

Figure 6.11: Phase shift between moving and stationary microphone as a function of frequency.

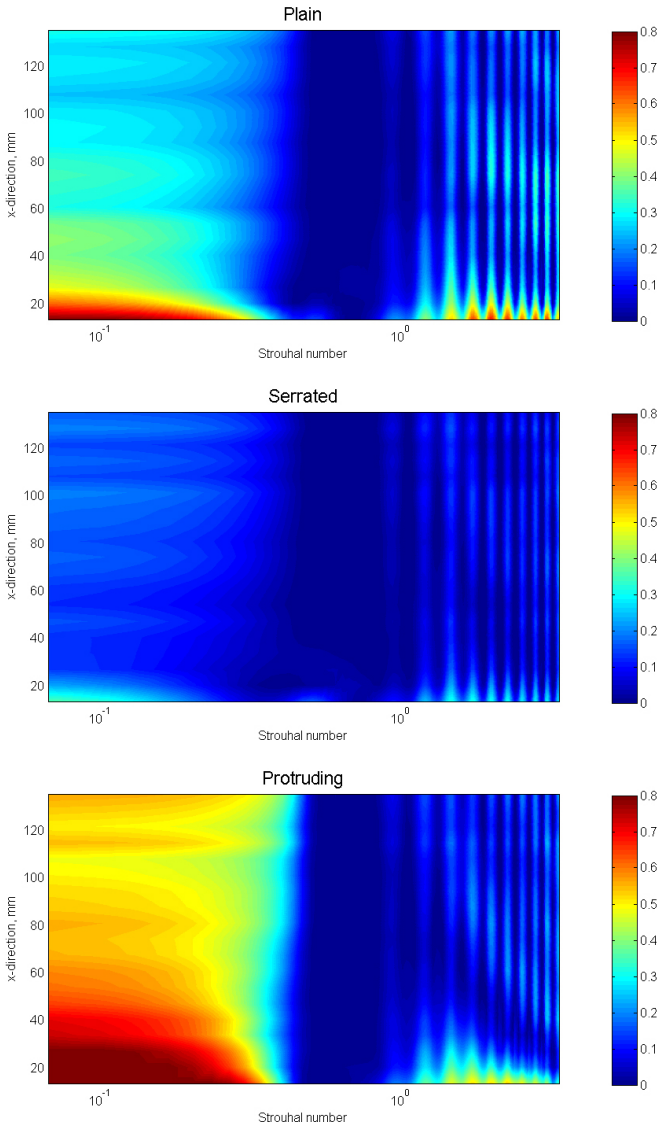

Figure 6.12: Coherence between the signals of the stationary microphone and the moving microphone at 41 different positions.

6.2.3 Far field

The far field measurements were carried out at four different velocities (see section **??** on page **??** for details). Figure 6.13 shows all OASPL graphs combined. As usual, blue, green and red correspond to the plain, serrated and protruding nozzles, respectively. Here, the line widths are a measure for the exhaust velocity, ranging from 10m/s (thinnest) to 40m/s (thickest). At lower speeds, the jets' noise emissions are not high enough to notably rise above the prevailing background noise, hence the significance of the 10m/s and 20m/s curves is limited. At higher speeds, however, the influence of the nozzle geometry on the noise becomes clearer. Straight above the outlet, the noise reduction due to the protrusions amounts to about 4dB. The measuring position "0mm" here is the same as "90deg" in the directivity tests (Figure **??**) and, consequently, the OASPL plots show very similar values at these positions. But as the microphones are moved closer to the jet in the directivity investigations, the noise reduction diminishes and at about 30 degrees from the centerline the measured noise levels from all three nozzles become about equal. In the far field, however, the relative noise reductions remain relatively constant over the entire range. The spectra fields resulting from the far field measurements are, again somewhat expectedly, very close to their directivity counterparts. In both cases, the plain nozzle yields homogeneous fields, which do not depend strongly on the X-position (Figure 6.14(a)). Figures 6.14(b) and 6.14(c) show how the serrated nozzles change the fields. Qualitatively, the effects of the two nozzles are very similar, albeit with the impact of the protrusions being significantly higher magnitude wise. The nozzles seem to be most effective at $0.3 < St < 1$, again very similar to the directivity results. In this range, the reductions can reach 5dB with straight serrations and almost 10dB with protrusions! At aft positions, the modifications generate low frequency noise, however. This effect has been seen in the directivity results as well, but in the far field case the increase in SPL at low frequencies is not sufficiently high to offset the reductions in the mid-range.

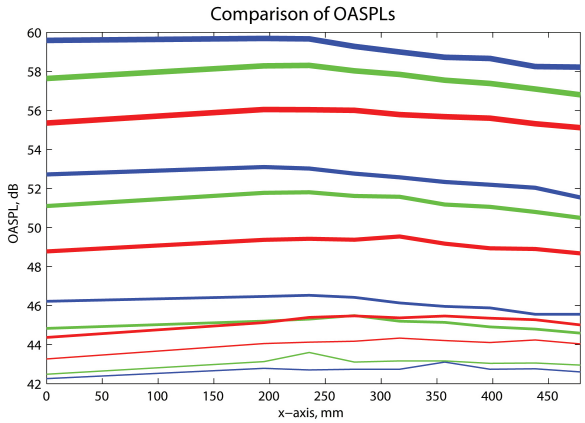

Figure 6.13: Overall sound pressure level of all twelve investigated configurations. Blue, green and red correspond to the plain, serrated and protruding nozzles, respectively. The line widths are a measure for the exhaust velocity, ranging from 10m/s (thinnest) to 40m/s (thickest).

In figure 6.15, the autocorrelation of the stationary microphone (red) is plotted eight times, simply because the measurements were available from the cross-correlation investigation. At the very least, they show the pleasant repeatability of the microphone measurements. This is further supported by the fact that the red plots in figure 6.15 very closely resemble the green plots in figure 6.4 an page 107, which is hardly a coincident as the plots correspond to exactly the same microphone position.
In the far-field investigations, the autocorrelation does not seem to depend very strongly on the position of the microphone, but the different nozzles seem to lead to three distinct basic shapes of the curves. Unsurprisingly, this is also true for the autocorrelation results of the directivity measurements (figure 6.4 an page 107).
The basic shapes of the cross-correlation plots in figure 6.16 somewhat resemble their respective autocorrelation counterparts, an observation already made when dealing with the directivity results. Apart from that, it is very apparent in the figures how an increased distance between the microphones leads to increased lag. Furthermore, the reduction in cross-correlation observed in figure 6.5 an page 107 is present here as well. Unfortunately, the cross-correlation plots also reveal a mistake made when selecting the microphone positions for the far-field tests. All the positions are downstream and, moreover, relatively far away from the nozzle in X-direction. That the different microphone positions are recovered so nicely in the cross-correlation plots, strongly indicates that an opportunity was missed to gain some information

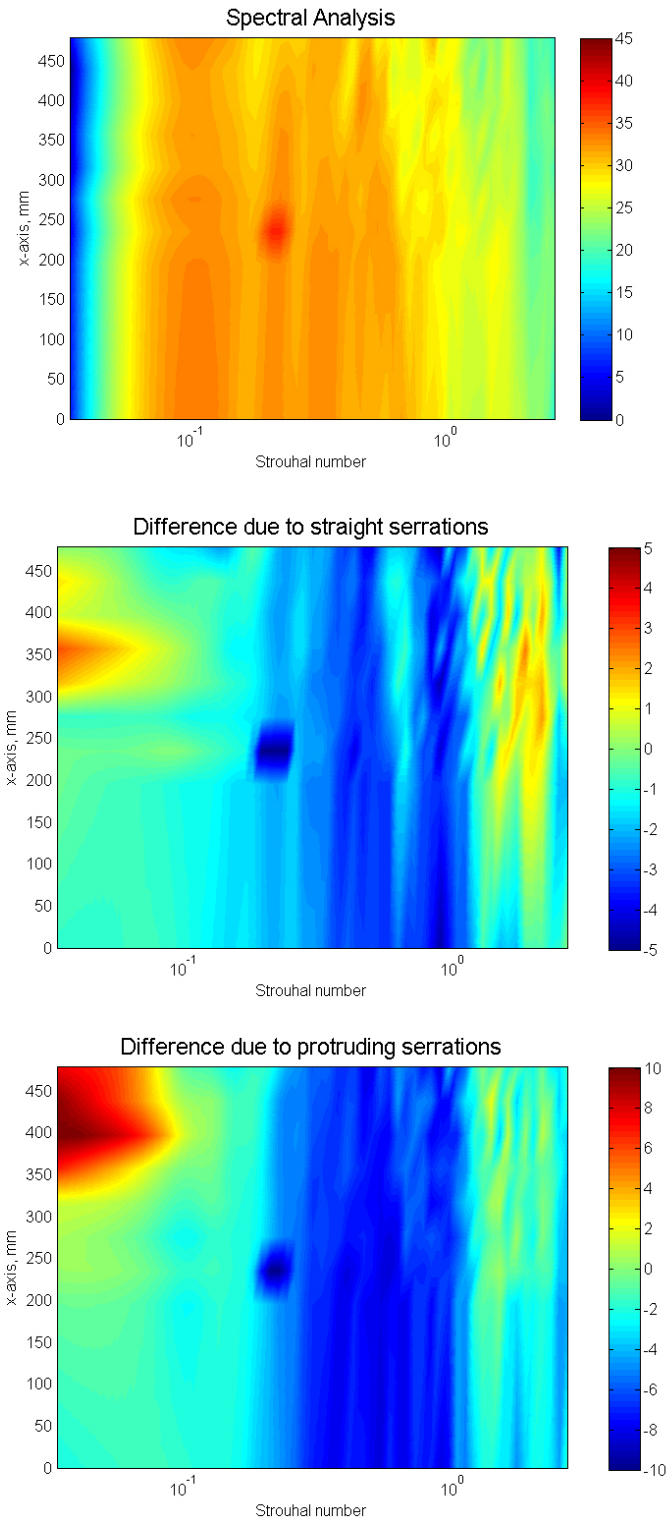

Figure 6.14: Spectra field of the "plain"-configuration and variations due to serrations and protrusions.

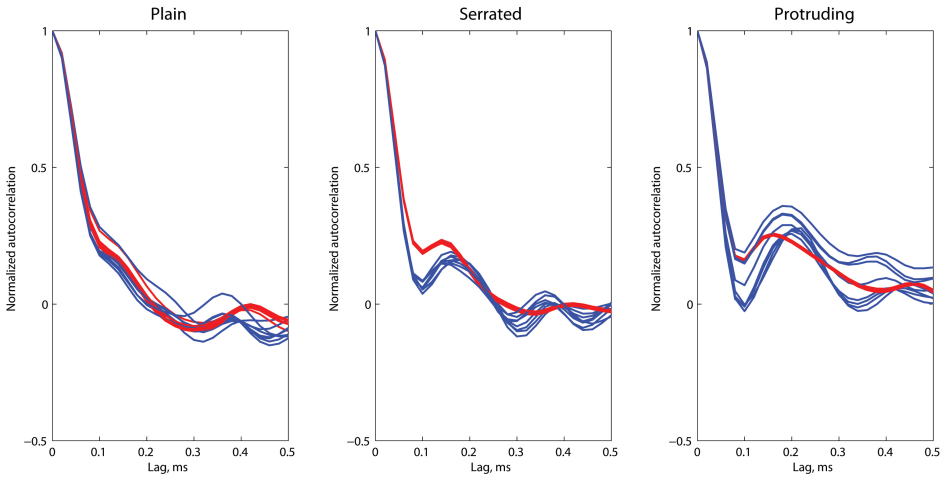

Figure 6.15: Autocorrelation plots for all three configurations at 40m/s. The red lines in every figure correspond to the autocorrelation of the stationary microphone straight above the nozzle exit (90°). The magenta line corresponds to the last position of the moving microphone at ∼480mm downstream.

about the noise source. Extending the range of the moving microphone further upstream, at least some distance beyond the coordinate origin at the nozzle tip would most likely have been sufficient.

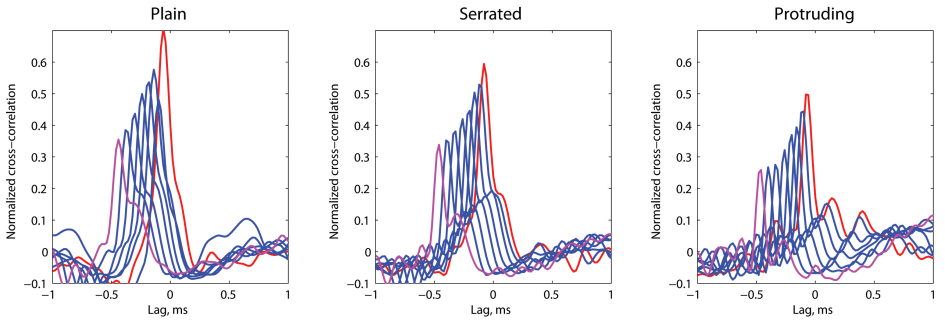

Figure 6.16: Cross-correlation plots for all three configurations at 40m/s. in these figures, the red lines correspond to the first position of the moving microphone (195mm) and the magenta line to its last position (∼480mm).

6.3 Flow measurements

The hot wire measurements were carried out in an attempt to, firstly, capture the various velocity fields and, secondly, to unveil differences in the flow due to the nozzle modifications. A detailed description of the employed method, including all measuring positions, can be found in section **??** on page **??** and in the appendix (REF), but for the sake of simplicity, figures **??** nd **??** are included in this section as well.

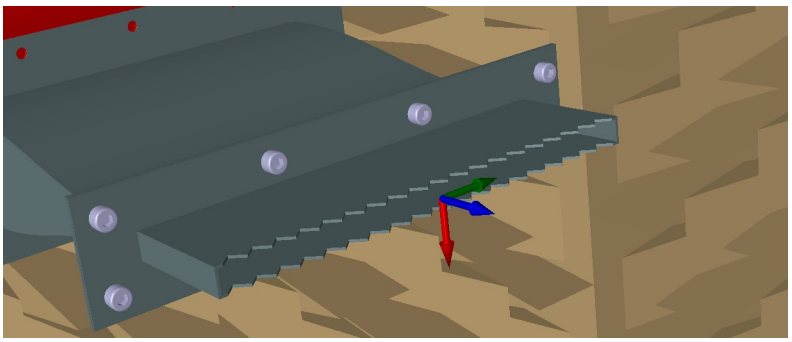

Figure 6.17: The coordinate system used here: X (blue), Y (green) and Z (red)

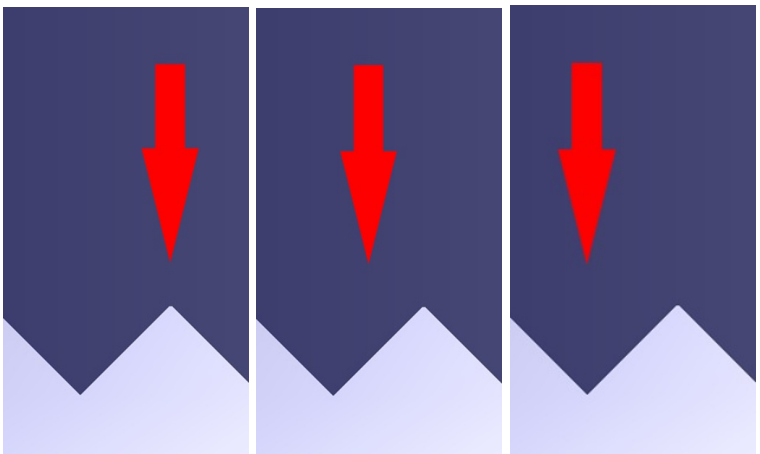

(a) 'top' (b) 'side' (c) 'bottom'

Figure 6.18: Measuring positions in y-direction in case of serrations. Note the the light grey (default CATIA color) portions represent the nozzle.

6.3.1 Velocity fields

Full velocity fields, subsequently compared to the plain nozzle results, were only obtained at the 'side' position (Figure 6.18(b)). For the sake of comparability, these U,W-fields were normalized using the respective centerline velocities immediately after the outlet. The results, depicted in the form of contours, are shown in figure 6.19. Figures 6.19(a) and 6.19(b) are very similar, albeit not identical. Further considerations regarding this similarity are made a bit later, when the centerline velocity decay is discussed. The field corresponding to the jet due to the protruding nozzle (Figure 6.19(c)) clearly differs from the reference, however. Firstly, the plume is much smaller and shorter and, secondly, there seems to be a constriction at about 65mm downstream. One may interpret this as 'focusing' of the jet by the protrusions. The centerline velocity decay is shown in figure 6.20. According to the plot, the speed slightly increases after the outlet in the plain and protruding configurations, while it immediately starts to decrease in the case of straight serrations. An increase in centerline velocity after the outlet of rectangular nozzles was also observed by (NASA PAPER REF), for plain as well as for serrated nozzles. Assuming now that the slight increase or decrease in velocity between the outlet and the location where substantial decay starts were negligible, i.e. using the 'decay start' velocity rather than the centerline velocity at the outlet as normalization parameter, would result in the serrated-function to be shifted up in the plot. Now virtually identical between 50 and 130mm downstream, the functions corresponding to the plain and serrated cases, respectively, do not suggest notable changes in the flow field due to straight serrations. This is further confirmed by the vertical velocity profiles obtained at 'top' and 'bottom' (Figure 6.21(a)), also hinting at a largely uninterrupted flow field. Applying the same change in normalization on the velocity contour of the serrated-configuration would presumably put it even closer in appearance to the plain-configuration. Figure 6.21(b), on the other hand, shows how strongly the protrusions influence the jet, which is in accordance with figure 6.19(c).

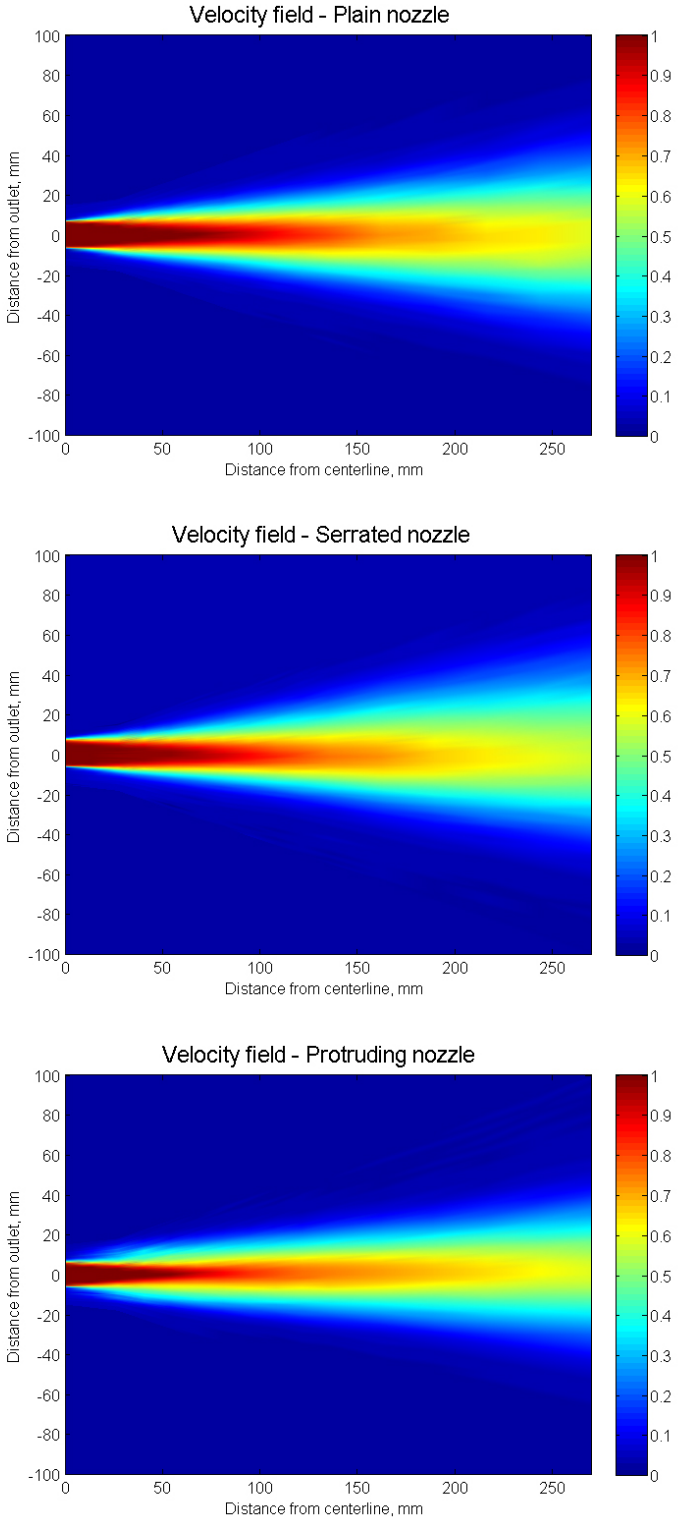

Figure 6.19: Velocity fields

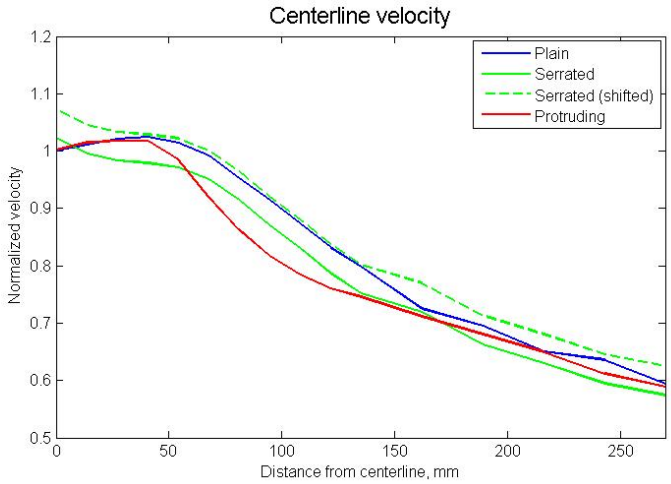

Figure 6.20: Centerline velocity decay

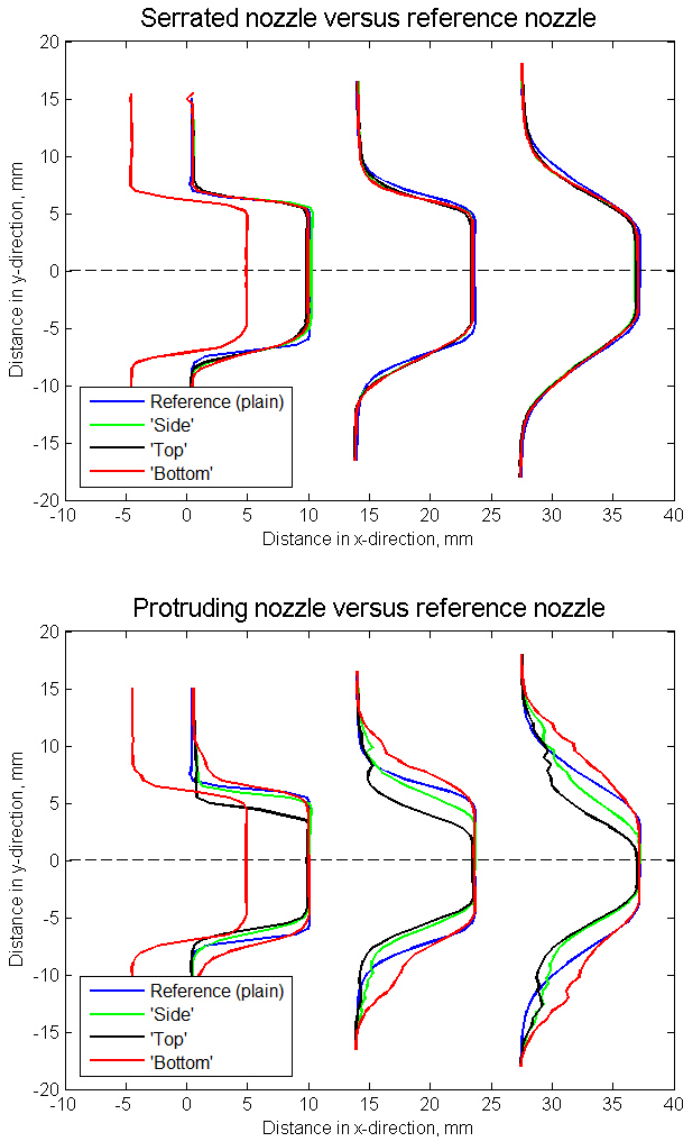

Figure 6.21: Comparisons of velocity profiles close to the outlet

As the most interesting portion of the jet, the mixing layers of the 'plain' and 'protruding'-jets underwent close investigation. Fields of all three velocity components (normalized) were obtained in an X,Y-plane 7.55mm above the coordinate origin. The state of the plain nozzle jet is shown in figures 6.22(a) to 6.22(c). The U-field and, to a lesser extent, the W-field show that the jet reaches the measuring plane at about 40mm downstream. Moreover, it is apparent from these plots that, despite slight variations close to the outlet,

the plain nozzle jet does not change along the Y-axis. Unfortunately, the first profile of the V-field was faulty and hence not included. The fact that the V-field is non-zero can most likely be attributed to a slightly misaligned probe. Expectedly, the contours resulting from measurements in the mixing layer of the 'protruding'-nozzle, display far less homogeneous velocity fields (Figure 6.23). The plot for the stream wise velocity (Figure 6.23(a)) clearly shows how the protrusions deflect parts of the flow (blue), which seems to push the air through the cut-outs more, leading to an earlier opening of the jet at these locations (e.g. -2mm or 11mm). Note that in the V-plot (Figure 6.23(b)) positive velocity corresponds to negative coordinate direction. Keeping this in mind, one can see clearly see how the protrusions direct the air into the 'windows' between them. These 'windows' are also visible in the W-contour (Figure 6.23(c)).
Combining the V and W-components of the first profiles used in the mixing layer contours, i.e. at one slot widths downstream, yields figure 6.24, where the velocity vectors projected on the YZ-plane are shown. As in the contours, the positions of the protrusions are clearly visible. The difference in upwards velocity left and right of each protrusion hints at vortexes around axes parallel to the X-axis and starting at the serration tips. Figure 6.25 gives graphic interpretation of figure 6.24.

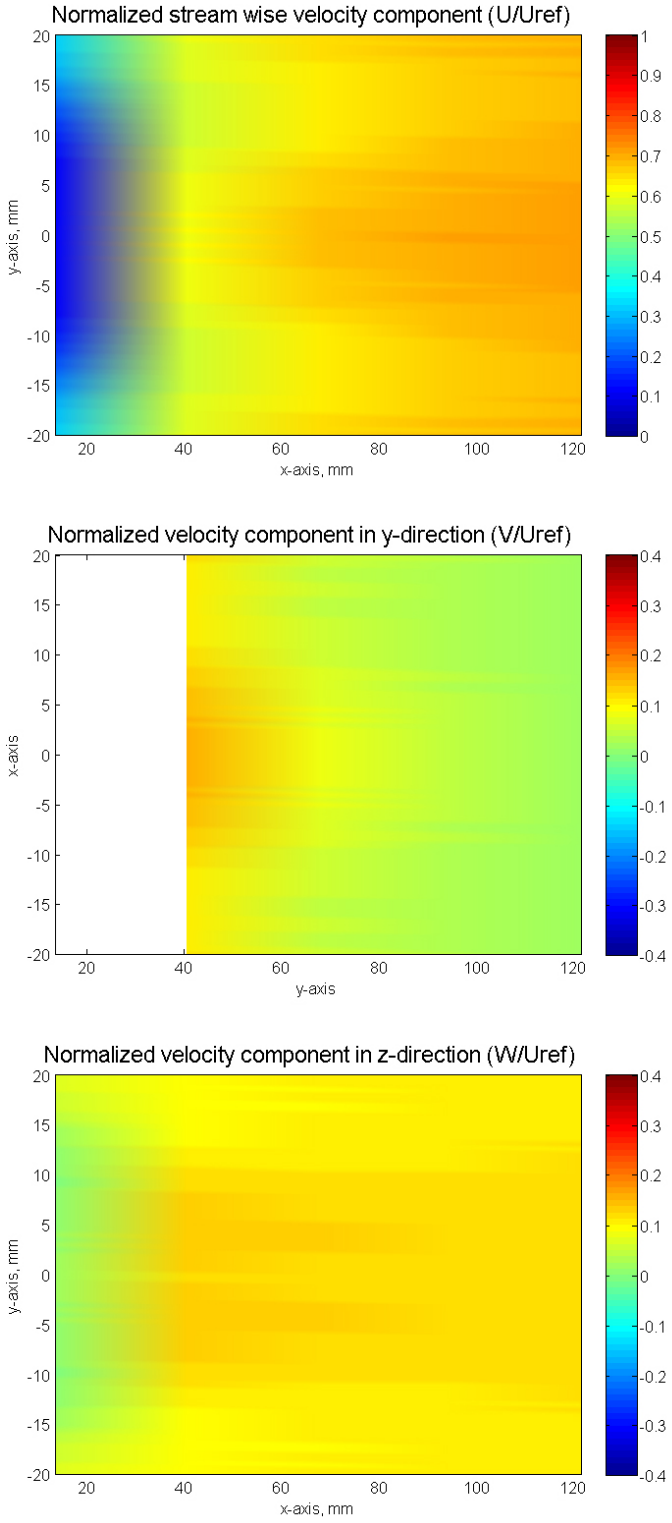

Figure 6.22: Fields of the respective velocity components in the mixing layer

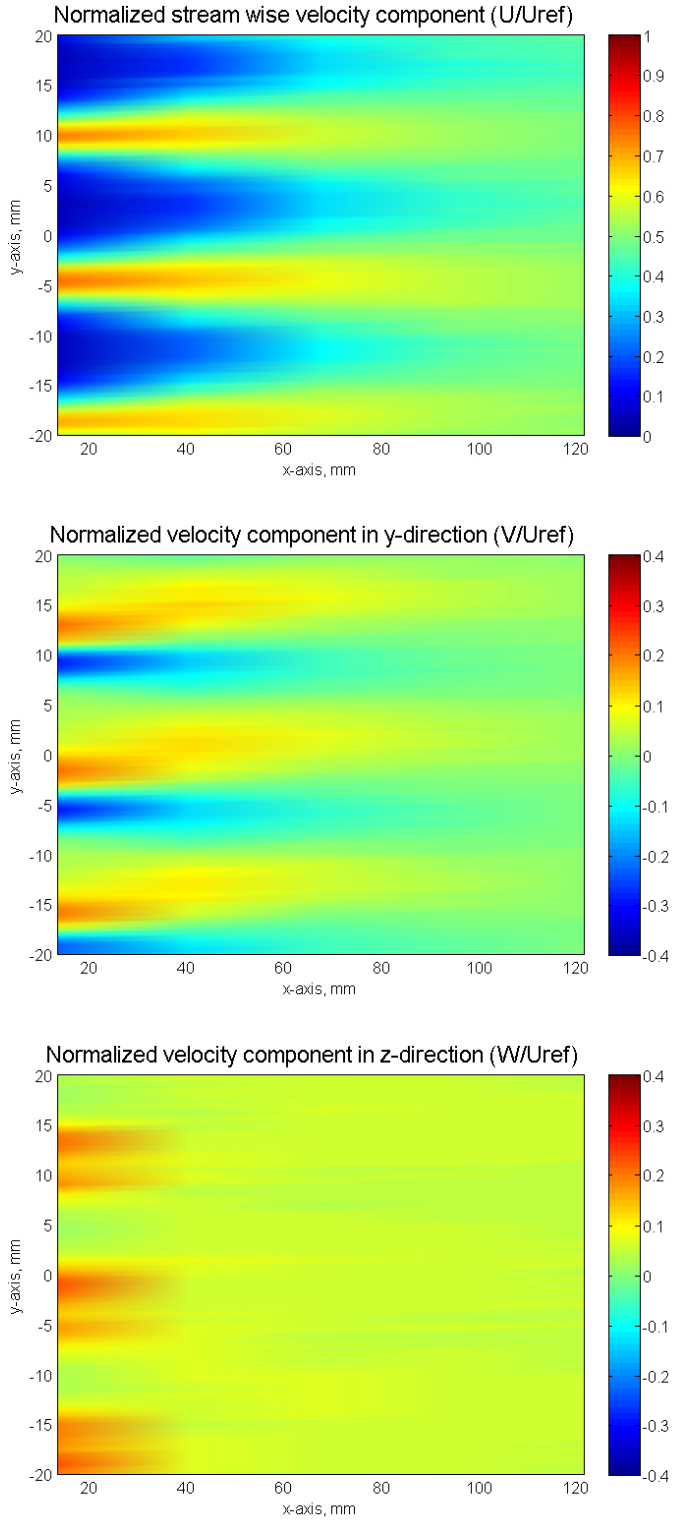

Figure 6.23: Fields of the respective velocity components in the mixing layer

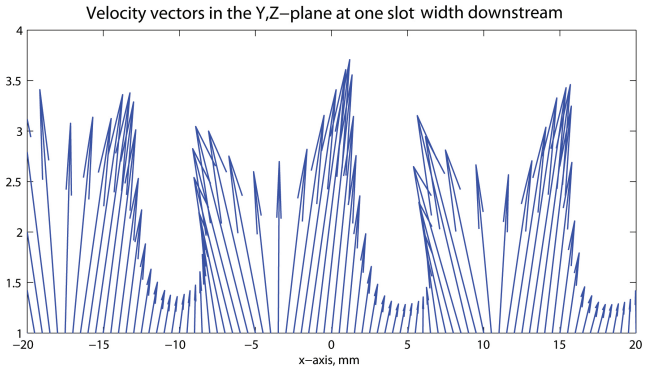

Figure 6.24: Velocity vectors

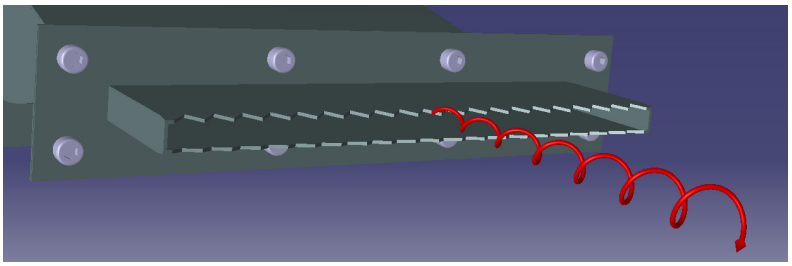

Figure 6.25: Velocity vectors

6.3.2 Turbulence intensity

Figure 6.23 shows the turbulence intensity I distribution in the jets stemming from the various nozzles. CHAPTERREF to THEORY explains how the values for I are extracted from the velocity data. As the full flow fields were only obtained with the probe in the 'upright' position (see CHAPREF), the values for the velocity fluctuations in Y-directions were unavailable and hence had to be estimated. But as u' and w' are relatively close in magnitude, the made assumption that v' was in the same range as well should be valid. The contour corresponding to the reference case shows the pointy onsets of the mixing layers. These turbulent areas steadily grow and start to merge at around 60mm (4-5SWs) downstream. This coincides satisfactorily with the centerline velocity decay (figure 6.20). When looking at the 'serrated' and protruding'-results, one has to keep in mind that, due to a manufacturing error, the nozzle used in these tests could not be positioned perfectly horizontal. The noticeable asymmetry in the contours is caused by this error angle of about two degrees. Moreover, there seems to be slightly more inherent turbulence at the outlet, which can also be attributed to the nozzle. The most obvious difference between the plain and serrated cases is

a general increase in turbulence intensity by about 10 to 15 per cent Even though the pointy onset of the mixing layers is visible also in the 'serrated'-plot, albeit slightly skewed by the asymmetry, the serrations seem to make the mixing layers grow a bit faster and merge a bit earlier. Also, the overall thickness, or height as these contours are XZ-sections, of the turbulent zone increases slightly in and after the merging area (80mm or 6SWs and onwards). The location of maximum turbulence, i.e. the X-position at which high I is sustained over a large Z-axis range, does not significantly change, however. It remains between 110mm (8SWs) and 140mm (11SWs) downstream. So, while straight serrations do increase turbulence intensity, the distribution of turbulence is not drastically changed. This is the case, however, when the serrations are protruding the flow. Figure 6.26(c) shows how strongly the jet resulting from the protruding nozzle differs from the reference configuration. In contrast to the other two configurations, where the mixing layer starts as a 'point' and subsequently grows at a relatively steady rate, the onset of the mixing layer in the 'protrusion' case is more diffuse and the following growth not constant. After a strong initial increase in thickness, the height of the turbulent zone remains almost constant from 50mm (4SWs) to 150mm (13SWs) downstream, where it starts to increase in size again, albeit slightly. The strong initial turbulence generation caused by the protrusions also leads to an early merging of the two mixing layers. The aforementioned location of maximum turbulence was moved upstream considerably. It is now between 70mm (5SWs) and 100mm (7SWs) downstream.

As described on page **??**, hot wire measurements were carried out in one of the mixing layer planes (7.55mm above the horizontal symmetry plane). Naturally, the data obtained was also used for turbulence investigations and since in this test all velocity vector components were measured, no estimating was necessary. Figure 6.27(a) holds the 'plain'-results. The visible 'peak lines' stem from post-processing and interpolation and must be disregarded. The most important conclusion that can be drawn is that the turbulence intensity is not a function of Y. At least in the area covered by the investigation, I is also relatively constant along the X-axis and in this regard this result shows good agreement with figure 6.26(a). The magnitude, however, does not. It is about 20% higher than it is in the corresponding locations in figure 6.26(a), namely at $x = 40.5 - 121.5$ and $z = -0.755$. One could assume that this difference is due to v' now being based on measured data rather than on estimates, but this would hint at very high velocity fluctuations in the Y-directions, which is unlikely in this, the plain, case. Part of this difference can be attributed to the reference velocity that is used to calculate I from k (See RIGHT THEORY CHAPTER AND METHOD CHAPTER). Normally the centerline velocity

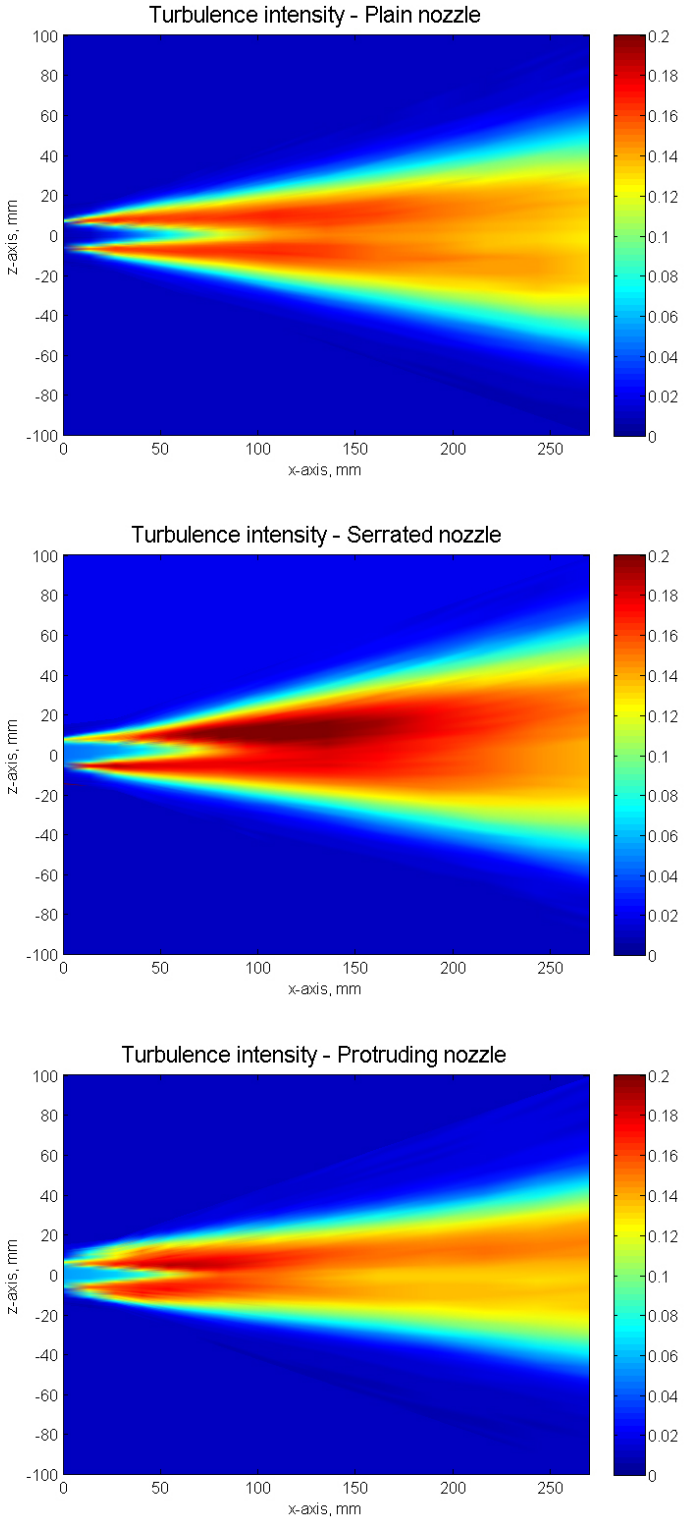

Figure 6.26: Resulting turbulence intensity when taking into account all three components u', v' (estimated) and w'.

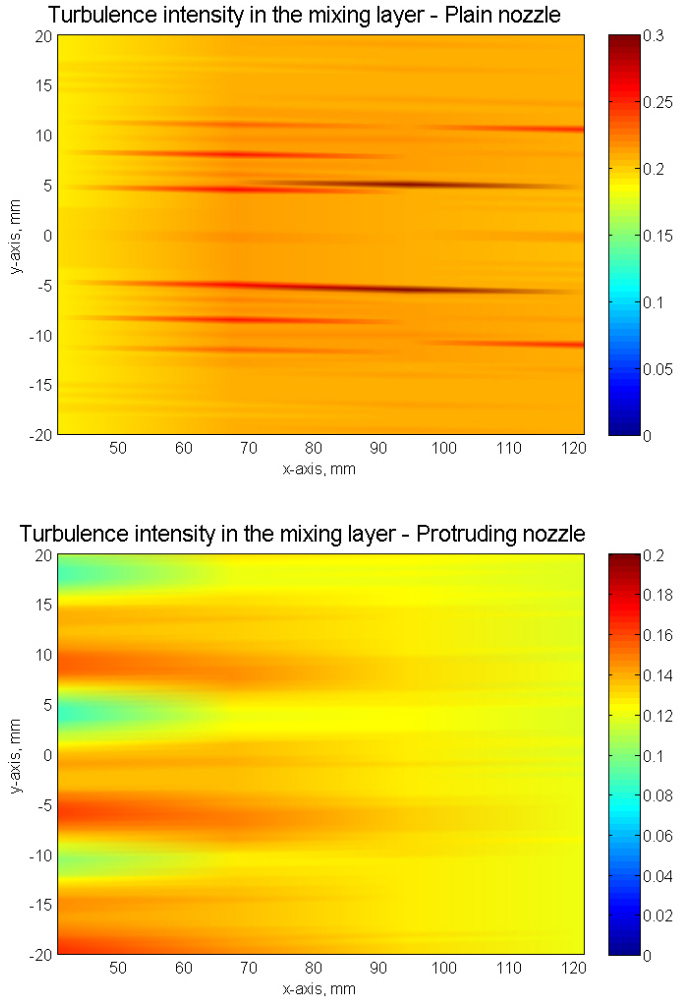

Figure 6.27: Turbulence intensity in the mixing layer with all components measured

directly after the outlet is used, but as this measuring set did not include any profiles that crossed the centerline, it was necessary to fall back on the calibration velocity (40m/s) of the wind tunnel. This calibration velocity can be different from the centerline speed obtained via hotwire by almost 10%. Naturally, the results could have easily been scaled to better fit the vertical velocity field, but as the turbulence intensity always contains a certain level of approximation, it is better to accept that the magnitude might be off by 10 or even more per cent and concentrate on trends and changes within each plot. Moreover, these considerations can, and should, also be applied on the vertical turbulence contours, as there the cases 'plain' and 'serrated' differ mainly in magnitude (Figures 6.26(a) and 6.26(b). The plot containing the results of the protruding nozzle (Figure 6.27(b) show the usual variations along the Y-axis. The vertical turbulence field (Figure 6.26(c)), like all serrated 16-profile fields obtained at the 'side'-position, would intersect this contour at the origin of the Y-axis. Areas shielded by the protrusions and hence calm can be seen at $y = -11$ or $y = 4$. Like in previous XY-plots, the variations along the Y-axis can be seen to fade out after a certain distance. Interestingly, the turbulence seems to be higher on the sides of the protrusions that face the negative coordinate direction. The vortexes hinted at by figure 6.24 might be responsible for that. Air goes counter clockwise (when looking in stream direction) around the vortex axes that start at the serration tips ($y = -11, 4$ and 18) and 'crashes' back into the jet, hence increasing turbulence intensity at $y = -20, -6$ and 8.

6.3.3 RMS of the angular velocity

In an attempt to visualize the rotation of the flow in the mixing layer (XY-plane 7.55mm above centerline), the RMS of the angular velocity fluctuations was calculated. To firstly calculate the angular velocity from the instantaneous flow angle, an algorithm for the deriving of series of discrete values (see APPENDIX REF TO CODE) was used. As the velocity measurements are always two-dimensional (U, W or U, V), this resulting angular velocity is one component of the angular velocity vector. If, for example, the probe is in the upright position (see section **??** on page **??**), the measured velocities are U and W, the calculated angle β_Y and, hence, the derived angular velocity ω_Y. Figures 6.28(a) and 6.28(b) show the contours of $\overline{\omega_Y}$ for the plain and the protruding nozzle, respectively. The leftmost area in the 'plain'-contour is not in the jet yet and should not be regarded as the X-wire probes do not reliably measure angles at velocities near zero. Generally speaking, the uniformity that, regardless of the displayed parameter, is typical for all the mixing layer contours of the plain nozzle case is present here as well. The protrusions, on the other hand, again strongly influence the jet. There seems to be a lot of rotation generated at the flanks of the protrusions (e.g. $x = -12, 3$). The visible asymmetry from the turbulence intensity contour (Figure 6.27(b) can be seen here as well. One should keep in mind, though, that both I and $\overline{\omega_Y}$ stem from the same raw data. $\overline{\omega_Z}$-plots can be found in the appendix on page **??**.

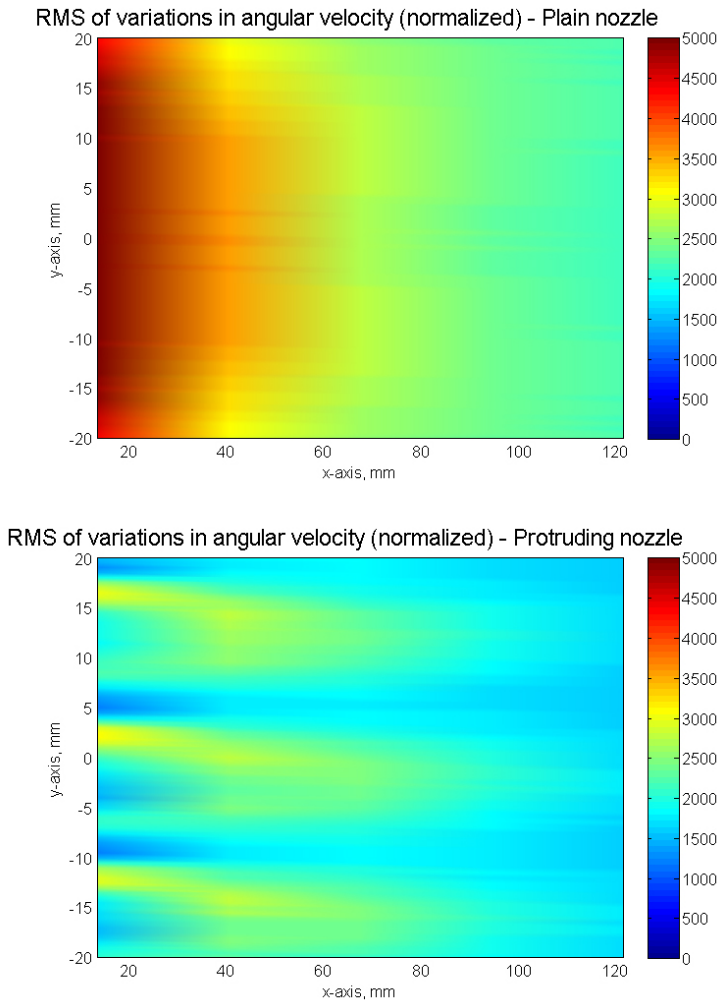

Figure 6.28: Root mean square contours of the angular velocity $\overline{\omega_Y}$ in the mixing layer

6.3.4 Coherence

For the coherence investigations, centerline velocity and sound were recorded simultaneously. This data was used to compute the magnitude squared coherence at 41 positions and the combined results are displayed in figure 6.29. The MSC values are low indeed, but they are at least in the same ballpark and there are notable differences between the configurations. In the 'plain'-case, maximum coherence seems to occur almost immediately after the outlet and over a relatively large frequency range, while the protrusions appear to altogether destroy this early peaks and lead to some coherence at about

10 SWs downstream. Interestingly, the peaks in the 'protrusions'-contour occur roughly where the mixing layers merge, an area which a number of researchers found to be the prime noise source (REFS). The plain nozzle does not seem to trigger any coherence in this area, however. When relating these coherence plots with the pure sound measurements, it can be assumed that the noise reduction due to the protrusions stemmed from the lower overall, or at least more distributed, coherence between flow movement and recorded sound. Also, the MSC results seem to agree with the directivity measurements, parts of which also indicate that the main noise source in a jet from a protruding nozzle is located further downstream than the source in a baseline jet.
Figure 6.30 shows selected results from comparing the ensemble averaged samples from the microphone and hot wire signals. Guj et al(REF) used the lag times between the peaks of sound and noise to (see figure 6.30(a) as an example) obtain distances. Using several microphones distributed around the facility allowed them to narrow down the most likely position of the noise source. In the investigation at hand, the hot wire probe was moved along the jet centerline in 41 0.5SW steps and comparisons were done at all these positions. Unfortunately, they did not yield any meaningful correlation. Figure 6.31 shows the lag time as a function of stream wise hot wire probe position. The resulting curve is arbitrary.

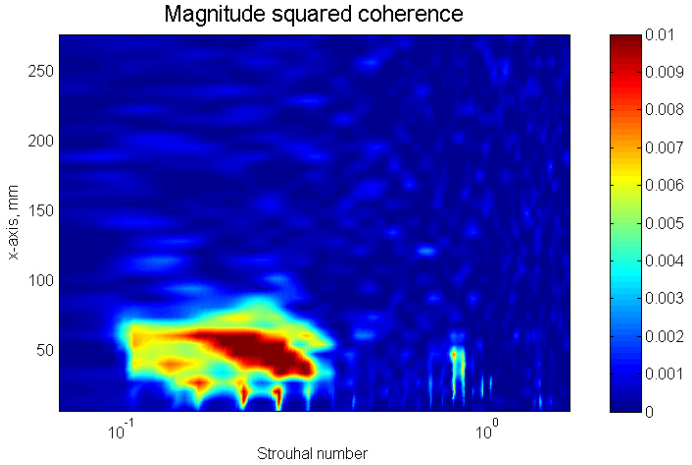

(a) Plain nozzle

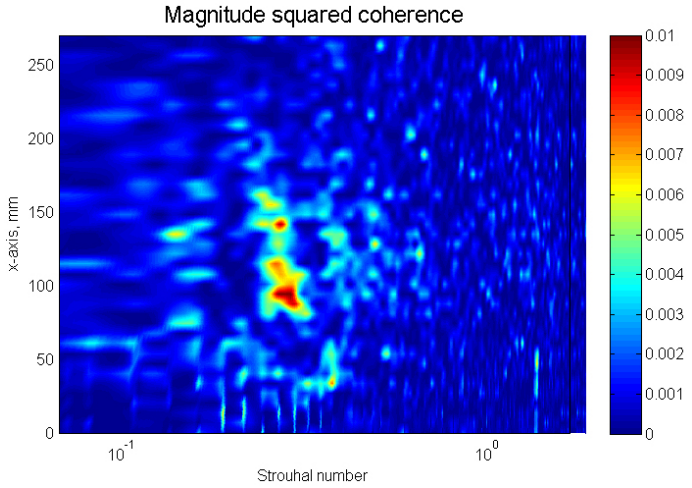

(b) Protruding nozzle

Figure 6.29: Contours of the magnitude squared coherence

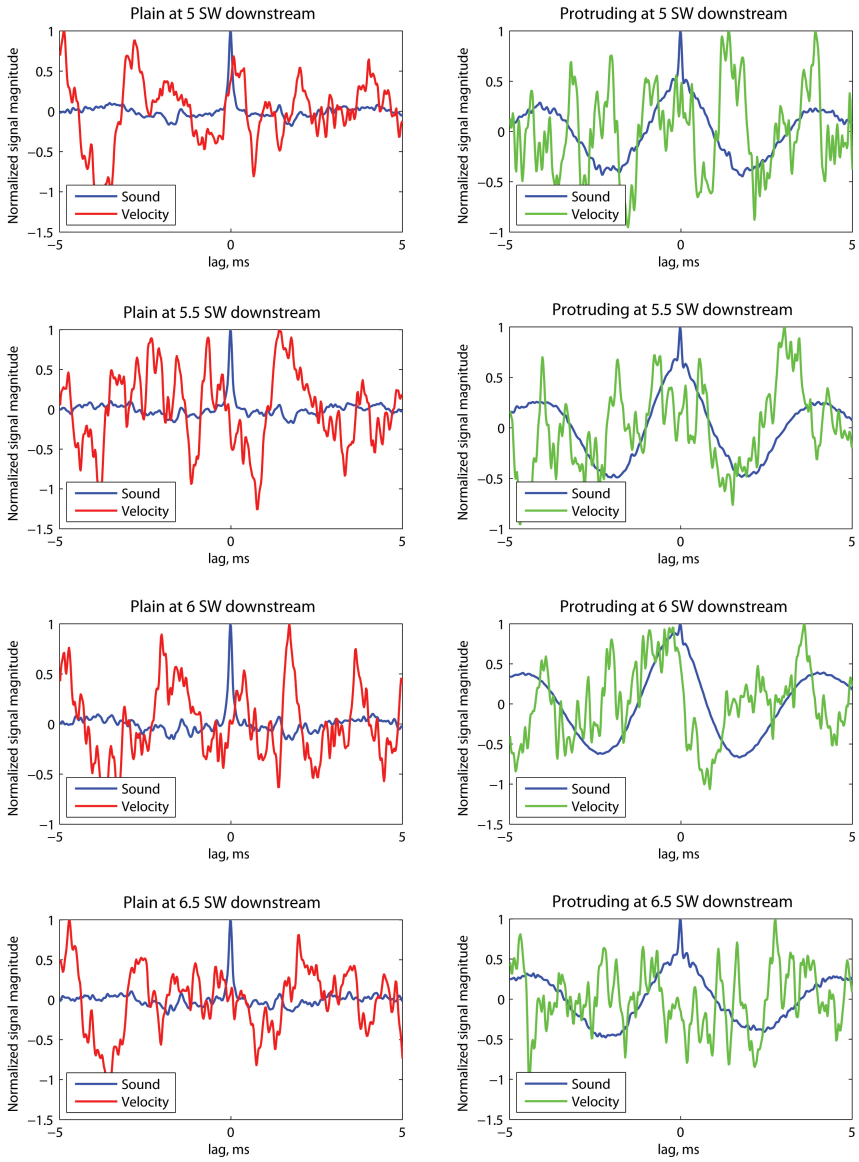

Figure 6.30: Ensemble averaged samples of sound and speed. Representative for all comparisons, the plots corresponding to the transition zone after the potential core are shown here.

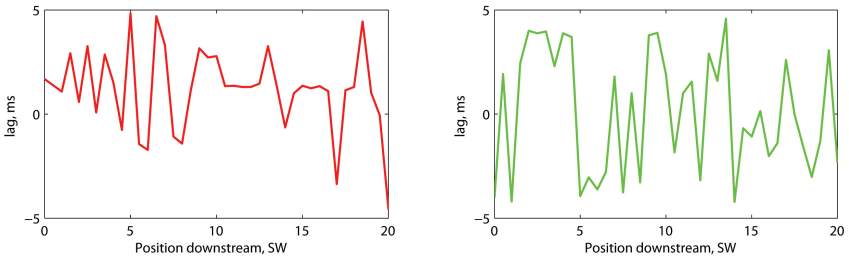

(a) Plain nozzle (b) Protruding nozzle

Figure 6.31: Lag between the maxima of the averaged sound and velocity samples as a function of X.

7 Conclusion

Actual sound emission into the surroundings was only measured in the far field and directivity measurements, with the results of both clearly stating that nozzle chevrons succeed in reducing jet noise. At an exhaust velocity of 40m/s or Mach 0.12 the nozzle equipped with straight serrations lowered the overall sound pressure level by up to 2dB compared to the baseline configuration. Bending the chevrons such that the tips would reach 1mm into the flow yielded a further 2 dB drop in sound pressure level. The noise reduction were found to be directional, with the mentioned maxima recorded at 90 degrees from the jet axis. At 30 degrees there is no reduction in SPL at all. The spectra of the far field sound show that the serrated nozzles work best at $0.3 < St < 1$, an effect observed at all far field and directivity measuring positions. In fact, (Callender et all REF) observed a similar behavior of round nozzles. At aft angles ($\sim$30 degree) the serrations lead to a stark increase in noise level at very low frequencies, which effectively compensates the reductions at $0.3 < St < 1$. A weighting function will most probably lessen this low frequency contribution, however.

Despite both investigated nozzle configurations reliably reducing mixing noise in the far field, the near field microphone measurements and the hot wire investigations of the flow indicate that the each nozzle worked in a different way. Straight serrations increase the turbulence intensity in big portions of the jet, while leaving the basic jet shape unchanged. Moreover, this nozzle seems to increase hydrodynamic pressure fluctuations in the near field. The acoustic fluctuations are most likely reduced to some extend, however, which would explain the far field reductions. Protruding serrations, on the other hand, reduced the turbulence intensity in the flow field and significantly changed the shape of the jet. In the near field, the reductions in SPL due to protruding serrations are drastic. One might assume that hydrodynamic as well as acoustic fluctuations are lessened.

That the serrations influence the signature of the acoustic far field is made obvious by the fact that in the auto- and cross-correlation plots, each nozzle

has a particular basic shape, which can be recognized and assigned to the corresponding nozzle in the plots of virtually all far-field measuring positions.
As usual, gaining a few answers yields a number of further questions. Especially a confirmation of the observed influences of the two different serration configurations through further experiments would be desirable. In order to investigate the proposed source in the transition zone downstream of the potential core, a jet velocity above Mach 0.7 is necessary and, in such an investigation, a non-intrusive flow visualization method would be a useful complement to hot wire anemometry. Not only could flow results be counterchecked, but, as shown by e.g. (REF HILEMAN), non-intrusive flow visualization is better suited to source detection than is HWA. It must be stressed, however, that there is still a lot of potential in the equipment used in the present work. Simple alterations of the method might very well yield improved results. Possible changes include the use of micro hot wire probes with reduced measuring volumes, smaller traverse steps close to the outlet and a method to more precisely define the initial positions of probes and microphones. Another simple, but potentially enlightening improvement would be increasing the area covered by the moved microphone in the far field. Simultaneous near and far field measurements with subsequent correlation investigations are highly recommend as well. Last, but not least, the first results of the mentioned FE-simulations will most probably yield questions that need to be dealt with experimentally.
The work at hand succeeded in detecting changes due to alterations of the nozzle in many flow and sound field properties, but extensive further research is necessary to assign the observed effects to their respective physical causes.

References

[1]. URL: http://www.airliner-pics.com/caravelle/cn209.htm (cit. on p. 1).

[2]. URL: http://imageshack.us/f/832/19690823okldatupolevtu1.jpg/ (cit. on p. 1).

[3]. URL: http://www.thedistilledwatercompany.com/distilled-water-news/correction-distilled-water-and-boeing-707-engines/ (cit. on p. 1).

[4]. URL: http://www.flugzeug-bild.de/name/einzelbild/number/7439/kategorie/militaerflugzeuge~mc-donnell-douglas~f4-phantom-ii.html (cit. on p. 2).

[5]. URL: http://people.hofstra.edu/geotrans/eng/ch3en/conc3en/ch3c5en.html (cit. on p. 2).

[6]. URL: http://en.wikipedia.org/wiki/Boeing_787 (cit. on p. 4).

[7]. URL: http://wings.avkids.com/Book/Propulsion/advanced/types-01.html (cit. on pp. 8–11).

[8]. URL: http://www.revisemri.com/questions/creating_an_image/fourier_transform (cit. on p. 12).

[9]. URL: http://sepwww.stanford.edu/sep/prof/waves/cs/paper_html/node8.html (cit. on p. 12).

Arndt, R. E. A., D. F. Long, and M. N. Glauser (1997). "The proper orthogonal decomposition of pressure fluctuations surrounding a turbulent jet". In: *Journal of Sound and Vibration* Vol. 340 (cit. on p. 109).

Bakken and Krogstad (2004). "A velocity dependent effective angle method for calibration of X-probes at low velocities". In: *Experiments in Fluids* Vol. 37 (cit. on pp. 69, 77).

Bogey, C. and C. Bailly (2004). "The proper orthogonal decomposition of pressure fluctuations surrounding a turbulent jet". In: *Journal of Sound and Vibration* Vol. 340 (cit. on p. 49).

Bräunling (2009). *Flugzeugtriebwerke*. Springer Verlag (cit. on p. 16).

Callender, B., E. Gutmark, and S. Martens (2005). "Far-Field Acoustic Investigation into Chevron Nozzle Mechanisms and Trends". In: *AIAA Journal* Vol. 43 (cit. on pp. 50, 51, 104, 105).

Coiffet, F., P. Jordan, J. Delville, Y. Gervais, and F. Ricaud (2006). "Coherent structures in subsonic jets: a quasi-irrotational source mechanism?" In: *International Journal of Aeroacoustics* Vol. 5 (cit. on pp. 49, 109).

Dantec (2012). URL: `http://www.uwo.ca/finance/andrew/Dantec950/traverse.pdf` (cit. on p. 58).

Eck, B. (1981). *Technische Strömungslehre I & II*. Springer Verlag (cit. on pp. 23, 24, 26).

Environmental noise (2012). URL: `http://www.nonoise.org/library/envnoise/` (cit. on p. 3).

Guj, G., M. Carley, and R. Camussi (2003). "Acoustic identification of coherent structures in a turbulent jet". In: *Journal of Sound and Vibration* Vol. 259 (cit. on pp. 48, 49, 54, 96).

Harper-Bourne, M. (2004). "On modeling the hydrodynamic field of high-speed jets". In: *10th AIAA/CEAS aeroacoustics conference* (cit. on pp. 49, 109).

Hileman, J. I., B. S. Thurow, E. J. Caraballo, and M. Samimy (2005). "Large-scale structures evolution and sound emission in high-speed jets: real-time visualization with simultaneous acoustic measurements". In: *Journal of Fluid Mechanics* Vol. 544 (cit. on p. 48).

ICAO (2012). URL: `http://legacy.icao.int/env/noise.htm` (cit. on p. 3).

Juvé, D., M. Sunyach, and G. Comte-Bellot (1980). "Intermittency of the noise emission in subsonic cold jets". In: *Journal of Sound and Vibration* Vol. 71 (cit. on p. 49).

Lighthill, M. J. (1952). "On sound generated aerodynamically". In: *Proceedings of the Royal Society of London. Series A, Mathematical and Physical Sciences* Vol. 211 (cit. on pp. 44, 47).

Marn and Pirker (2011). "Technische Akustik und Lärmarm konstruieren". In: (cit. on p. 27).

mathworld (2012). URL: `http://mathworld.wolfram.com/Cross-Correlation.html` (cit. on p. 14).

Matlab. URL: `MatlabR2010bdocumentation` (cit. on p. 14).

Moreau, D. J., L. A. Brooks, and C. J. Doolan (2012). *Noise and flow characteristics of a small-scale anechoic wind tunnel*. Tech. rep. School of Mechanical Engineering, The University of Adelaide, 5005 South Australia, Australia (cit. on pp. 58–61).

Möser, G. and M. Müller (2003). *Taschenbuch der technischen Austik*. Springer Verlag (cit. on pp. 3, 27, 35, 40, 41, 43, 44, 105).

NASA (1999). “Making Future Commercial Aircraft Quieter”. In: *NASA facts* (cit. on pp. 41, 42).

Panda, J., R. G. Seasholtz, and K. A. Elam (2005). “Investigation of noise sources in high-speed jets via correlation measurements”. In: *Journal of Fluid Mechanics* Vol. 537 (cit. on p. 49).

Payne, S. J. “Unsteady Loss in a High Pressure Turbine Stage”. PhD thesis (cit. on pp. 67–69).

POST (2003). “Aircraft noise”. In: *postnote*, No. 197 (cit. on p. 3).

Schlichting, H. and K. Gersten (1997). *Grenzschicht-Theorie*. Springer Verlag (cit. on pp. 15, 18, 27).

Stainback, P. C. and K. A. Nagabushana (1992). *Review of Hot-Wire Anemometry Techniques and the Range of their Applicability for Various Flows*. Tech. rep. NASA Langley Research Center, Hampton, VA 23681, USA (cit. on pp. 70, 72).

Suzuki, T. (2010). “A review of diagnostic studies on jet-noise sources and generation mechanisms of subsonically convecting jets”. In: *Fluid Dynamics Research* Vol. 42 (cit. on p. 47).

Tam, C. K. W., K. Viswanathan, K. K. Ahuja, and J. Panda (2008). “The sources of jet noise: experimental evidence”. In: *Journal of Fluid Mechanics* Vol. 615 (cit. on pp. 52, 54, 105).

Tinney, C. E. and P Jordan (2008). “The near pressure field of co-axial subsonic jets”. In: *Journal of Fluid Mechanics* Vol. 611 (cit. on pp. 49, 51, 52, 108, 109).

Viswanathan, K. (2004). “Aeroacoustics of hot jets”. In: *Journal of Fluid Mechanics* Vol. 516 (cit. on p. 48).

Wikipedia. URL: `MatlabR2010bdocumentation` (cit. on p. 15).

Appendices